



TECHNISCHE
UNIVERSITÄT
WIEN
Vienna University of Technology

Unterschrift (Betreuer)

DIPLOMARBEIT

Monte Carlo versus pencil beam based dose calculation for scanned proton therapy: assessment of optimal calculation and user interface parameters

Ausgeführt am
Atominstitut
der Technischen Universität Wien

und der
Universitätsklinik für Strahlentherapie
der Medizinischen Universität Wien

unter der Anleitung von Univ. Prof. Dr. DI Dietmar Georg und Mag. Barbara Knäusl, Ph.D
als verantwortlich mitwirkende Universitätsassistentin.

durch
Sandra Nemecek, BSc
Spargelfeldstraße 166/3/2
1220 Wien

28. September 2015

Unterschrift (Student)

Danksagung

Zuallererst möchte ich mich ganz besonders bei Mag. Barbara Knäusl, Ph.D. bedanken, die mir im Laufe dieser Arbeit mit viel Geduld und vielen guten Ratschlägen zur Seite stand und stets ein offenes Ohr für Fragen hatte. Vielen herzlichen Dank!

In diesem Zusammenhang sei auch Dipl.-Ing. Hermann Fuchs gedankt, der meine Fragen stets mit Geduld beantwortet hat.

Für die Betreuung meiner Diplomarbeit möchte ich mich auch besonders bei Univ. Prof. Dr. DI Dietmar Georg bedanken.

Dank auch an O. Univ. Prof. Dr. Richard Pötter, Vorstand der Univ. Klinik für Strahlentherapie, für die Möglichkeit die Diplomarbeit in seiner Abteilung durchzuführen.

Hier möchte ich auch meinen Dank an Ass.Prof. Dipl.-Ing. Dr.techn. Karin Poljanc aussprechen, welche mich an das AKH vermittelt hat und dadurch diese Arbeit erst ermöglicht hat.

Ebenfalls möchte ich mich auch bei Andreas Hoppe von der Firma Elekta bedanken, der für die Fehler anderer büßen musste und meine Anfragen stets zügig bearbeitet hat.

Ganz besonderer Dank gebührt meiner Mutter Maria, die mir mit ihrem Intellekt und Kampfgeist immer ein Vorbild war und mich lehrte, niemals aufzugeben wenn man etwas erreichen möchte. Ausgesprochen gerne möchte ich auch meinem Vater Hermann für den Ideenreichtum und die Improvisationsgabe, welche er mir in meiner Kindheit beigebracht hat, danken. Beide zeigten immer ein großes Interesse an meinem Studium und haben mich dabei moralisch und finanziell unterstützt. Vielen, vielen Dank!

Im Speziellen bedanke ich mich auch bei meinen beiden Schwestern Lisa und Birgit, die mich mit Heiterkeit durch das Leben begleiten.

Weiters bedanke ich mich bei meinem Freund Philip, der auch nach einem anstrengenden Arbeitstag für mich da war und mir während der gesamten Arbeit mit viel Fachwissen und Humor zur Seite stand. Danke!

Schlussendlich möchte ich noch meinen Freunden, für all die schönen Stunden, vor und während meines Studiums und hoffentlich auch in Zukunft, danken.

Die finanzielle Unterstützung durch das Bundesministerium für Wissenschaft, Forschung und Wirtschaft und der Nationalstiftung für Forschung, Technologie und Entwicklung wird dankbar anerkannt.

Abstract

Background

Treatment planning systems for proton and carbon ion beam therapy are commonly based on fast analytic dose calculation engines using pencil beam (PB) algorithms. Monte Carlo (MC) calculations, on the other hand, are recognized for their superior accuracy due to their better consideration of physical processes. Therefore, the value of MC based calculation for proton treatment planning has been investigated.

Material and Methods

The purpose of this project was to benchmark the MC algorithm against the PB algorithm and to identify clinical useful MC calculation settings for dose calculation in proton therapy. E.g. the mean relative statistical uncertainty per spot ($unc=1-5\%$), the mean relative statistical uncertainty threshold ($err=10\%-60\%$ of the maximum dose per spot) for voxels included in the uncertainty calculation and the maximum numbers of particles ($maxNr=5 \times 10^3-5 \times 10^5$). Furthermore, treatment planning parameters as e.g. peak width multiplier and spot spacing were investigated. Treatment plans based on the PB algorithm were optimized and recalculated via MC algorithm using the XiO treatment planning system research version v4.62 (Elekta AB, Stockholm, Sweden). A homogenous water phantom with three cubes of different size and complex multi-layer chess pattern phantom (HU of +1000 (bone) and -800 (lung)) embedded in a water tank, with target structures placed within or at different distances behind the chess pattern, was created. The clinical applicability was tested for a prostate and a paranasal sinus (PS) patient. The results of the PB and the MC treatment plans were compared on the basis of dose calculation times, dose profiles, dose difference maps, γ -index analysis and conformity index (CI) and homogeneity index (HI) measures.

Results

To ensure that the number of particles didn't terminate the dose calculation, 5×10^4 particles were necessary for unc values of 3-5% and 5×10^5 below 3%. A peak width multiplier of 0.8 and a spot spacing of 0.5cm achieved the best results in regards to the treatment planning parameters. Different dose deposition characteristics of the MC and PB algorithm in the presence of media with large density and composition variations could be observed. The MC algorithm deposited more dose to areas located proximal to low density tissue. Dose-difference maps revealed hotspots having a dose difference of up to 21% (PS patient) and 19% (prostate patient) of the prescribed dose. γ -index analysis (2%/2mm) indicated a good agreement between the MC and the PB algorithm.

Conclusion

A relative statistical uncertainty per spot of 5% seemed acceptable for clinical MC dose calculation, especially when regarding the dose calculation time. The PB algorithm worked accurate and attained comparable result, even in difficult treatment situations involving large density and tissue heterogeneities.

Contents

Danksagung	i
Abstract	iii
1. Introduction	1
1.1 Technological developments in radiation therapy in the last century.	1
1.2 Motivation	3
2. Basics of medical radiation physics	5
2.1 Interaction processes	5
2.2 Interaction processes of photons	5
2.2.1 Coherent scattering.	6
2.2.1 Compton effect	7
2.2.2 Photoelectric effect.	9
2.2.3 Pair production	10
2.2.4 Relevance of the various processes	11
2.3 Interaction processes of charged particles	13
2.3.1 Stopping power	13
2.3.2 Linear energy transfer (LET)	14
2.3.3 Relative biological effectiveness (RBE)	15
2.4 Comparison of protons and photons	16
2.5 Comparison of protons and heavier ions	17
2.6 Dosimetric quantities	18
2.7 Beam delivery.	20
2.7.1 Passive scattering	20
2.7.2 Active scanning	21
2.8 Treatment planning principles	22
2.9 Volume concepts	23
2.9.1 Volume types.	23
2.10 Treatment techniques	26
2.10.1 Conformal radiotherapy (CRT).	26
2.10.2 Single-field uniform dose (SFUD)	26
2.10.3 Intensity modulated radiation therapy (IMRT) and intensity modulated particle therapy (IMPT)	27

2.11	Dose calculation algorithms	28
2.11.1	Correction based algorithms.	28
2.11.2	Model based algorithms	29
2.11.3	Pencil beam algorithm.	30
	Precision.	31
2.11.4	Monte Carlo algorithm	32
	Mean relative statistical uncertainty (MCuncertainty)	33
	Mean relative statistical uncertainty threshold (MCerrordosethreshold).	33
	Maximum number of particles (MCmaxnrparticles)	33
2.12	Optimization process	34
2.13	Evaluation parameters	35
2.13.1	Isodose distributions.	35
2.13.2	Dose-volume histogram (DVH)	35
2.13.3	Dose-volume-specifications	36
2.13.4	Homogeneity index (HI).	37
2.13.5	Conformity index (CI)	37
2.13.6	Dose-difference maps	37
2.13.7	Gamma index method.	37
3.	Material and methods	39
3.1	Phantom geometries	39
3.1.1	Phantom 1 “Testphantom”	39
3.1.2	Phantom 2 “Chessphantom”	41
3.1.3	Phantom 3 “Waterphantom”	42
3.2	Hardware, Treatment planning system and software	43
3.2.1	Treatment planning Hardware	43
3.2.2	XiO	43
3.2.3	CERR	43
	3D gamma metric in CERR	43
3.3	Experimental Setup.	44
3.3.1	Planning.	44
3.3.2	Parameter input.	45
3.3.3	Evaluation of the MC parameters	46
3.3.4	Evaluation of the user interface parameters	47

4. Results	48
4.1 Assessment of the MC parameters	48
4.1.1 Stop criterion maximum number of particles	48
4.1.2 Evaluation of the Chess Target	49
Comparison of MC and PB results	52
4.1.3 Evaluation of Target 1, 2 and 3	57
Comparison of MC and PB results	60
4.2 Assessment of the user interface parameters	64
4.2.1 Evaluation of the peak width multiplier.	64
4.2.2 Evaluation of the spot spacing.	67
4.3 Patient examples	69
4.3.1 Prostate patient	69
4.3.2 Paranasal sinus patient	78
5. Summary and Discussion	82
6. Outlook	87
Bibliography	89
List of Figures	94
List of Tables	96
List of Abbreviations	97

1. Introduction

1.1 Technological developments in radiation therapy in the last century [1], [2]

With the discovery of X-rays by Wilhelm Conrad Röntgen in 1895 [3] - an achievement that earned him the first Nobel Prize in Physics in 1901 - the foundation for radiotherapy has been laid. Soon after this groundbreaking discovery the potential of using radiation for medical purposes was explored and only one year later, in 1896, Leopold Freund, a professor of radiology at the Medical University of Vienna, treated a 5 year old girl suffering from a skin disease [4]. He is the first physician known to have used ionizing radiation for therapeutic purposes and can be considered as the founder of medical radiology and radiotherapy.

Soon after Röntgen's milestone, the discovery of radioactivity by Henri Becquerel in 1896 [5] and the discovery of Radium by Marie and Pierre Curie [6] in 1898 caused further interest in this area. In 1901, Henri Becquerel and Pierre Curie published a paper about physiologic effects caused by radium radiation [7]. Their work inspired scientists to consider medical treatments for various diseases. Two years later, in 1903, Henri Becquerel was honored with the Nobel Prize in Physics *"in recognition of the extraordinary services he has rendered by his discovery of spontaneous radioactivity"* [8]. Pierre and Marie Curie received the Nobel Prize together with Henri Becquerel *"in recognition of the extraordinary services they have rendered by their joint researches on the radiation phenomena discovered by Professor Henri Becquerel"* [8].

In 1904, only nine years after the first discovery of X-rays by Wilhelm Conrad Röntgen, the first radiation therapy textbook was available [9], which granted a larger number of scientists a deeper insight of the subject.

During the first years of radiation therapy, no suitable method of dose measurement and only limited knowledge of biologic effects were available, leading to severe side effects for the patients. For this reason, biologists and physicists tried to assemble information about the correlation between dose and time on cell survival in terms of radiation therapy, in the following three decades of the 20th century. In the 1930s C. Regaud, R. Ferroux [10] and H. Coutard [11] established the different recovery of normal and malignant cells. They provided evidence of the reduction of side effects by applying the total dose in smaller fractions instead of one or a few large doses, which led to employ dose fractionation, a concept that is still employed in clinical routine. Furthermore, their findings showed that normal cells are able to recover better from radiation injury than cancer cells. Parallel to these discoveries, W.D. Coolidge developed a more powerful X-ray tube (180–200kV) [12] that allowed physicians to treat deeper located tumors, providing the basis of more sophisticated technology [13].

The development of the linear accelerator by Widerøe [14], the cyclotron by E. O. Lawrence and M. Stanley Livingston [15] and the betatron by Kerst [16] were the next steps that enabled treatments with even higher photon energies.

Around 1955, the first linear accelerators for clinical purposes became available, but as they were prototypes only, it lasted around the 1960's and 1970's until they became widely used [17]. The Megavoltage era, starting in 1950, was marked by the development of cobalt teletherapy machines (equivalent to approximately 1.3MV X-rays) and megavoltage linear electron accelerators. The higher energies made an increase of the penetration depth possible and enabled better skin sparing. To this day, linear accelerators underwent continuous improvements: automated beam shaping technologies like multi-leaf collimators or wedge filters and new dynamic beam delivery methods further improve the treatment efficiency.

In 1946, Robert Wilson, the founding director of Fermi National Labs, laid the groundwork for particle beam therapy. He proposed the use of accelerated protons for medical purposes [18], due to the physical properties of particles. In his pioneering paper, he explained the finite and controllable beam range of particle beams, the possibility of narrow collimated beams and the distinct dose deposition at the end of the particles ranges.

Only nine years later, in 1954, the first clinical use of protons took place at the Lawrence Berkeley Laboratories [19] and initial clinical studies were performed on patients [20]. In the following years, the medical use of protons and heavier ions was investigated in physics laboratories all over the world. In Sweden, the Gustav Werner Institute began with proton treatment research [21] and in the 1970's, the first hospital-based proton facility was built at the Loma Linda University Medical Center (LLUMC) in the USA [22].

Starting in the 1950's, radiation treatment with ions heavier than protons became of interest and several studies were carried out. For example, the Lawrence Berkley Laboratory treated 2054 patients with helium ions starting from the late 1950's up to the early 1990's [23].

Patient treatment with carbon ions was first carried out in 1994 at the National Institute of Radiological Sciences (NIRS) in Japan [24]. Further research developments lead to Japan being the best equipped and most experienced country concerning carbon ion treatment. Nowadays, eight carbon ion facilities are in operation worldwide [25], whereas four are located in Japan alone. In Europe, radiation therapy with carbon ions is performed at the "Heidelberg Ionenstrahl-Therapiezentrum" (HIT) in Germany and the "Centro Nazionale di Adroterapia Oncologica" (CNAO) in Italy [25]. In Austria, another therapy center, called "MedAustron", is currently built at Wiener Neustadt and the first patient treatment is planned for end of 2015.

Radiation therapy as we know it today began in the 1960's with the introduction of computers able to calculate detailed dose distributions. The Memorial Hospital in New York is generally credited as the first to use automatic computing machines for radiation dosage calculations in 1955 [26].

Computer development had a huge impact on many fields of cancer therapy and diagnosis. An important step was the introduction of high quality three-dimensional medical imaging in the 1970's, by means of Computed Tomography (CT), Magnetic Resonance Imaging (MRI) and Positron Emission Tomography (PET).

The Computed Tomography developed by Sir Godfrey Newbold Hounsfield in 1971 [27], [28] enabled three dimensional images of the patient anatomy and allowed to map the location of tumors very precisely. Furthermore CT images provided additional information about the material composition. The so called Hounsfield units (HU) represent a quantitative scale for describing the radiodensity of the materials and thus allow a more precise dose calculation. Imaging techniques such as CT and MRI are essential and necessary for a good differentiation of tumor volume from healthy surrounding tissue.

Advances in computer technology and radiation physics made it possible to deliver radiation more accurately. Conformal radiotherapy (CRT), for example is a treatment technique, where the radiation beams are aligned to the shape of the tumor and the beams can be delivered to the tumor from several directions.

Another widely used treatment technique, Intensity Modulated Radiation Therapy (IMRT) where the underlying concept was first described in 1978 [29] is similar to conformal radiotherapy with the advantage that the intensity (fluence) of the beams can be adjusted.

1.2 Motivation [30]

The aim of any radiotherapy treatment is to homogeneously deliver the prescribed dose to the tumor volume while reducing the dose to the surrounding normal tissue. Especially, the dose to the so called organs at risks (OARs) in the proximity of the tumor should be as low as possible to reduce side effects and normal tissue complications. To use modern radiotherapy techniques in an adequate way, anatomical and functional imaging modalities with a suitable resolution are essential to identify the tumor volume and the organs at risk. Modern treatment planning systems based on sophisticated and fast dose calculation algorithms play an important role in the fast development of modern radiotherapy techniques like IMRT and particle beam therapy. For realizing modern radiotherapy, treatment imaging devices, a planning workstation (able to calculate treatment plans) and an accelerator (able to deliver the desired radiation) are the fundamental basis.

During the last decade the significance of particle beam therapy in radiation oncology has increased. Until today 49 proton and ion beam therapy facilities have been built in Europe, Asia and the United States [25]. Based on the unique depth-dose characteristics of particle beams that follow with a signature Bragg peak at a well defined depth in a medium, particle beam therapy is one of the most advanced forms of therapy offered to cancer patients. Due to these theoretical physical advantages, particle beam therapy is supposed to deliver less dose to the normal tissue compared to photon therapy for a given prescribed dose. The sharp fall-off of the Bragg peak can potentially spare critical structures located directly behind the target volume. The usage of protons could result in a general reduction of the integral dose outside of the target volume by a factor of 2 or 3 compared to photons [31]. The main disadvantage of proton therapy is the large size and the high costs of the accelerator and the beam lines. Furthermore, proton therapy is less robust in comparison to photon therapy and many sources of

uncertainties influence the outcome of proton therapy, as for example the biological model that is used for dose calculation and patient setup and organ movement during the therapy.

In principle, two different types exist for particle beam delivery. For passive scattering (chapter 2.7.1), a narrow beam is spread to clinically relevant field sizes making use of passive scattering materials. For the active scanning (chapter 2.7.2), a single narrow pencil beam is magnetically swept over the dimension of the target volume, applying the radiation dose without the need to construct beam shaping devices.

Currently, treatment planning systems for proton and carbon beam therapy are commonly based on fast analytic dose engines using pencil beam (PB) algorithms (chapter 2.11.3). Nevertheless there are limitations of PB algorithms concerning heterogeneous media mainly because of the one-dimensional density scaling of particle beams in a medium. Monte Carlo (MC) calculations (chapter 2.11.4) have a superior accuracy due to their more detailed consideration of physical processes, especially in difficult and non-standard treatment situations involving large density and tissue heterogeneities. MC based calculations are already in use for conventional photon therapy. The reason why MC based algorithms are not yet implemented in modern particle treatment planning systems are the limited computer capacities and the much shorter calculation times of PB algorithms. The computation of a particle treatment plan based on MC algorithms takes approximately 10 times longer than PB calculation using standard computer software. With the improvement of computational technology in the last years it is now possible to start implementing MC calculations for particle therapy. For cases in which large dose errors can be expected, the usage of MC dose calculations could be essential to ensure a successful treatment outcome by accepting a presumably longer computation time compared to PB methods.

The objective of this master thesis was the evaluation of the impact of Monte Carlo based calculation in modern proton treatment planning systems. For this purpose, the treatment planning software XiO v4.62 (Elekta AB, Stockholm, Sweden) with a research version of a MC algorithm was tested. Besides general benchmarking of the MC algorithm against the PB algorithm in clinical settings, the aim of this thesis was the identification of an optimal set of treatment planning parameters (peak width multiplier, spot spacing) and MC parameters as e.g. the accepted statistical uncertainty (MCuncertainty, 0.01-0.05), the voxels included in the uncertainty calculation dependent on the maximum deposited energy (MCerror dosethreshold, 0.1-0.6) and the maximum numbers of particles (5×10^3 - 5×10^5). Therefore treatment plans based on different combinations of planning parameters and MC parameters were calculated using the XiO software. The outcome of the PB and the MC based algorithms were compared on the basis of dose calculation time, dose profiles, dose difference maps, γ -index analysis and dosimetric parameters such as conformity index and homogeneity index. In the end a dose calculation was performed using selected patient data sets in order to validate the outcome of the previous test setups which were based on self-made phantoms.

2. Basics of medical radiation physics

2.1 Interaction processes [32], [33], [34]

The photon radiation used in medicine includes low- and high-energy X-rays provided by X-ray tubes and accelerators (10 keV - 50 MeV). Different types of radiation exhibit different energy deposition characteristics. The following subsections describe the different interaction processes of photons and charged particles.

2.2 Interaction processes of photons

The interaction of photon radiation with matter can cause a full or partial absorption of the photon energy or a change of the photon direction (scatter). These types of interactions can lead to the production of charged secondary particles, like electrons or positrons, or uncharged particles like photons. Secondary particles can excite and ionize the surrounding medium. They are able to deposit energy and evoke biological effects by transferring their energy to the medium. Since the ionization is mainly caused indirectly by the generated secondary particles, photon radiation is regarded as indirect ionizing type of radiation.

To describe the interaction processes of photon beams with matter three different stages have to be distinguished: attenuation of the initial photon beam, transformation of the photon energy into kinetic energy and energy absorption within the matter arising from the kinetic energy of secondary particles.

The primary interaction process causes attenuation of the initial photon beam which results in a loss of intensity:

$$I = I_0 * e^{-\mu d} \quad (2.1)$$

$$\mu = \frac{N_A}{A} \rho * \sigma_a \quad (2.2)$$

Equation (2.1) is called Beer-Lambert law named after August Beer and Johann Heinrich Lambert. The attenuation describes the relation of the intensity I after transmission through the absorbing matter with a thickness d to the initial intensity I_0 . The minus sign implies that the number of photons decreases as the thickness of the absorber increases. μ [cm^{-1}] represents the linear attenuation coefficient and is related to the energy of the photons, to the atomic mass A and the density ρ of the material as well as the Avogadro constant N_A ($6.02214129 \cdot 10^{23} \text{ mol}^{-1}$) and the atomic cross section σ_a which describes the likelihood of interaction between particles. The linear attenuation coefficient describes how easily a material can be penetrated by energy or matter. A high attenuation coefficient means that the beam is fast weakened as it passes through the medium and a low attenuation coefficient means that the medium is relatively transparent to the beam.

The linear attenuation coefficient depends on the energy of the photons. Since the attenuation produced by a thickness d depends on the number of electrons presented in that thickness, the linear attenuation coefficient μ depends on the density of the material. The mass attenuation coefficient is independent of the density and its unit is $[\text{cm}^2/\text{g}]$. Tables of photon mass attenuation coefficients are essential in radiological physics.

The attenuation of the photon beam is caused by four major types of interaction which are based on one of the three stages mentioned above:

- Coherent scattering σ_{coh}
- Compton effect (incoherent scattering) σ_c
- Photoelectric effect τ
- Pair production π

These different types of interaction are represented by their own attenuation coefficient σ_{coh} , σ_c , τ and π . The total attenuation mass coefficient is the sum of them:

$$\frac{\mu}{\rho} = \frac{\sigma_{coh}}{\rho} + \frac{\sigma_c}{\rho} + \frac{\tau}{\rho} + \frac{\pi}{\rho} \quad (2.3)$$

2.2.1 Coherent scattering

Coherent scattering, also called classical scattering or Thomson scattering, describes an elastic (no energy loss) interaction that occurs between photons of low energy and materials with a high atomic number. The incoming photon interacts with electrons that are located in the atomic shell, causes electron oscillation and gets scattered. Basically, no energy is lost by the photon as it transfers momentum to the atom while being scattered through the angle φ .

This process can be visualized best by considering the wave nature of photons. The electromagnetic wave passes near the electron, setting it into oscillation. The oscillating electron radiates the energy at the same frequency as the incident electromagnetic wave, emitting a scattered X-ray with the same wavelength as the incident beam (Figure 2.1).

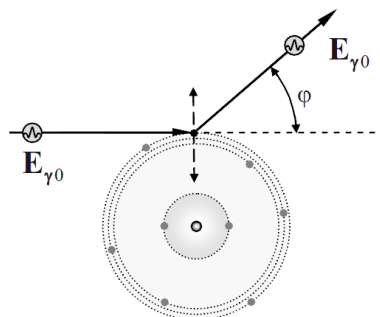


Figure 2.1: Principle of coherent scattering of a photon with the initial and scattered energy $E_{\gamma 0}$ and the scattering angle φ .¹

¹ Extracted from Krieger [34], page 194

The probability of occurrence of coherent scattering is described by the coherent scattering coefficient σ_{coh} . σ_{coh} decreases with the mass number A and with the square of the photon energy E_γ^2 (above 10 keV) and increases with the atomic number Z and the density ρ of the absorber. The coherent scattering coefficient σ_{coh} above 10 keV can be approximated:

$$\sigma_{coh} \propto \rho * \frac{Z^{2.5}}{A * E_\gamma^2} \approx \rho \frac{Z^{1.5}}{E_\gamma^2} \quad (2.4)$$

Coherent scattering occurring in materials with low atomic numbers, such as human tissue or water, is only important for photon energies below 20 keV. Thus, coherent scattering is not relevant in radiation therapy because the dose related to this low energy level of the photons would not lead to any deterioration of the irradiated tissue.

2.2.1 Compton effect

The Compton effect describes the inelastic interaction of a photon with weakly bound electron in an outer shell of the absorber (Figure 2.2). This process can be visualized best by considering the particle nature of photons. The incident photon with an energy of $E = h * \nu$ transmits parts of its energy and its momentum to the electron and is scattered at an angle ϕ . This results in a decrease of the energy (increase in wavelength) of the photon. The electron leaves the atomic shell, with an angle θ relative to the direction of the incident photon. The ejection of the Compton electron leads to an ionization of the atomic shell. Once the Compton electron is ejected from the atom, it loses its kinetic energy through excitation and ionization of atoms in the surrounding material. The Compton scattered photon, on the other hand, can traverse through the medium without interaction or may undergo additional photon interactions.

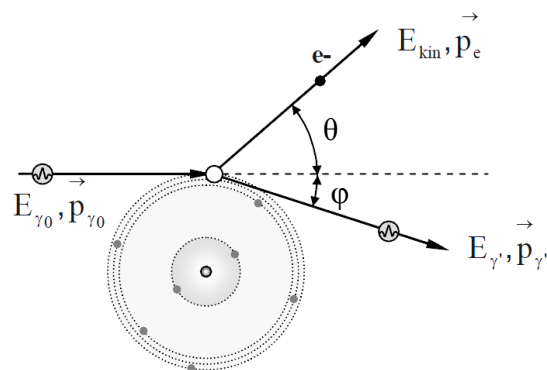


Figure 2.2: Principle of the Compton effect.² The momentum \vec{p} and the photon energy E_γ are transferred to the Compton electron and the scattered photon.

The energy transferred to the Compton electron and the scattering angle depend on the photon energy. Low incident photon energy results in an almost symmetrically scattering of the photons perpendicular to the incident photon direction and even backscattering can take place. With increasing photon energies more scattering occurs in the forward direction (Figure 2.3).

² Extracted from Krieger [34], page 174

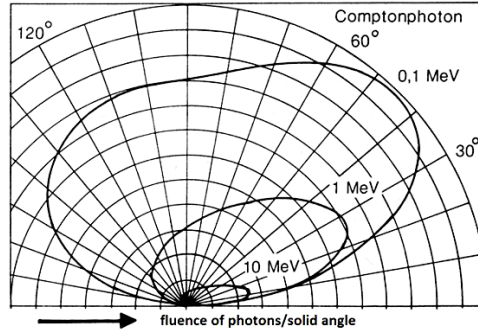


Figure 2.3: Angular distributions of scattered Compton photons with different photon energies.³

The probability of occurrence of the Compton effect is described by the Compton attenuation coefficient σ_c . As two secondary particles are involved in the Compton effect, the Compton attenuation coefficient is composed of the Compton photon scattering coefficient $\sigma_{scatter}$ and the Compton energy transfer coefficient σ_{tr} , which describes the energy transfer of the Compton photon to the electron.

$$\sigma_c = \sigma_{scatter} + \sigma_{tr} \quad (2.5)$$

The Compton attenuation coefficient σ_c is proportional to the ratio of the atomic number and the mass number of the absorber Z/A . For most of the stable, light elements (except hydrogen) the neutron number N is as large as the atomic number Z ($N \approx Z$) and therefore $Z/A \approx 1/2$. Furthermore, the Compton attenuation coefficient increases with the density of the absorber and decreases with the photon energy. A rough estimation for the energy dependence of σ_c can be made for an energy ranging from 0.2 MeV to 10 MeV - this is the region in which the Compton effect is dominant for the majority of materials:

$$\sigma_c = \rho * \frac{Z}{A} * \frac{1}{E_\gamma^n} \quad (n = 0.5-1) \quad (2.6)$$

The energy of the photon after the collision with the electron can be analyzed according to the laws of conservation of momentum and energy. The angle dependent energy of the scattered photon $E'_\nu(\varphi)$ is defined as follows:

$$\text{Photon: } E'_\nu(\varphi) = h * \nu' = \frac{h * \nu}{1 + \frac{h * \nu}{m_e * c^2} * (1 - \cos(\varphi))} \quad (2.7)$$

The energy of the electron is $E'_e(\varphi) = h * \nu - h * \nu'$. m_e corresponds to the mass of the electron. Equation (2.7) with possible values for a φ range from 0° to 180° show that the photon loses no energy when it is scattered in forward direction ($\varphi = 0^\circ$), which means that the electron is emitted at an angle of $\theta = 90^\circ$. As mentioned before, the possibility of scatter in forward direction increases with the increasing energy of the incoming photon (Figure 2.3). The maximum energy transfer to the electron, and thus the maximum reduction in incident photon energy, occurs at an angle of $\varphi = 180^\circ$ (Compton Edge). These equations also show that the Compton electron is never emitted in backward direction.

³ Extracted from Krieger and Petzold [37], page 109

2.2.2 Photoelectric effect

In 1921 Albert Einstein was awarded with the Nobel Prize: "*for his services to Theoretical Physics, and especially for his discovery of the law of the photoelectric effect*" [8], [36]. The photoelectric effect describes the interaction between an incoming photon with an atom that, in the course of this interaction, ejects one of the orbital electrons. The incident photon is completely absorbed and the entire energy of the photon $E = h * \nu$ is transferred to the electron. The electron receives the difference of the photon energy E_γ and electron binding energy E_b as kinetic energy and leaves the atomic shell. Thus, the electron gets ejected from the atom if the photon energy is higher than the binding energy of the electron: $E_\gamma > E_b$.

The kinetic energy of the ejected photoelectron (from the K, L, M, ... shell) is equal to:

$$E_{kin} = E_\gamma - E_b (K, L, M, \dots) \quad (2.8)$$

After the electron is ejected as a secondary particle, a vacancy remains in the inner atomic shell. Due to energetic reasons, the vacancy can be filled by an electron from outer atomic shells generating characteristic X-rays as a consequence of this process. The energy of the characteristic X-rays is dependent on the different binding energies of the electron states in the atomic shells. If the characteristic X-rays are absorbed by another electron of the atom and exceed its binding energy, an Auger electron is created. Thus, the Auger effect, named after Pierre Victor Auger, can be understood as the internal photoelectric effect produced by the interaction of the characteristic X-rays with the same atom.

A depiction of the photoelectric effect is shown in Figure 2.4. In Figure 2.4 i), an electron positioned in the K-shell absorbs the energy of the photon and leaves the atom. The vacancy is filled with an electron of the L-shell resulting in characteristic X-ray, as shown in Figure 2.4 ii).

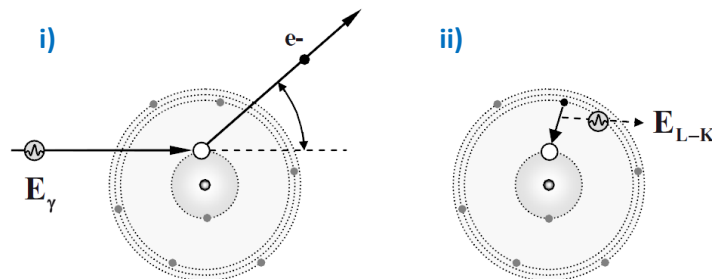


Figure 2.4: Principle of the photoelectric effect.⁴

The photo absorption coefficient τ describes the probability of the photoelectric effect. τ increases with the density ρ of the absorber and with the electron density in the inner shells, which is approximately proportional to Z^3 . Furthermore, the interaction probability increases with the bigger electron binding in heavier atoms and is highest for K-electrons in dense absorbers with high atomic number. About 80% of all photon interaction effects take place in the K-shell and the remaining 20% take place in outer shells. Since these outer electrons see a reduced nuclear charge due to the shielding by the K-electrons, a more accurate estimation can

⁴ Extracted from Krieger [34], page 169

be carried out. Thus, the total photon interaction probability increases approximately with a Z -potency between 4 and 4.5. Furthermore, the photo absorption coefficient is energy dependent. The probability of photon absorption is highest, when the energy of the photon and the electron shell are equal. Therefore, the photo absorption coefficient reaches a maximum at the energy of the inner electron shell (K-shell), falls off rapidly after exceeding this energy level and increases again at the next energy level of the next electron shell (L-shell). These discontinuities are called absorption edges and are shown in Figure 2.5.

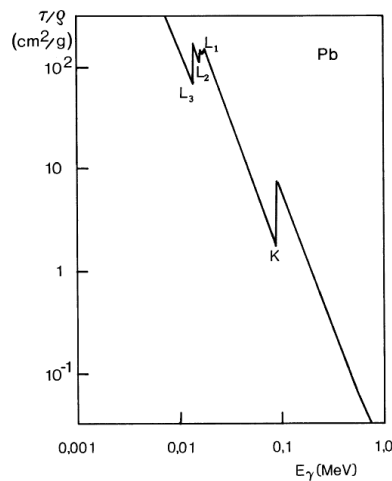


Figure 2.5: Illustration of the energy dependence of the mass photon absorption coefficient for lead.⁵

Low photon energies emit photo electrons nearly perpendicular relative to the incident photon beam direction. The higher the photon energy is the smaller is the emission angle of the photo electron that tends to the forward direction.

2.2.3 Pair production

If the energy of a photon exceeds 1.022 MeV, the photon can interact with matter through the mechanism of pair production. This high-energy photon, under the influence of the atomic nucleus, is converted into an elementary particle and its antiparticle, namely an electron and a positron (Figure 2.6). The photon is completely absorbed and transfers all its energy to the particle/antiparticle pair.

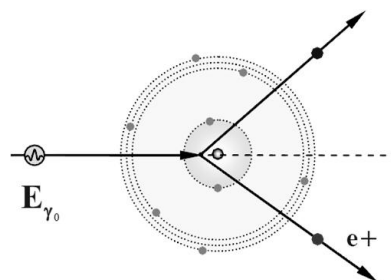


Figure 2.6: Principle of pair production.⁶

⁵ Extracted from Krieger [34], page 171

⁶ Extracted from Krieger [34], page 191

The energy of 1.022 MeV is equal to the rest mass m_0 energy equivalent of the positron-electron pair.

$$E_{kin} = E_\gamma - 2m_0c^2 = E_\gamma - 1.022 \text{ MeV} \quad (2.9)$$

The positively charged positron receives a slightly higher kinetic energy because of the rejection by the positive electric field of the atomic nucleus. The negatively charged electron is slowed by the nuclear attraction. For reasons of conservation of the momentum, the particles are emitted in forward direction.

The probability of pair production is described by the pair production coefficient π and increases with the density ρ of the absorbing material, the quotient Z^2/A and the logarithm of the photons' energy E_γ .

$$\pi \propto \rho * \frac{Z^2}{A} * \log(E_\gamma) \quad (2.10)$$

After their creation, the electron and the positron move through the absorber and transfer their kinetic energy to the surrounding medium. When the positron loses enough energy, it recombines with a shell electron of the absorber. The rest mass of the two particles is then converted into two 511 keV photons. These two photons of the annihilation radiation are emitted at an angle of 180° with respect to each other.

2.2.4 Relevance of the various processes

The previous chapters described the various interactions of photons and specified the mass attenuation coefficients depending on the atomic number and the energy of the photon. These dependencies are summarized for a more detailed assessment:

Type of interaction	f(Z,A)	f(E _γ)	Secondary radiation
Coherent scattering	$Z^{2.5}/A$	$1/E_\gamma^2$	γ
Photoelectric effect	$Z^4/A - Z^{4.5}/A$	$1/E_\gamma^3$ for $E_\gamma \ll 5.11 \text{ keV}$ $1/E_\gamma$ for $E_\gamma \gg 5.11 \text{ keV}$	Electron, X-ray, Auger-electron
Compton effect	Z/A	$1/E_\gamma^{0.5} - 1/E_\gamma$	γ , Electron
Pair Production	Z^2/A	$\log E_\gamma$ ($E_\gamma > 1022 \text{ keV}$)	Electron, positron

Table 2.1: Approximate dependencies of the attenuation coefficient in relation to the Photon energy E_γ , atomic number Z and mass number A of the absorber. All coefficients are proportional to the density ρ of the absorber.⁷

Photon energy in radiation therapy ranges from 6 MeV – 18 MeV. For imaging purposes the photon energy is several 100 keV. The energy of the photon E_γ , the atomic number Z and the mass number A of the irradiated material decide which type of interaction process is the dominant one. The respective process is responsible for the attenuation, the energy transfer and the absorption of the photon radiation. Figure 2.7 shows the dominant photon interaction type depending on the energy and the atomic number.

⁷ Extracted from Krieger [34], page 199

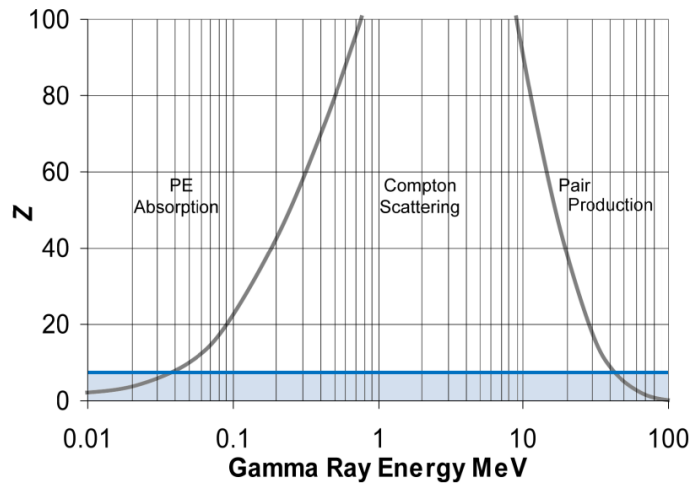


Figure 2.7: Different photon interactions as a function of the atomic number and the gamma-ray energy. The blue area depicts the relevant part for human tissue ($Z=7$).⁸

Table 2.1 and Figure 2.7 show that the photoelectric effect is dominant for low energies up to 1 MeV. Thus, this effect is almost insignificant in radiation therapy, except for X-ray diagnostic, due to the small photon energies. The protective effect of lead, tungsten or uranium as shielding materials for radiation protection (high Z) for diagnostic X-rays (low photon energy) is therefore based predominantly on the photoelectric effect. For a broad range of photon energies and low atomic numbers the Compton effect is the dominant interaction process and plays a major role for therapeutic and diagnostic photon radiation. Human tissue is the most important absorber in medicine. It is nearly equivalent to water, with an effective atomic number of 7 to 8. Therefore, the Compton effect is the predominant interaction process concerning human tissue, as shown in Figure 2.8. Pair production only becomes relevant for materials with high atomic number and energies from 10 MeV on. For heavy absorbers with $Z > 20$ pair production is an important interaction process, but thus negligible for human tissue.

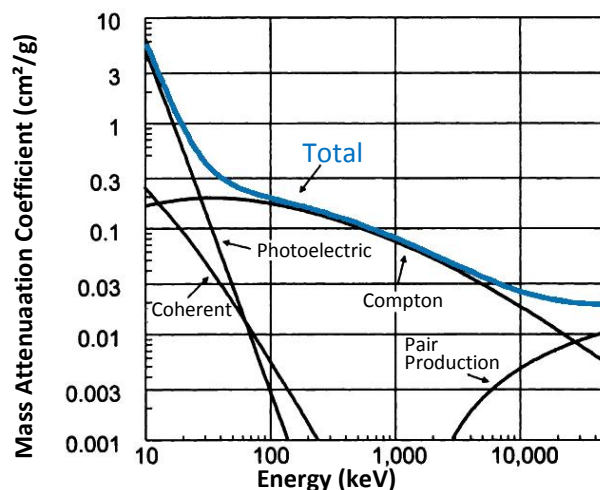


Figure 2.8: Coherent scattering, photoelectric, Compton, pair production and total mass attenuation coefficients for soft tissue ($Z=7$) as a function of energy.⁹

⁸ Extracted from http://petrowiki.org/images/a/a6/Vol5_Page_0254_Image_0001.png, 27.01.2015

⁹ Extracted from Bushberg [38], page 467

2.3 Interaction processes of charged particles

In this chapter an overview about the interaction processes of charged particles, like protons, electrons and other ion species is given. One fundamental advantage of charged particles is the energy deposition in comparison to other types of therapeutic radiation such as photons. In comparison to photons, charged particles are directly ionizing and have a reduced deflection when traversing through matter, due to their higher mass. Furthermore, the energy deposition of charged particles increases with penetration depth and rises sharply to a maximum, the so called Bragg peak, close to the end of the particles range. The involved processes are of statistical nature; therefore it is not possible to determine the exact range of charged particles. This range difference between the mean particle range and the actual particle range is called range-straggling and depends primarily on the particle mass.

2.3.1 Stopping power

The stopping power describes the deceleration of charged particles due to their interaction with matter, which results in a loss of particle energy. The stopping power of the absorbing material is numerically equal to the loss of the energy E per unit path length x .

The stopping power depends on the energy and the type of the radiation and on the properties of the material that it passed. The total stopping power $S_{tot}(E)$ of a material is the sum of the collision stopping power S_{col} and radiation stopping power S_{rad} and is defined as follows:

$$S_{tot}(E) = \left(\frac{dE}{dx}\right) = S_{col} + S_{rad} \quad (2.11)$$

The collision stopping power is characteristic for the absorber material and describes the energy absorption by matter, as shown in formula (2.12).

$$S_{col} = \left(\frac{dE}{dx}\right)_{col} \propto \rho \frac{Z}{A} * \frac{z^2}{v^2} \quad (2.12)$$

The collision stopping power depends on the density ρ and the ratio Z/A of the target material. Furthermore, S_{col} increases with the square of the charge z and for non-relativistic particle-energies S_{col} decreases quadratically with the velocity of the particle which leads to a quadratic increase of the energy loss per unit path length. This behavior explains the shape of the Bragg peak showing a steep rise and fall-off at the end of a particle's range (Figure 2.9). The energy deposition reaches a maximum shortly before the energy drops to zero, indicating that the energy loss corresponding to the relative dose is a function of the penetration depth.

The second term refers to the radiation stopping power S_{rad} , which describes the deceleration of charged particles by the Coulomb field of particles in the material traversed. Thereby, charged particles can lose some of their kinetic energy by photon radiation (Bremsstrahlung). The energy loss is higher, the larger the deflection angle and the closer the charged particle is to the nucleus or other deflecting particles. If electrons are used as projectiles, radiative stopping is always

important. Otherwise, radiation stopping power is only relevant at extremely high ion energies, where energy loss due to nuclear reactions can occur.

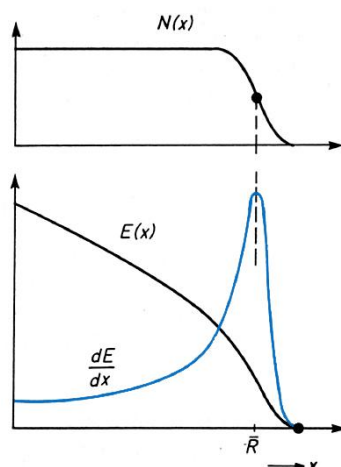


Figure 2.9: Amount of particles N and energy losses as a function of the penetration depth.¹⁰

2.3.2 Linear energy transfer (LET) [39]

The term Linear Energy Transfer (LET) was first introduced by Zirkle et al. in 1952 [40]. The LET is closely related to the stopping power of a material (chapter 2.3.1). While the stopping power describes the total energy loss of a particle that passes through matter, the LET describes the energy loss of secondary electrons in immediate vicinity of the particle track. Thus, the LET depends on the nature of the particle as well as on the material traversed.

To describe the LET, a distinction between unrestricted and restricted LET has to be done. The unrestricted LET takes every secondary electron (generated by ionizing particles) into account. The restricted LET on the other hand considers only secondary electrons up to a specific energy limit. This is done in order to exclude higher energetic secondary electrons - the so called delta electrons - which are capable to ionize matter by themselves.

The LET is not a constant value. As mentioned before, it depends on the charge and the energy of the particle and varies with the particle type. A high LET value attenuates the beam quickly, and prevents a deep penetration of the beam. Furthermore, a high LET value means a higher concentration of deposited energy, which can cause more severe damage to the tissue near the particle track. Thus, the LET helps to explain why radiation damage is sometimes disproportionate to the absorbed dose.

¹⁰ Extracted from Krieger and Petzold [37], page 191

2.3.3 Relative biological effectiveness (RBE)

The term Relative Biological Effectiveness (RBE) was first used by Failla and Henshaw in 1931 who described the RBE of X-rays and γ -rays [41]. The RBE is a quantity that describes the biological effect originating from different types of radiation. The RBE is defined as the ratio of biological effectiveness of one type of ionizing radiation (reference radiation D_{ref}), which causes a specific biological effect, related to another comparative radiation D_U , which is necessary for the occurrence of the same effect under the same conditions on the same biological object, as shown in formula (2.13). The reference radiation is usually a low LET radiation, such as 250 kV X-rays or the gamma radiation of ^{60}Co ($E_\gamma = 1.17$ and 1.33 MeV).

$$RBE = \frac{D_{Ref}}{D_U} \quad (2.13)$$

Figure 2.10 i) shows a cell survival curve and Figure 2.10 ii) shows a dose-response curve for determining the RBE. The RBE values in these graphical examples were calculated according to formula (2.13), resulting in numbers higher than 1. The RBE is considered as 1 for photons and 1.1 for protons [42], [43]. The RBE of carbon ions is more complex and changes with the energy and the tissue density [44]. Carbon ions have a higher RBE than photons and protons which means an increased efficiency of cell killing. For therapeutic purposes correctly determined RBE values are essential. Different RBE values of different radiation types could be explained by the transfer of their energy to the tissue in different ways. Massive particles like alpha particles and neutrons have a high RBE and leave a dense trail of ionized atoms in their path, while photons and beta particles have a low RBE, resulting in a spacious ionization along their path.

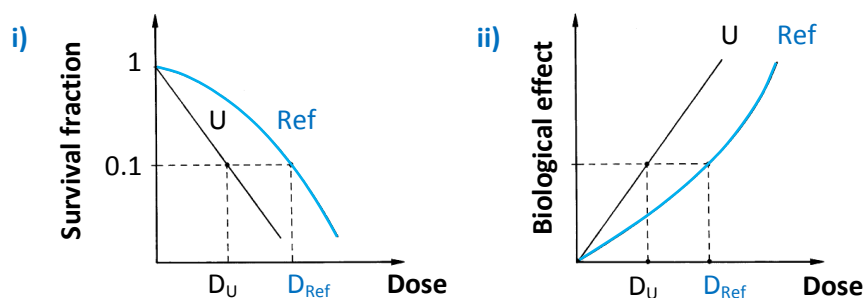


Figure 2.10: Determining the RBE on the basis of i) cell survival curves and ii) dose-response curves. The reference radiation "Ref" required for a particular biological effect generates a higher dose in comparison to radiation "U", which generates a smaller dose for a given effect.¹¹

The RBE changes with experimental conditions, as it depends on the dose rate, the oxygen environment, the observed biological effect and the cell type. All these effects have to be considered when determining the RBE of a certain radiation.

¹¹ Extracted from Krieger [34], page 467

2.4 Comparison of protons and photons

The main difference between protons and photons is the Bragg peak, which could probably result in a reduction of the integral dose to healthy tissue outside the target volume for protons. When photons traverse through biological tissue, stochastic events like absorption and scattering processes occur. Hence, the photon beam spreads quickly after entering the tissue and has no defined range in comparison to the proton beam, as shown in Figure 2.11 i). The curve progression of the photon beam shows an initial build up followed by an exponentially dose decrease. Proton beams on the other hand feature a finite range and show less scattering compared to photons due to their mass. The depth-dose distribution of protons shows a slight increase with a higher penetration depth and a steep rise and fall-off towards the end of the particle's range (Bragg peak). This is shown Figure 2.11 ii), where a spread out Bragg peak (SOBP) is pictured as well. The SOBP is the sum of several individual Bragg peaks at graded depths and is formed in order to create a uniform dose region with a defined extent.

Protons lose their energy and consequently their velocity not only by Coulomb interactions but also by nuclear interactions [42] which results in secondary radiation. Secondary neutrons can be generated by interactions of the protons with scattering and collimating beam elements. Shielding against secondary neutron radiation is therefore important for any proton therapy installation.

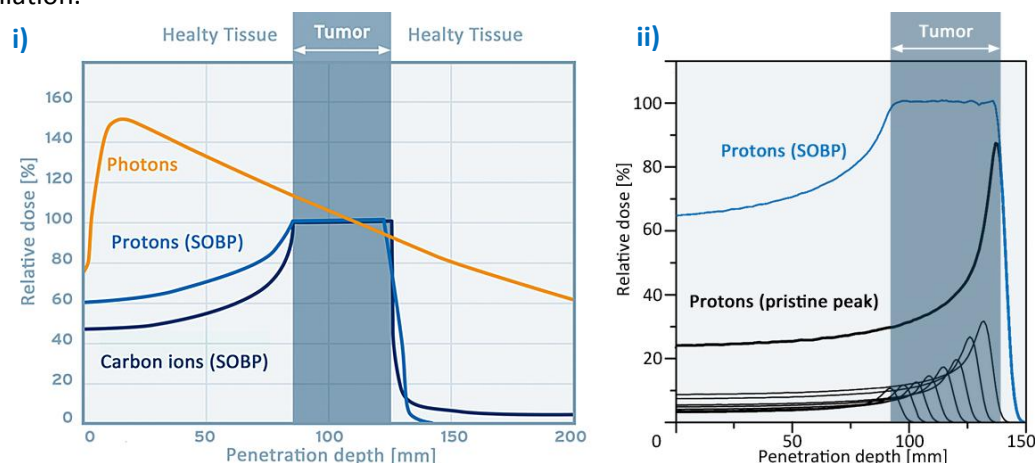


Figure 2.11: i) Relative dose as a function of the penetration depth of photons, protons and carbon ions.¹² ii) Spread out Bragg peak.

One source of potential errors in proton therapy has its origin in existence of inhomogeneities. In general, bone, air cavities, or other tissue inhomogeneities produce greater dose distribution perturbations in a proton treatment plan than in a photon treatment plan. While heterogeneities alter the dose distributions of photon plans by a few per cent, their influence on charged particle beams can be huge. In the worst case, it can result in near zero dose delivered to parts of the target volume, or even to unintended treatment of the full target dose to critical structures distal to the target volume. Thus, air cavities close to the target volume pose a great challenge, as no interaction takes place which results in an extended range of the protons.

¹² Extracted from <http://www.medastron.at/service/presse/bilder/grafiken/>, 27.01.2015

2.5 Comparison of protons and heavier ions [46], [47]

As mentioned in chapter 2.3.3, the RBE of heavier ions is higher than that of protons, which leads to an increase of the biological effectiveness in terms of malignant cell death. Hence, a lower physical dose is required when using heavy ion beams to produce the same cell damage. On the other hand heavier ions produce secondary particles, which produce a noticeable dose deposition behind the Bragg peak, as shown in Figure 2.11 i). This effect known as the fragmentation tail is even more pronounced for heavier particles and might damage the healthy tissue behind the tumor during treatment.

In recent times, carbon ions ($Z=6$) have become of interest because of their LET-properties that are almost comparable to those of neutrons. Carbon ions have a high-LET behavior (which corresponds to a high RBE) within the Bragg peak due to the higher ionization densities and a low-LET quality at the entrance region of the biological tissue. Protons in comparison are characterized by a lower LET. As mentioned in chapter 2.3, the range of the particles deviates slightly from the mean particle range due to the involved statistical nature of the processes. When particles traverse the same distances in matter, the number of collisions depends on the ion type. Different numbers of collisions cause varying ranges. This range differences are called range-straggling and depend primarily on the particle mass. For protons range-straggling amounts to approximately 1% of the mean particle range [48]. For heavier particles range-straggling is decreased inversely with the square-root of the particle mass, resulting in a more pronounced, sharper Bragg peak, as can be observed in Figure 2.11. Thus, the heavier the particle is, the less range-straggling occurs. Helium, for example, shows only 50% of the range-straggling the proton exhibits and neon approximately 22%. This fact can be explained due to the higher amount of mass which avoids deflection after the collision with other particles and thereby reduces range-straggling. From a therapeutic point of view, the reduced range-straggling of heavier ions allows a higher precision of the treatment and a potential improvement of the sparing of healthy tissue surrounding the target volume.

2.6 Dosimetric quantities [32], [37]

All radiation effects in humans are based on the absorption of radiation in tissue. The fundamental physical dose quantity is therefore the absorbed dose, which describes the absorbed energy per unit mass. In radiation therapy, the absorbed dose is used for prescribing a dose to a patient for tumor treatment using a treatment planning system and the following dose calculation. For delivering the prescribed dose to the patient, different techniques in external beam therapy or brachytherapy used for different types of radiation are utilized.

The correlation between the applied dose and the resulting response (biological effect, cancer probability, etc.) is described by dose-response curves. Tumor treatment is only possible due to different dose-response curves of healthy tissue and tumor tissue, as shown in Figure 2.12 i). A certain dose D is applied to the patient, which results in a higher response R_2 of the tumor tissue than the response R_1 of the normal tissue. Since a small volume of normal tissue receives dose as well there is always a small probability of late normal tissue damage.

In order to make precise statements concerning the impact of radiation on tissue, exact measurement and calculation of the absorbed dose is particularly important, as shown in Figure 2.12 ii). It can be seen, that a small change ΔD in the dose results into a major change ΔR in the effect.

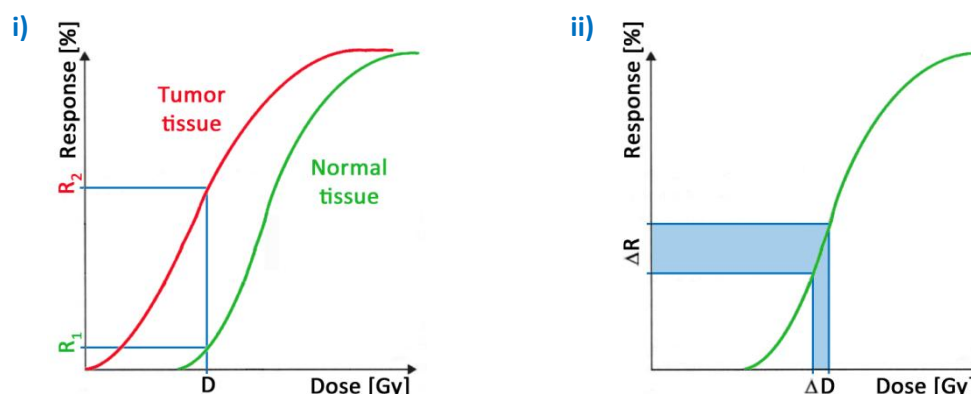


Figure 2.12: Dose-response curves showing i) the impact of a dose D on normal and tumor tissue and ii) the impact of varying doses on the response.

For detecting the absorbed dose, different physical effects like ionization of gases or solids (ionization chamber and semiconductor detector), luminescence (thermoluminescence detector), heat (dose calorimeter) can be used. Furthermore, chemical methods (photographic film) can be applied.

For measuring the basic beam characteristics, 3D water phantoms are used in radiation therapy. A water phantom consists of an acrylic glass container filled with distilled water as the density and the characteristics of water are comparable to those of body tissue. A radiation detector array measures the beam profile on basis of depth dose profiles and longitudinal dose profiles.

In general, dosimetric quantities are required for dose calculation using a treatment planning system and to assess the radiation exposure to human tissue in a quantitative way. These quantities can either be of biological nature (e.g. equivalent dose, effective dose) considering stochastic health effects on human tissue (e.g. relative biological effectiveness, see chapter 2.3.3) via radiation weighting factors, or of physical nature, considering only the characteristics of the radiation. In this chapter physical dose quantities will be discussed, further information about biological quantities can be found in [32].

Absorbed dose

The absorbed dose D is a physical dose quantity that describes the mean energy dE transferred to matter per unit mass dm through ionizing radiation.

$$D = \frac{dE}{dm} = \frac{1}{\rho} * \frac{dE}{dV} \quad (2.14)$$

The unit of the absorbed dose is Gray [J/kg]. The absorbed dose is important for calculating radiation exposure and is therefore essential in radiologic protection.

Kerma

One interaction of indirectly ionizing radiation with matter is the transformation of energy into kinetic energy E_{kin} of charged secondary particles. The energy transferred to secondary electrons is of particular interest in dosimetry because the electrons will impart their energies close to the point where they were released and can best be described with a physical quantity called Kerma (kinetic energy released per unit mass). The unit of kerma is Gray [J/kg].

“The kerma, K , is the quotient of dE_{tr} by dm , where dE_{tr} is the sum of the initial kinetic energies of all the charged particles liberated by uncharged particles in a mass dm of material, thus” (ICRU60 [35])

$$K = \frac{dE_{tr}}{dm} \quad (2.15)$$

2.7 Beam delivery [31], [49], [50]

Currently, two proton-beam delivery methods are available: passive scattering and active scanning. In passive beam delivery, scattering elements and a series of blocks and apertures are used to cover the whole tumor volume in order to achieve appropriate dose conformity. Active beam delivery on the other hand uses a narrow pencil beam for “scanning” the whole tumor volume.

2.7.1 Passive scattering

The passive scattering technique uses external scattering materials (e.g. scattering foils) in order to spread out the narrow beams up to the size of the target volume. Normally, two scattering foils are used to increase the width of the primary beam, as shown in Figure 2.13.

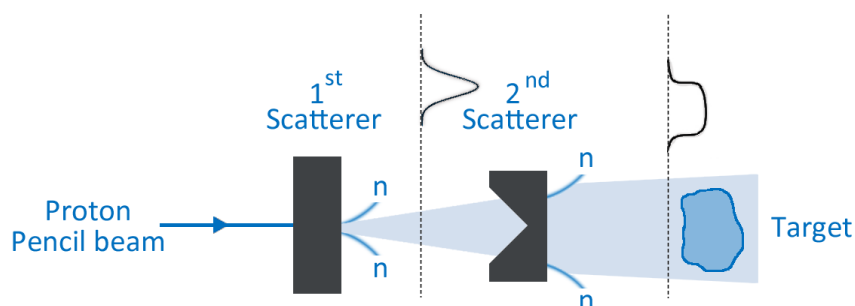


Figure 2.13: Principle of passive scattering proton beam delivery.¹³

The spread out Bragg peak (SOBP) is obtained via a set of range modulator wheels or ridge filters inside the nozzle of the delivery system. The range modulator wheel is a rotating disc of varying thickness that alters the range of the proton beam. A combination of patient-specific collimators and compensators conform the dose to the target volume laterally and distally.

One disadvantage of passive scattering is that the fluence is constant across the treatment field and therefore no intensity modulation can be realized. Further a certain amount of dose is delivered proximal to the target volume. Another disadvantage is caused by the usage of scattering foils for the production of the required field size. When the proton beam hits the scattering material, secondary neutrons are generated. When using the passive scattering technique, doses distant from the field edge, 10 times higher than those characteristic for IMRT with X-rays can occur [50]. Limiting the neutron production is especially important when children are treated, who have an increased risk of developing neutron-induced secondary cancers later in life. One advantage of the passive scattering technique is the less complex treatment planning process in comparison to scanning and there are fewer variables to consider in treatment planning. Thus, passive scattering is a more robust technique compared to active scanning.

¹³ Based on Hall [50], page 6

2.7.2 Active scanning

Active Scanning uses narrow mono-energetic pencil beams that are scanned over the target volume by deflection using magnets. One possible scanning pattern is a zigzag pattern, where the beam is scanned perpendicular to the beam direction. Thereby, the scanning can start with the deepest layer (highest energy) and does one x-y scan. Then the energy is reduced (higher layer) and this procedure is repeated until the whole target volume is covered (Figure 2.14). To reduce uncertainties and delivery errors each layer can be addressed several times. This is called re-scanning. While the beam is swept across the target volume, the dose deposition takes place in small spots. Up to several thousand narrow particle beams (spots) are used for the target irradiation. Similar to the passive scattering technique, scattering materials are used to spread the beam to a wider Gaussian shape (SOBP) in order to reduce the irradiation time and to facilitate a coverage of the whole target using a reasonable number of spots. As shown in Figure 2.14 range shifter plates can be used to broaden the spot size of the beam.

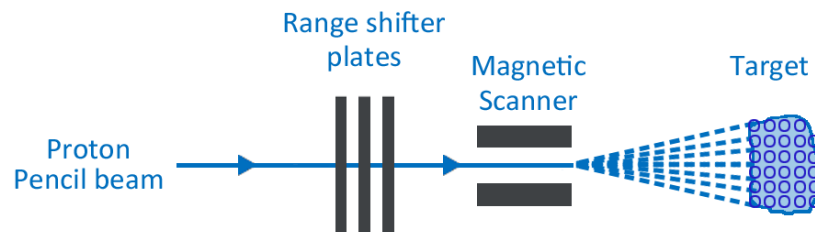


Figure 2.14: Principle of active scanning proton beam delivery.¹⁴

The usage of variable initial particle energies is in direct contrast to the passive scattering technique that cannot conform the dose distribution to both distal and proximal edges of the target volume. Furthermore, the depth of dose deposition can be precisely modified, the scattered radiation is reduced and the active scanning technique enables the application of intensity-modulated treatment methods. Fluence modulation can be achieved through the speed of the scan or the modulation of the output of the source or both.

¹⁴ Based on Hall [50], page 6

2.8 Treatment planning principles

Treatment planning systems allow simulating multiple treatment scenarios for a given patient in order to achieve a final treatment plan that satisfies the therapeutic aim.

One basic input any treatment planning system requires is the patients' anatomical data which can be received by imaging modalities like CT, MRI and PET. For dose calculation CT density data are required. Heterogeneity corrections are necessary to perform a calibration to obtain a relationship between electron densities (or proton stopping powers for proton radiotherapy) and the corresponding Hounsfield units (HU). Thus, Hounsfield units (HU) represent a quantitative scale for describing the radiodensity of the materials and allow a more precise dose calculation.

Furthermore, treatment planning systems require contouring anatomy (chapter 2.9), beam selections and different treatment techniques (chapter 2.10), dose calculation (chapter 2.11), optimization (chapter 2.12) and dose analysis tools (chapter 2.13). The generated treatment plan includes the final prescription as well as all technical data required for the treatment delivery. Examples of technical data are: structure of the beam delivery system, the number of beams and their directions and the number of beam segments and their intensity, dose distributions and the aperture shapes or multileaf collimator settings, etc. At least two systems are required to perform radiation therapy: a treatment planning system (chapter 3.2) able to calculate non-uniform fluence maps and a system to deliver these fluence maps as planned. For treatment plan calculation, planning constraints are given and the plan is optimized in order to deliver a high dose to the target volume and an acceptably low dose to the surrounding healthy structures. This guiding principle is known as "ALARA"-principle. ALARA is an acronym for "As Low As Reasonably Achievable", which means making every reasonable effort to maintain exposures to ionizing radiation as far below the dose limits as practical and represents a regulatory requirement for all radiation safety programs and is defined as following:

"For all medical exposure of individuals for radiotherapeutic purposes, [...] exposures of target volumes shall be individually planned; taking into account that doses of non-target volumes and tissues shall be as low as reasonably achievable and consistent with the intended radiotherapeutic purpose of the exposure." (Directive 97/43/EURATOM, Article 4)

2.9 Volume concepts [51]

The aim of any radiotherapy treatment is to homogeneously deliver the prescribed dose to the target volume containing the tumor while limiting the dose to the adjacent healthy tissue. Therefore it is important to accurately localize the tumor and the adjacent critical tissues. With the help of imaging modalities like CT, MRI and PET the position and the size of the tumor volume are defined. Different volumes related to both tumor and normal tissues have been defined in several ICRU Reports for use in the treatment planning process. The ICRU reports 50 and 62 [52], provide precise information for conventional radiotherapy treatment and the ICRU report 83 [53], which discusses volumes and guidelines when performing IMRT, advances some of these concepts even further. Delineating these volumes is an obligatory step in the planning process, as dose cannot be prescribed without specification of target volumes and not optimized and reported without the delineation of so called organs at risk (OARs). On the basis of the high quality 3D images the visible tumor and OARs are outlined slice by slice. Furthermore, the received dose of the organs at risk should be “As Low As Reasonably Achievable”. As mentioned before, this guideline is also known as the “ALARA”-principle. Thus, sufficient dose coverage of the planning target volume and a satisfying organ at risk dose sparing is a complex balancing act. In order to use the potential advantage of protons, the range of proton beams in patients needs to be predicted and assured as accurate as possible. Thus, an improper quantification of safety margins added to the target volume, as for example wrong positioning of the patient or a change in the anatomical geometry can have more severe consequences in proton therapy than in photon therapy. Margins that underestimate the uncertainties in photon therapy might cause underdosage of the tumor. Applied to proton therapy, such an underestimation can cause part of the tumor receiving much less dose than prescribed due to a potential shift of the sharp distal dose falloff towards adjacent OARs.

2.9.1 Volume types

Figure 2.15 displays different treatment volumes that are used in the treatment planning process.

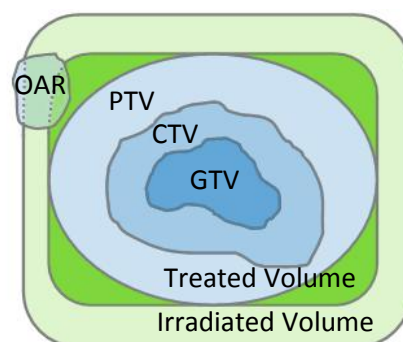


Figure 2.15: Various treatment volumes

Gross tumor volume (GTV)

The GTV describes the visible extent and location of malignant growth, and is defined as:

„The Gross Tumor Volume (GTV) is the gross demonstrable extent and location of the tumor. The GTV may consist of a primary tumor (primary tumor GTV or GTV-T), metastatic regional node(s) (nodal GTV or GTV-N), or distant metastasis (metastatic GTV, or GTV-M).” (ICRU Report No. 83 [53])

The GTV may appear to be different in shape and size, depending on what imaging modality is used. Therefore, the radiation oncologist should indicate which method has been used for the delineation of the GTV.

Clinical target volume (CTV)

The CTV contains the GTV and includes an area directly surrounding the GTV. This additional volume may contain microscopic malignant disease and other areas that are considered to be at risk and which require treatment.

“The Clinical Target Volume (CTV) is a volume of tissue that contains a demonstrable GTV and/or subclinical malignant disease with a certain probability of occurrence considered relevant for therapy.” (ICRU Report No. 83 [53])

“This volume thus has to be treated adequately in order to achieve the aim of therapy: cure or palliation.” (ICRU Report No. 50 [52])

The delineation of the GTV and the CTV should be independent of the irradiation technique and should only be influenced by oncological considerations.

Planning target volume (PTV)

The PTV includes an external margin for setup uncertainties and an internal margin which takes organ motion into account in order to ensure that the prescribed dose is actually absorbed in the CTV. In contrast to the CTV the PTV is a geometrical concept and can depend on the irradiation technique. The PTV is defined as followed:

“The Planning Target Volume is a geometrical concept introduced for treatment planning and evaluation. It is the recommended tool to shape dose distributions to ensure that the prescribed dose will actually be delivered to all parts of the CTV with a clinically acceptable probability, despite geometrical uncertainties such as organ motion and setup variations. It is also used for dose prescription and reporting. It surrounds the representation of the CTV with a margin such that the planned dose is delivered to the CTV. This margin takes into account both the internal and the setup uncertainties. The setup margin accounts specifically for uncertainties in patient positioning and alignment of the therapeutic beams during the treatment planning, and through all treatment sessions.” (ICRU Report No. 83 [53])

Treated volume (TV)

Due to the limitations of irradiation techniques the volume receiving the prescribed dose may be larger and of a simpler shape than the PTV. Therefore, the TV also depends on the irradiation technique and represents the volume that is enclosed by a specific isodose and is defined as followed:

“The Treated Volume (TV) is the volume of tissue enclosed within a specific isodose envelope, with the dose specified by the radiation oncology team as appropriate to achieve tumor eradication or palliation, within the bounds of acceptable complications.” (ICRU Report No. 83 [53])

Irradiated volume

The irradiated volume depends on the irradiation technique and is defined as followed:

“The Irradiated Volume is the tissue volume that receives a dose that is considered significant in relation to normal tissue tolerance.” (ICRU Report No. 50 [53])

Organs at risk (OAR)

OARs are healthy organs which might be damaged during treatment.

“The organs at risk (OAR) or critical normal structures are tissues, which if irradiated could suffer significant morbidity, and thus might influence the treatment planning and/or the dose prescription. In principle, all non-target tissues could be organs at risk. However, normal tissues considered as OARs typically depend on the location of the CTV and/or the prescribed dose.” (ICRU Report No. 83 [53])

Sparing OARs is an important component in radiotherapy treatment planning. Therefore, a balance between proper dose coverage of the PTV and an adequate OAR dose sparing has to be achieved.

2.10 Treatment techniques [48], [54] - [56]

Several different treatment techniques are described in this chapter. Conformal radiotherapy (CRT) and single-field uniform dose (SFUD) radiotherapy uses the so called “forward planning” approach whereas intensity modulated radiation therapy (IMRT) or intensity modulated proton therapy (IMPT) uses the “inverse planning” approach.

2.10.1 Conformal radiotherapy (CRT)

Conformal radiotherapy (CRT) uses a beam of uniform intensity, which delivers a constant photon fluence and uniform doses across the treatment field. The ability for conformal radiotherapy to alter dose distributions is limited to shaping field boundaries with collimators, blocks or multileaf collimators (MLCs), the use of wedge filters or compensators for missing tissues and central blocks for shielding critical structures.

Beam directions and beam weights as well as wedge filters and collimator shapes have to be defined by the planner. The field of the MLC field is primarily determined by the shape of the target volume and the shape of the MLC can be manually reduced or enlarged at certain positions. As mentioned above, CRT uses the “forward planning” approach. This means that the prescribed dose for each beam, the beam directions and the multileaf collimator configurations have to be adjusted.

2.10.2 Single-field uniform dose (SFUD)

The single-field uniform dose (SFUD) method is a treatment planning technique for light ions and protons and can be performed with both passive scattering and active scanning and represents a robust method in a short time.

When using SFUD, each beam is optimized independently for its spot positions and weights in such a way that each beam alone will provide homogenous and uniform dose coverage of the target volume. Each beam is then weighted manually and all beams are summed up.

Single-field uniform dose is used because it allows each field to deliver the prescribed dose to the entire target volume by itself and is therefore less sensitive to proton-range uncertainties than IMPT. IMPT is similar to SFUD as both techniques are based on the modulation of individual Bragg peaks. The difference between SFUD and IMPT is that in SFUD the fields are optimized individually, whereas in IMPT the Bragg peaks are optimized concurrently focusing on explicit OAR sparing. As mentioned before, one advantage of SFUD is the robustness of the SFUD plan. One disadvantage of SFUD is its limited ability to spare organs at risks especially when they are located proximal to the target.

2.10.3 Intensity modulated radiation therapy (IMRT) and intensity modulated particle therapy (IMPT) [49]

In intensity modulated radiation therapy (IMRT) a non-uniform fluence is delivered to the patient. Furthermore, different beam directions are chosen manually to generate the desired dose distribution. To produce intensity modulated fluence profiles, the linear accelerator has to be equipped with a system capable of transforming the beam profile into a profile of any shape - a computer controlled multileaf collimator (MLC). The MLCs define and subdivide the beam into so called beamlets with uniform beam intensities, which form the basis for the variation in the fluence. During the optimization the treatment-planning algorithm determines the optimal setting of the fluences or weights of the beamlets to satisfy predefined dose distribution criteria. For a set of beam directions an optimal fluence profile can be calculated using the inverse planning approach. Thus, with inverse planning, the user does not directly optimize or re-adjust beam intensities. That means, that inverse planning modifies the beam intensities based on the calculated dose distribution, including any imperfections in the calculation, and it is important that the calculation is accurate at all points.

A comparison between conformal radiotherapy and IMRT is shown in Figure 2.16. As mentioned before only a constant photon fluence and uniform dose can be delivered when using conformal radiotherapy. IMRT, on the other hand, uses beams that have highly non-uniform beam intensities.

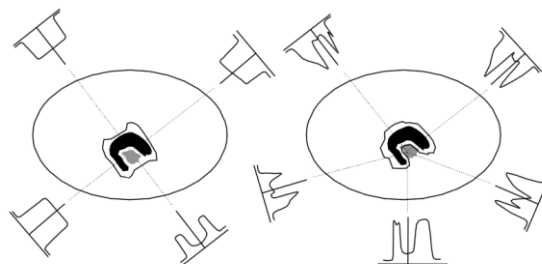


Figure 2.16: Difference between conformal radiotherapy (left) which uses the forward planning approach and IMRT (right) which uses the inverse planning approach.¹⁵

One advantage of using non-uniform beam intensities is the better conformation of dose distributions to the target volume caused by varying the fluence of the primary beams. Furthermore, a reduction of the dose to the adjacent healthy tissue can be achieved.

Intensity modulated particle therapy (IMPT) follows a similar approach as IMRT. In comparison to IMRT, IMPT has an additional degree of freedom because of the finite range of the charged particles. The extra degree of freedom increases its dose-shaping potential, which could potentially result in a reduction of the dose received by healthy tissue but also increases the computational and delivery complexity. IMPT is performed in combination with the active scanning technique (chapter 2.7.2) and it is a method that optimizes all treatment fields in a plan including all scanned spots at the same time. The simultaneous optimization of all Bragg peaks is characteristic for the IMPT calculation process.

¹⁵ Extracted from the ICRU Report No. 83 [53], page 25

2.11 Dose calculation algorithms [32], [57]

One of the central subjects in radiation oncology is the accurate and fast calculation of a 3D dose distribution within the patient. The result of the dose calculation has to be sufficiently accurate so that the context between the delivered dose and the clinical effects is reliable. Furthermore, the dose calculation needs to be fast so that the treatment planning process can be completed in clinically acceptable time. The subsequent competition between accuracy and calculation time is one of the major challenges for the development of modern dose calculation algorithms.

Once all required anatomical structures and the target volume are delineated, beam arrangements are designed and the dose distribution is optimized according to clinical objectives using computer based treatment planning software. For the optimization of a treatment plan, different treatment planning algorithms are available including different parameters such as beam weights and intensity modifiers.

This chapter covers different treatment planning algorithms: correction -, model -, pencil beam - and Monte Carlo - based algorithms. Every method can in principle be used for 3D treatment planning, although with a different degree of accuracy and speed. Heterogeneities pose the biggest challenge in predicting accurate dose distributions within a patient and are handled best by the model based on the Monte Carlo algorithm.

2.11.1 Correction based algorithms

Correction based algorithms are semi empirical algorithms that rely on measurement and correction factors in order to calculate the dose distribution within a patient. They are based on measured dose distributions in a water phantom whereas different correction factors are considered during the implementation in the treatment planning system. Typical corrections that have to be included are:

- Attenuation corrections for: contour irregularity, beam intensity modifiers such as wedge filters, compensators, etc. and tissue heterogeneities
- Scatter corrections
- Geometric corrections for: source to point of calculation field, size, shape and radial distance corrections

Correction based algorithms include different methods for interpolating measured depth-dose distributions or predicting the correction factors under given conditions. Usually the dose at any point is split into primary and scattered components, which are then computed separately and summed up to receive the total dose.

2.11.2 Model based algorithms

Model based algorithms rely less on measured data, they are rather based on the calculation of the dose distribution by means of physical models that simulate the radiation transport.

Model based algorithms are able to model the primary fluence of the photons emerging from a radiation source and the energy distribution resulting from primary photon interactions. Furthermore, model based algorithms are capable of simulating the transport of scattered electrons and photons and the absorption of the primary photons. The transport of energy created by secondary particles is accounted for by the introduction of the so called dose kernels. Dose kernels describe the energy transport and the deposition in water caused by a defined set of primary photon tissue interactions in different levels. Thus, a dose kernel is the complete summation of radiation energy imparted to the tissue from a point source of radiation fluence. For the application to inhomogeneous patient geometries these dose kernels are scaled in size according to the encountered local tissue densities.

A type of model based algorithm is the so called kernel based convolution-superposition method. The convolution-superposition method uses a convolution equation that includes the transportation of the primary- and the scattered photons and also takes electrons emerging from the primary photon interaction into account.

The dose $D(\vec{r})$ at the position of given point \vec{r} calculated from point kernels is expressed as:

$$D(\vec{r}) = \int \frac{\mu}{\rho} \psi_E(\vec{r}') * A(\vec{r} - \vec{r}') d^3\vec{r}' = \int T_E(\vec{r}') * A(\vec{r} - \vec{r}') d^3\vec{r}' \quad (2.16)$$

The factor $\frac{\mu}{\rho}$ is the so called mass attenuation coefficient. The values of different mass attenuation coefficients are dependent upon the absorption and scattering on the incident radiation caused by various mechanisms such as: coherent and incoherent scattering, photoelectric effect and pair production (chapter 2.2).

$\psi_E(\vec{r}')$ represents the primary photon (entrance) energy fluence and $A(\vec{r} - \vec{r}')$ the convolution kernel. The convolution kernel is a matrix of dose distribution generated by scattered electrons and photons originating at the primary photon interaction site. The most commonly used technique for the calculation of a kernel is the Monte Carlo method which simulates interactions of a large number of primary photons and ascertains the dose deposited in all directions by scattered particles set in motion at the primary photon interaction site.

The factor $T_E(\vec{r}')$ represents the so called Terma. It is the product of the mass attenuation coefficient $\frac{\mu}{\rho}$ and the primary photon energy fluence $\psi_E(\vec{r}')$. Terma corresponds the total energy per unit mass released by a radiation field interacting with a medium of density ρ at a certain point \vec{r}' . This locally released energy of the radiation field is afterwards available for another transport originating from the interaction point.

However, model based algorithms rely on approximations and therefore can only partly describe the physical processes involved in the microscopic absorption of the energy delivered by the radiation field.

2.11.3 Pencil beam algorithm [58] - [62]

Most treatment planning systems for particle beam therapy utilize so called pencil beam algorithms, which are semi-empiric and fulfill the requirements in terms of accuracy and speed. Pencil beam algorithms divide the main treatment beam into so called pencil beams that are infinitesimal segments of the main beam. Pencil beam algorithms use the superposition technique and they are based on different approximations as for example: the simplification of the treatment device by simple sources like point sources or parallel sources or the modeling of electron transport on straight lines.

When a dose calculation with the pencil beam algorithm is performed, the calculation is separated into two parts namely the depth-dose calculation along the central axis of the beam and an off-axis (lateral axis) term of the beam. The energy loss is modeled on the central axis and the scattering on the off-axis. First the calculation of the dose at a given point is generated by a pencil beam and then the individual pencil beams are summed up. Spots that are used during the calculation are defined via their initial energy, position, lateral spread and direction. The initial shape of one spot can be considered to be a Gaussian distribution at a given distance to the isocentre:

$$F(x, y, z) = \frac{1}{2\pi\sigma_{x_0}\sigma_{y_0}} \exp\left(-\frac{(x-x_0)^2}{2\sigma_{x_0}^2} - \frac{(y-y_0)^2}{2\sigma_{y_0}^2}\right) \quad (2.17)$$

$F(x, y, z)$ represents the relative fluence distribution of the spot located in the spot plane in the spot coordinate system (x, y, z) . Here, the coordinates (x_0, y_0, z_0) define the position within the spot plane, and $\sigma_{x_0} = \sigma(x_0, y_0, z_0, E_0)$ and $\sigma_{y_0} = \sigma(x_0, y_0, z_0, E_0)$ define the initial lateral spread, where E_0 is the initial energy of the spot.

The calculation of the total dose can be done by the integration over the beam aperture and the energy spectrum. Regarding the scanned pencil beam method, the primary beam can be seen as discrete pencil beams. Hence, the dose calculation reduces itself to a weighted sum:

$$D(x, y, z) = \sum D_{CAX,i}(x_0, y_0, z_0) * F_i(x-x_0, y-y_0, z-z_0) \quad (2.18)$$

Here, $D_{CAX,i}$ represents the dose that is delivered by a pencil beam at the central axis (CAX) at the coordinates (x_0, y_0, z_0) . F_i is the relative fluence distribution as mentioned above.

The main problem of the pencil beam algorithm is the limitation concerning heterogeneities. These heterogeneities can either be external originating from beam devices or internal heterogeneities in the patient's body such as air cavities, lung tissue, or bony structures close to the target volume. Heterogeneities pose a difficulty due to the fact that the PB algorithm uses only a one-dimensional density correction which does not accurately model the distribution of secondary electrons in heterogeneous media. Doses are scaled along a straight ray line originating from the radiation source to the calculation point and don't take effects of side and backscattered radiation into account. Hence, protons that partially go through air cavities are

not handled in a correct way. That means that treatment planning software based on Monte Carlo algorithm simulates the physical rules of interaction of radiation with matter in a more realistic way. The following chapter describes a parameter of the PB algorithm in more detail as this parameter was investigated in the course of this thesis.

Precision

An important source of errors in pencil beam based dose calculation is the influence of heterogeneities on the proton transport. These errors increase with growing difference between the voxel size and the spot size. To decrease the influence of the heterogeneities, the spot is divided into several sub-spots of finite size. The idea of dividing the spot has first been proposed by Schaffner et al. [63]. For a beam spot of precision n the number of sub-spots is given by:

$$N = (2 * n + 1)^2 \quad (2.19)$$

Sub-spots are weighted with the corresponding fluence of the original spot. Thus, a higher precision means a higher number of sub-spots and thus a better accuracy concerning heterogeneities as shown in Figure 2.17.

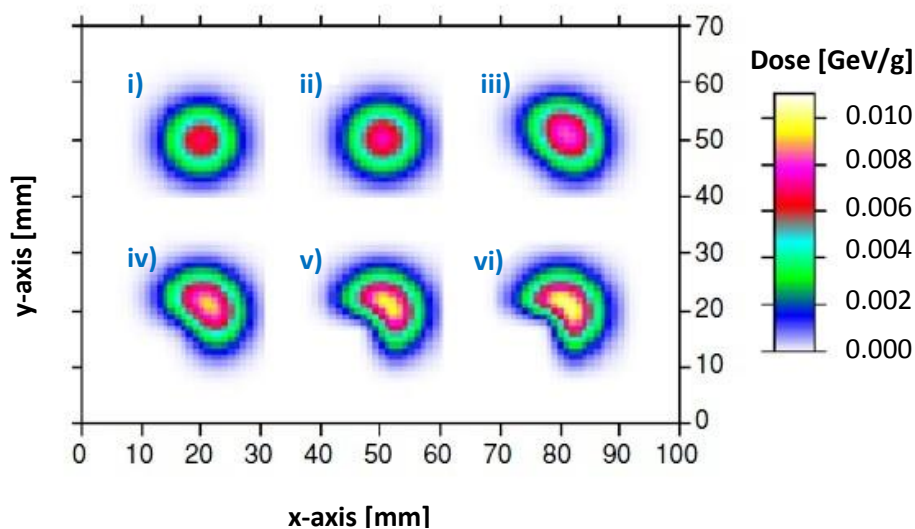


Figure 2.17: Influence of the number of sub-spots on the dose distribution at the surface of a water phantom if a blocking device is present (lower left). i) precision 0, ii) precision 1, iii) precision 2, iv) precision 3, v) precision 4 and vi) precision 5.¹⁶

¹⁶ Extracted from M. Soukup, M. Fippel, and M. Alber [58], page 5

2.11.4 Monte Carlo algorithm [64] - [67]

Treatment planning algorithms that are based on the Monte Carlo Method achieve the most accurate results for dose calculation especially when heterogeneities have to be considered with the drawback of more processing time.

The MC method is a computational method that uses known probabilities together with random numbers to predict results of interactions. It can simulate the transport of millions of particles through matter employing statistical methods. The Monte Carlo algorithm is able to simulate the probable direction and energy distributions of every single particle. Hence, MC uses the “Law of Large Numbers”, which says that the average of the results obtained from a large number of trials should be close to the expected value, and will tend to get closer as more trials are performed. Therefore, the higher the number of simulated particles (histories) is, the higher is the statistical accuracy. That means, if only a few protons were needed to deliver the desired dose to the patient, the MC method would not be accurate. By modeling the basic particle interactions directly, the MC method is not limited to certain geometries or treatment setups.

In principle the MC algorithm allows the individual consideration of each and every photon or particle. For the accurate calculation, the path of each particle through matter can be divided into several small steps. For each step the interaction probabilities are calculated. While the particle passes through matter, different particle interactions take place, as for example energy- and direction- change of the particle, ionization, or dose deposition in the target material. Upon calculating the interaction and the subsequent effects, the length of the next step is ascertained. This procedure is repeated until the energy of the particle either reaches zero or a predefined energy cut off value has been attained. Secondary particles created from the initial particles are treated in the same way. The calculation of many particle tracks yields to an increasing realistic description of the global effects of particle interactions such as dose deposition.

Unlike analytical dose calculations, MC simulations take the specific properties of each material, such as its atomic composition or electron density into account. Further, MC dose calculations can distinguish between electromagnetic and nuclear interactions.

In combination with IMRT and inverse planning (chapter 2.10.3) MC represents a real clinical benefit, in means of accuracy but there are some drawbacks that need to be taken into account when Monte Carlo is used for dose calculation instead of analytical techniques. Monte Carlo methods require large amounts of random numbers, whereby a drawback can arise from the random number generator [68]. Therefore, a proper random number generator has to be chosen. It should be considered to use multiple number generators and for each generator multiple initial states (also called seed). The main problem is that the final dose distribution can change if the seed of the random number generator is changed. Therefore, different reasonable dose outcomes can be achieved. Another problem that has to be addressed comes from the statistical noise [69]. The statistical uncertainty of the dose in every voxel causes a systematic uncertainty of the outcome. However, this systematic aberration can be calculated and considered during the optimization progress.

Another matter that needs to be considered when using the Monte Carlo algorithm are voxels consisting of air. The dose of the air voxels is calculated correctly when the Monte Carlo algorithm is used and the air voxels receive a significant smaller dose than the surrounding tissue. Now if the air voxels are part of the target volume, the optimization algorithm needs to compensate for the underdosage of the air voxels which can cause problems in the optimization process.

The following subsections describe some parameters of the MC algorithm in more detail as these parameters were investigated in the framework of this thesis.

Mean relative statistical uncertainty (MCuncertainty)

Due to the fact that the MC algorithm is based on various statistical effects, the mean relative statistical uncertainty per spot depends strongly on the number of particles that are simulated. The relative statistical uncertainty per spot s can be directly attributed to the number of particles traversing a given point and is calculated according to the following formula:

$$s^2 = \frac{1}{N^2} \left[N \sum_{i=1}^N d_i^2 - \left(\sum_{i=1}^N d_i \right)^2 \right] \quad (2.20)$$

N represents the total number of particles and d_i describes the individual energy deposited of particle number i . A total uncertainty of a MC simulation can therefore not be given, as the number of particles interacting with a given voxel isn't constant and varies widely depending on the position in relation to the beam.

Mean relative statistical uncertainty threshold (MCerrordosethreshold)

The mean relative statistical uncertainty threshold value z describes which voxels are included in the uncertainty considerations. Only voxels that receive a dose of $z \times \text{maximum dose per spot}$ are considered in the uncertainty calculation.

Maximum number of particles (MCmaxnrparticles)

The maximum number of particles specifies how many particles are taken into account for the dose calculation. Within the scope of this thesis, a rough estimation of the value was made, to assure that the maximum number of particles doesn't work as a stop criterion (chapter 4.1.1).

2.12 Optimization process [70] - [73]

A necessary part of any treatment planning procedure is the treatment optimization. The aim of the optimization process is to achieve good dose conformity to the PTV and to avoid a high dose exposure to the OAR. Treatment optimization is based on physical or biological dose objectives or constraints such as the maximization of the dose homogeneity within a tumor.

Usually, global thresholds for the tolerable minimum (D_{min}) and maximum doses (D_{max}) for the PTV or the CTV are set for the entire target volumes. The doses D_{min} and D_{max} are chosen in such a way that the resulting dose window allows for some flexibility if conflicting goals of organs at risk have to be fulfilled simultaneously. The use of D_{min} and D_{max} should lead to sufficient dose homogeneity and should be kept within the ICRU prescriptions. For organs at risk, not only global constraints for the entire organ should be considered, but also dose volume constraints. These constraints allow specifying a certain percentage of a volume which should only receive the maximum of a selected dose.

In IMPT (chapter 2.10.3), the optimization process is carried out in order to determine the proton beam spot intensities that best fulfill the clinical requirements. For photon IMRT plan optimization the fluence profiles for all beams serve as the only free treatment parameters. Other parameters, like the number of beams, the beam entry angles, the beam energy or the radiation type are preselected by the treatment planner and remain fixed during the whole optimization process. Furthermore, the concept of equivalent uniform dose (EUD) was designed to describe non-uniform dose distributions in organs. The EUD concept is used for organs and structures which can be seriously damaged by a high dose occurring in a small area.

The so called objective function considers dose constraints and weights the importance of the target and the organ at risk prescriptions in order to achieve the optimal intensity pattern. The optimization of the treatment plan corresponds mathematically speaking to a search for the minimum or maximum value of the objective function. This is achieved with the help of the optimization algorithm that calculates an optimized treatment plan. Basically, the optimization process follows the steps that are shown in Figure 2.18.

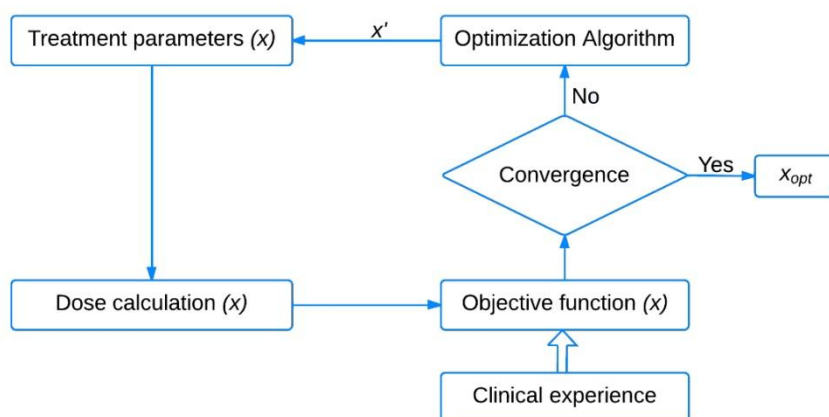


Figure 2.18: Optimization loop for iterative IMRT optimization.¹⁷

¹⁷ Extracted from Oelfke et al. [73], page 33

To start the optimization progress, a set of variable treatment parameters x - whose values have to be adjusted to their optimal setting x_{opt} - is chosen. An initial 3D dose distribution is calculated for the not yet optimized values of x . In the next step, the objective function reduces the calculated 3D dose distribution to a single number. If the quality of the treatment plan is considered to be sufficient, the current value x is chosen as the optimum x_{opt} otherwise the optimization algorithm calculates an updated set of x -values x' and a new iteration of the optimization is initiated. The term optimization does not necessarily indicate that the method will find the best (“optimal”) dose distribution.

2.13 Evaluation parameters

The following evaluation parameters are essential tools to evaluate radiotherapy treatment plans. In the course of this thesis all evaluation parameters were used as basis for the interpretation of the results obtained when comparing MC dose calculation with PB dose calculation.

2.13.1 Isodose distributions

Isodose distributions are points or zones in the body or the phantom that receive equal dose levels. They are a planar representation, depicted on every single CT slice, of the dose distribution and show the dose delivered by one beam or the combination of several beams. Dose distributions of competing plans are evaluated by viewing isodose distributions in individual slices. Displaying the dose distribution in the form of isodose curves or surfaces is not only useful because it shows regions of uniform dose, high dose, or low dose but also their anatomic location and extent. While isodose distributions can display the actual dose in Gray, it is also common to present them normalized to 100% at a fixed point, so that isodose distributions represent lines of equal dose as a percentage of the prescribed dose. Isodose distributions offer an important and essential evaluation tool with respect to treatment plan quality.

2.13.2 Dose-volume histogram (DVH)

The dose-volume histogram (DVH) provides quantitative information about the amount of volume of a certain region of interest (target or OAR) that receives a certain amount of dose. Thus, a DVH is a useful and routinely used tool for quantitative evaluation and comparison of calculated treatment plans. Since this evaluation method reduces the dose distribution to a two dimensional representation without any spatial information, it should be used with care and always combined with a consideration of the isodose distributions. In the illustration of a DVH the bin doses are represented along the horizontal axis and the structure volumes (either

percent or absolute volumes) on the vertical axis. Basically two types of DVHs can be distinguished: cumulative DVHs or differential DVHs (Figure 2.19). The cumulative DVH sums up all dose bins to certain volume bin. In contrast, the differential DVH shows the volume of a structure receiving a dose given by the bin.

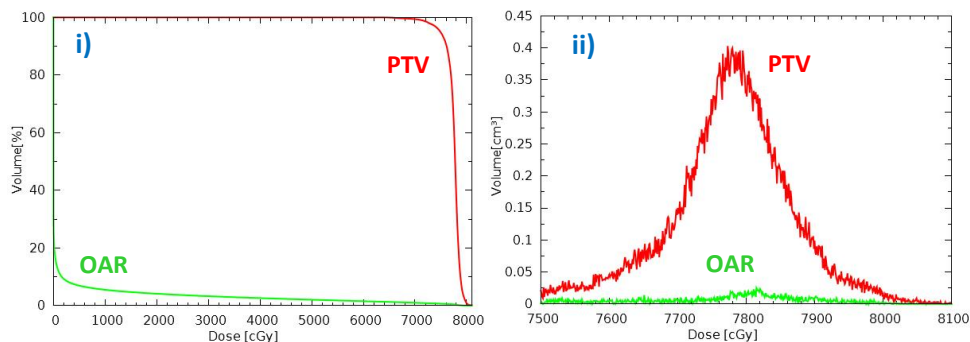


Figure 2.19: Example of a i) cumulative DVH and a ii) differential DVH.

2.13.3 Dose-volume-specifications

The dose-volume-specifications can be used for the evaluation of the quality of a treatment plan. They represent the deposited dose D_V [Gy] at a certain percentage of a volume V .

In the course of this thesis the following dose-volume-parameters, recommended by the ICRU83 [53] were used for the evaluations of the target volume:

- The Dose [Gy] at 2% of the volume ($D_{2\%}$) as a surrogate for the maximum dose
- The Dose [Gy] at 50% of the volume ($D_{50\%}$) as a surrogate for the median dose
- The Dose [Gy] at 98% of volume ($D_{98\%}$) as a surrogate for the minimum dose

For example, $D_{98\%}$ is the dose that covers 98% of the volume of the PTV. The median dose, $D_{50\%}$ has to fulfill the dose prescriptions.

Another type of the dose-volume-specifications represents a certain amount of volume [%] that is exposed to a certain percentage of the prescribed dose. For the evaluation of the treatment plans the parameters at 95% of the prescribed dose ($V_{95\%}$) was used to evaluate the dose coverage. As a guideline, the ICRU83 report states that the different dose-volume-specifications should follow these constraints:

- $D_{2\%} \leq 107\%$ of the prescribed dose
- $D_{98\%} \geq 90\%$ of the prescribed dose
- $V_{95\%} \geq 95\%$ of the prescribed dose

2.13.4 Homogeneity index (HI) [74]

The homogeneity index analyzes the uniformity of a dose distribution within the target volume. The HI is defined by ICRU83 [53] as followed:

$$HI = \frac{D_{2\%} - D_{98\%}}{D_{50\%}} \quad (2.21)$$

The closer the HI is to zero the more homogeneous is the dose distribution within the target volume.

2.13.5 Conformity index (CI) [75]

The conformity index gives the relationship between irradiated tumor tissue and nonirradiated healthy tissues and it is a valuable tool when an objective comparison between two treatment plans is required. The CI defined by Paddick et al. [76] measures to what extent the dose distribution conforms to the shape and size of the target volume.

$$CI = \frac{TVPI^2}{PI * TV} \quad (2.22)$$

TVPI represents the PTV subvolume covered by the 95% prescription isodose, *PI* represents the volume encompassed by the 95% prescription isodose and *TV* represents the total PTV. Hence, an ideally conformal treatment plan has a CI value of 1.

2.13.6 Dose-difference maps

As the name indicates, a dose-difference map is a graphical representation that shows the calculated difference between the dose distributions of one plan subtracted voxel by voxel from the dose distribution of another plan.

2.13.7 Gamma index method [77] - [80]

Dose-difference displays have one disadvantage: they don't have a numerical index that offers comparison of dose calculation quality. However, the Gamma index evaluation is a technique that enables quantitative analysis for different dose distributions. For the comparison of two different dose distributions the γ -evaluation combines a dose-difference criterion and a distance-to-agreement criterion (DTA), also called acceptance criteria.

A measured dose distribution $D_m(\vec{r}_m)$ at a given grid point \vec{r}_m is compared to a reference dose distribution $D_r(\vec{r}_r)$ at a given grid point \vec{r}_r . The dose-difference formula is defined as followed:

$$\delta(\vec{r}_m, \vec{r}_r) = D_r(\vec{r}_r) - D_m(\vec{r}_m) \quad (2.23)$$

The spatial distance is stated below:

$$r(\vec{r}_m, \vec{r}_r) = | \vec{r}_r - \vec{r}_m | \quad (2.24)$$

The general form of the $\Gamma(\vec{r}_m, \vec{r}_r)$ function, as it was used in the algorithm to calculate the 3D gamma metric of the CERR software (chapter 3.2.3), is:

$$\Gamma(\vec{r}_m, \vec{r}_r) = \sqrt{\frac{\delta^2(\vec{r}_m, \vec{r}_r)}{\Delta D^2} + \frac{r^2(\vec{r}_m, \vec{r}_r)}{\Delta d^2}} \quad (2.25)$$

ΔD represents the acceptance criterion and Δd describes the distance-to-agreement criterion.

Following formula (2.25) the evaluated point with the smallest $\Gamma(\vec{r}_m, \vec{r}_r)$ value conforms best to the reference point and is therefore called the γ -index of that particular reference point. The γ -index is defined as followed:

$$\gamma(\vec{r}_m) = \min\{\Gamma(\vec{r}_m, \vec{r}_r)\} \quad \forall \{\vec{r}_r\} \quad (2.26)$$

If $\gamma(\vec{r}_m) \leq 1$ the evaluated distribution is accepted at this particular point, otherwise the comparison revealed an unacceptable difference. Due to the fact that the γ -index for each reference point is defined independently of the other point of the reference dose distribution, the γ -index tool can be employed for 1D, 2D and 3D dose distributions. There is no consensus what gamma evaluation parameters for an IMRT plan verification should be used. However, a commonly used clinically gamma evaluation criteria set is $\Delta D = 3\%$ deviation in dose, and $\Delta d = 3 \text{ mm}$ dose to agreement, also written as $3\%/3\text{mm}$. As acceptance criterion ΔD for the dose difference, either a local criterion or a global criterion can be used. Furthermore, a threshold for low doses can be considered. A 5% threshold is used for photon dose calculation in clinical routine. This threshold serves as noise suppression and ensures that all values smaller than 5% of the maximum are rejected.

The gamma function applied to each point in the dose distribution can be used to create a γ -index map which is a distribution of accuracy corresponding to the dose distributions. Furthermore a cumulative or differential γ -area histogram can be calculated for a region of interest. Similar to DVHs (chapter 2.13.2) a γ -area histogram displays the volume that exceeds a specified γ -index value. According to the paper published by Stock et al. [78], there are some constraints that can be considered:

	$\gamma_{1\%}$	γ_{mean}	$\gamma > 1$	Appraisal and approach
Range	0-1.5	0-0.5	0-5%	Accepted
	1.5-2	0.5-0.6	5-10%	Acceptable, other verification tools such as dose-difference maps and dose profiles are needed for further evaluation
	>2	>0.6	>10%	Not acceptable – measurement has to be repeated or plan has to be re-optimized

Table 2.2: Constraints for γ -index-volume specifications.¹⁸

¹⁸ Extracted from Stock et al. [78], page 409

3. Material and methods

3.1 Phantom geometries

This chapter gives an overview of the phantoms that were created and used in the framework of this thesis.

3.1.1 Phantom 1 “Testphantom”

To evaluate the optimal configuration of the MC calculation settings like “MCerror dosethreshold”, “MCuncertainty” and the “Maximum number of particles” (chapter 2.11.4) a phantom with different densities was created based on the publication by Soukup et al. [58] (Figure 3.1). Therefore, an existing empty CT of a waterphantom was overwritten using MATLAB. The dimensions of the structures with different densities (air, water and bone) were assigned and individual slices with 4 mm spacing were generated. The new CTs with the different densities were exported to the treatment planning system Oncentra MasterPlan (OMP) and each contour was delineated manually.



Figure 3.1: Phantom used by Soukup et al.¹⁹

The Hounsfield units and the dimensions of the respective structures are given in Table 3.1. Figure 3.2 shows the resulting phantom that includes the properties of both settings used by Soukup et al. shown in Figure 3.1.

Name Contour	Dimensions [mm]			Hounsfield units
Outline	x: 300	y: 300	z: 300	0
Bone	x: 100	y: 49	z: 96	1000
Air	x: 100	y: 51	z: 96	-1000
Target 1, 2, 3	x: 40	y: 40	z: 36	0
Cubic AB	x: 60	y: 60	z: 36	-1000; 1000
Cylinder Bone	Radius: 20		Height: 96	1000
Cylinder Air	Radius: 20		Height: 96	-1000

Table 3.1: Dimensions and radiodensities of the structures of the Testphantom

¹⁹ Extracted from M. Soukup, M. Fippel, and M. Alber [58] page 14 and 15

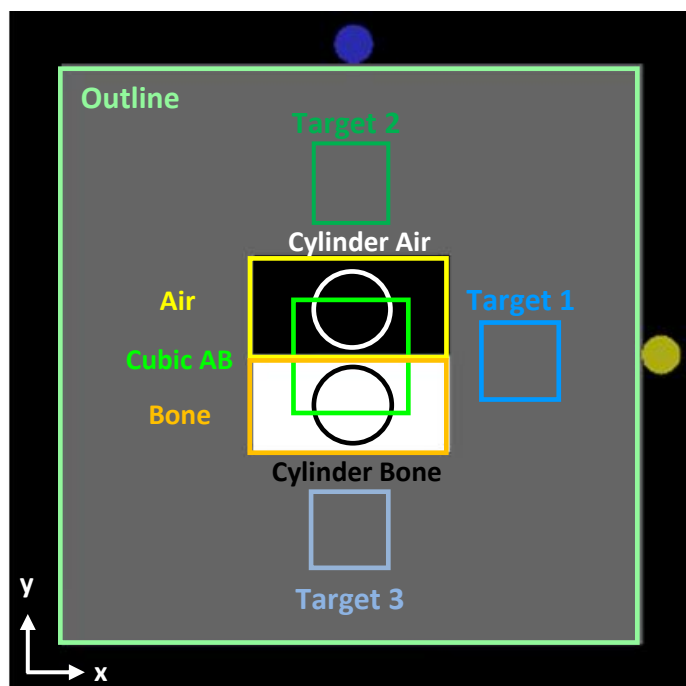


Figure 3.2: Phantom setup for the evaluation of the MC parameters.

In order to achieve a symmetrical setting the bone and air structure was placed exactly in the center of the phantom. The virtual target structures within the phantom were arranged in a manner that the beam passes the structures with different densities in different ways. The beam could pass through the center of the phantom, i.e. along the border between the lung and bone or first through air and then bone or vice versa. The bone and the air structure created a boundary layer where the differences between MC and PB algorithms should be particularly visible. All targets were located 15 mm proximal to the surface of the air/bone structure.

However, after a few investigations were carried out it became obvious that the phantom wasn't constructed difficult enough for testing the treatment planning algorithms in a proper way. Only a slight difference was observed between the treatment plans based on MC and PB algorithms and nearly none between the different MC parameters. Furthermore, it was visible that the XiO software had problems calculating the dose distribution in air, as no dose was deposited there. Thus, a new phantom with a more sophisticated geometry and lung tissue instead of air was created.

3.1.2 Phantom 2 “Chessphantom”

The second phantom created was more complex and contained a chess pattern structure representing density heterogeneities to explore the difference between the MC and PB algorithm in the presence of complex inhomogeneities (Figure 3.3). It was based on the publication by Sawakuchi et al. [83]. The dimension of the outer contour was 240 mm, while individual slices were generated using a 4 mm spacing. The chess pattern structure consisted of alternating cuboids with the densities of lung and bone tissue. The phantom contained four different structures serving as target structures. The first target called “Chess Target” was located on the bottom of the chess pattern and the other three called “Target 1-3” behind the chess pattern. Target 1 was 10 mm away from the edge of the chess pattern structure, Target 2 20 mm and Target 3 30 mm. The Hounsfield units and the dimensions of the respective structures are given in Table 3.2 and a schematic drawing of the phantom is shown in Figure 3.3.

Name Contour	Dimension [mm]			Hounsfield units
Outline	x: 240	y: 240	z: 136	0
Chess pattern	x: 100	y: 200	z: 96	1000, -800
Chess Target	x: 40	y: 40	z: 40	1000, -800
Target 1, 2, 3	x: 40	y: 40	z: 40	0

Table 3.2: Dimensions and radiodensities according to Schneider [85] of the structures of the Chessphantom.

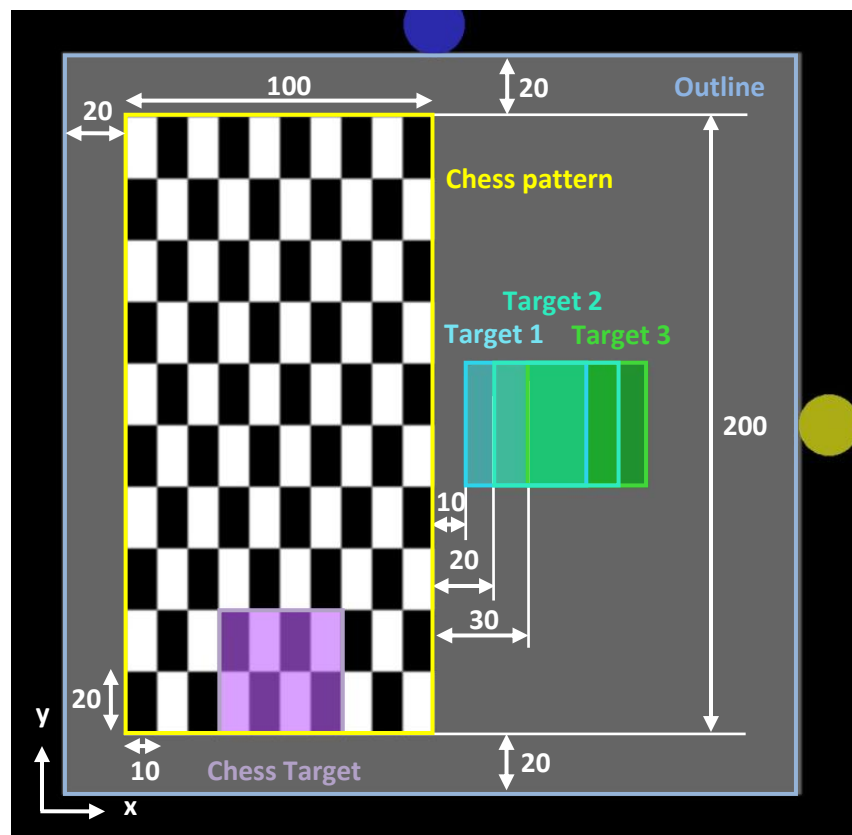


Figure 3.3: Phantom setup for the evaluation of the MC parameters. All dimensions are given in millimeters [mm].

3.1.3 Phantom 3 “Waterphantom”

For the evaluation of the user interface parameter a homogeneous phantom with three cubic targets of different sizes was created according to the paper by Hillbrand et al. [61]. As for the other two phantoms an existing CT of a waterphantom was overwritten using a MATLAB code and the dimensions were manually entered. The dimension of the outer contour was 200 mm, while individual slices were generated with 5 mm spacing in between. Three cubes of different sizes (8 cm³, 64 cm³ and 512 cm³) were created as target structure. The target cubes were located concentrically in the middle of the outer structure to achieve a symmetrical setup. The Hounsfield units and the dimensions of the structures are given in Table 3.3 and Figure 3.4 shows a schematic drawing of the phantom.

Name Contour	Dimension [mm]			Hounsfield units
Outline	x: 200	y: 200	z: 300	0
Small target	x: 20	y: 20	z: 20	0
Midsized target	x: 40	y: 40	z: 40	0
Large target	x: 80	y: 80	z: 80	0

Table 3.3: Dimensions and radiodensities of the structures of the Waterphantom.

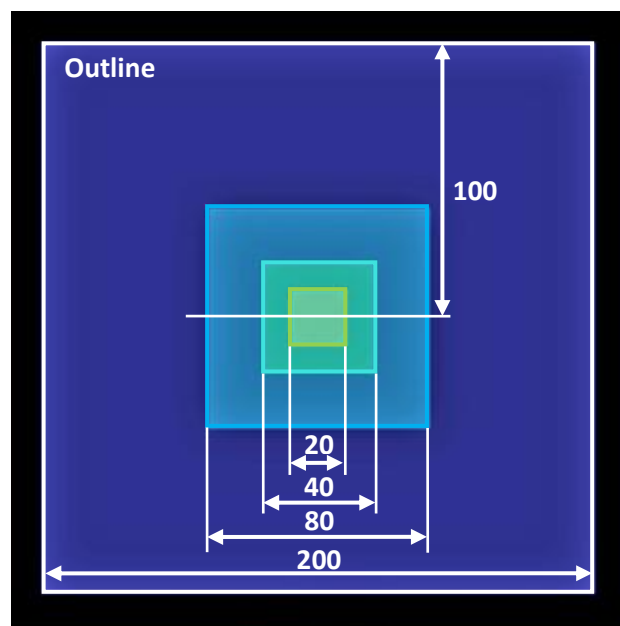


Figure 3.4: Phantom setup for the evaluation of the user interface parameters. All dimensions are given in millimeters [mm].

3.2 Hardware, Treatment planning system and software

This chapter gives a short overview of the treatment planning Hardware, the treatment planning system XiO and the software CERR that were used in the frame of this thesis.

3.2.1 Treatment planning Hardware

The treatment planning hardware was a Hewlett-Packard Z820 workstation equipped with two Intel® Xeon® E5-2670 2.6 GHz (8 core) CPUs and 32 GB DDR3 RAM.

3.2.2 XiO

The treatment planning software XiO research version v4.62 (Elekta AB, Stockholm, Sweden) was used for spot scanning dose calculation and optimization using different algorithms and phantom geometries. The XiO software includes pencil beam algorithms for active scanning [58] and for passive scattering [59]. The Monte Carlo Dose calculation is based on the paper "A Monte Carlo dose calculation algorithm for proton therapy" by Fippel et al. [65]. The MC dose calculation algorithm is not yet available in the commercial XiO treatment planning software and the MC algorithm parameters have to be changed in a text based configuration file, as described in chapter 3.3.2.

3.2.3 CERR [81]

CERR (Version 4.6, May 2014) is a MATLAB-based **C**omputational **E**nvironment for **R**adiation **R**esearch. CERR can import and display treatment plans from a wide variety of commercial or academic treatment planning systems, if the data is available in the DICOM or RTOG format. After the DICOM files are exported from XiO and imported to the CERR environment, they are converted to a MATLAB-readable CERR file and can be displayed using graphical user interface. CERR is able to recompute DVHs of every target volume and organ at risk. An important feature of CERR is the summation or subtraction of the doses of different treatment plans. In the course of this thesis, this was used to perform a dose difference analysis (chapter 2.13.6). This subtraction was done on a voxel by voxel basis. Furthermore, a γ -index analysis could be performed with CERR as mentioned in chapter 2.13.7. With CERR the γ -index-volume specifications can be calculated as well.

3D gamma metric in CERR [81]

The 3D Gamma metric that is employed in the CERR software is based on "A fast algorithm for gamma evaluation in 3D" [82], which has been implemented in MATLAB.

As mentioned in chapter 2.13.7, the criterion ΔD for the dose difference can either be a local criterion or a global criterion. The CERR software uses a global criterion, thus, the percentage of the maximum dose of the base dose.

3.3 Experimental Setup

The treatment planning software XiO (chapter 3.2.2) was used for spot scanning dose calculation and optimization using the different phantoms as described in the previous chapter. The treatment plans generated with the XiO system were processed with the CERR (chapter 3.2.3) software. The resulting treatment plans were compared in terms of dose profiles perpendicular to and parallel to the central beam axis and furthermore by dose homogeneity, conformity measures, dose-volume-specifications, dose-difference maps and γ -index evaluation (chapter 2.13). Furthermore, the time that was necessary to calculate the dose distribution was investigated. It should be considered that the time for dose calculation in an inverse treatment planning approach is strongly dependent on the available hardware (chapter 3.2.1).

3.3.1 Planning

Using the XiO software, the number of spots is e.g. determined by the distance of the spot layers and geometrical parameters defining the lateral space between individual Bragg peaks. The degrees of freedom and thus the ability to create individual dose distributions for different patients correspond directly with the number of spots developed from the optimization progress [61]. Using the inverse planning approach the number of protons associated with each pencil beam (weighting) is adjusted to find an optimal solution for the prescribed dose for the target volume and to spare healthy tissue.

For all targets located in the different phantoms (chapter 3.1), the proton dose was delivered by one single beam and calculated using different algorithms and configurations. The proton beam data for testing the MC algorithm provided by Elekta had the default setting of a spot spacing of 3 mm. For this thesis, a fixed nominal lateral spot size (spot sigma) of 3 mm was assumed. Spot sizes around 3 mm have been reported for high proton energies. For lower energies the spot sizes are typically between 5 and 7 mm [61]. Furthermore, the alignment shift that adds or subtracts an extra margin to the distal edge of the target was held constant at 0.5 cm. If a beam's Bragg peak is outside the target volume by more than 1 cm, that beam is automatically discarded during the optimization progress [84].

After evaluating the first data, it became apparent that an air gap of 10 cm needed to be set. This was due to the fact, that the trial version of the implemented MC algorithm had difficulties calculating the dose without an additional air gap, as no dose was calculated in the entry region of the beam. An air gap can be set in order to consider the gantry geometries and to avoid collisions with the gantry and the patient. As no actual treatment was performed with the simulated treatment plans the air gap was first set to 0 cm, but changed after the evaluation of some treatment plans.

3.3.2 Parameter input

The calculation model used by XiO could be changed in the text based configuration file *pb_calc_type* that was located in the */tmp/beammodel* folder. Therefore the number in the text file needed to be changed before starting the dose distribution calculation.

- 1) Pencil Beam CPU based
- 2) Pencil Beam GPU based
- 3) Monte Carlo CPU based

All MC parameters were changed in the *pb_calc_param* text file which was also located in the */tmp/beammodel* folder (Figure 3.5). All machines implemented in the XiO software can access these parameters, but only the Monte Carlo based machine *ATRePdemon03* can process the MC parameters properly.

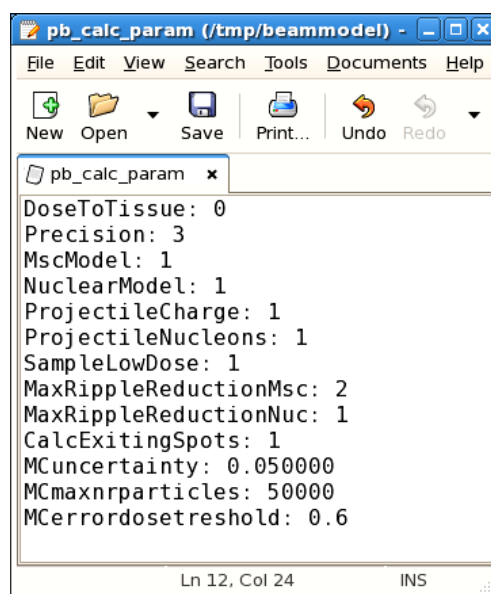


Figure 3.5: Text file *pb_calc_param* to change the MC parameters

The important parameters that need to be considered are explained in detail in chapter 2.11.3 and chapter 2.11.4. The precision n can range from $n = 0, 1, 2, 3, 4, 5$. By default this value is set to $n = 3$, which means a total number of 49 sub-spots, according to formula (2.19). In the following chapters the precision is abbreviated with "prec". The MCuncertainty is by default set to 0.05, which means a mean relative statistical uncertainty of 5% in each voxel. The MCuncertainty is hereinafter referred to by the abbreviation "unc". The MCmaxnrparticles is by default set to 50,000 which means that 50,000 particles are considered in the dose calculation. The MCerrordosethreshold – abbreviated with "err" in the following chapters - is by default set to 0.6 which means that only voxels that receive a dose of 60% of the maximum dose per spot are considered in the uncertainty calculation while all statistical uncertainty values are allowed for low energy spots.

These parameters were changed and respective results were investigated in detail.

3.3.3 Evaluation of the MC parameters

For the assessment of the Monte Carlo parameters the Chessphantom described in chapter 3.1.2 was used. During the evaluation of the MC parameters, the spacing between the IMPT range-(energy-) layers was fixed at 0.8 (peak width multiplier). The distance between the centers of the spots (spot spacing) was 0.5 cm. All these user interface parameters were chosen according to a previous investigation [61].

Furthermore, the grid size of the dose calculation matrix (distance between calculation points) was set to $2 \times 2 \times 2 \text{ mm}^3$. As the distance between calculation points is decreasing, the resolution of the calculation grid and thus the calculation precision is increasing. Hence, the time required for the dose calculation increases as well. To achieve the prescription of 10 Gy to the target, the maximum dose was set to 1050 cGy and the minimum dose on 950 cGy. Furthermore a dose goal of 1000 cGy was set. For the target "Chess Target" located in the chess pattern structure, the gantry angle was set to 0° and 15° . For the targets "Target 1,2,3" located behind the chess pattern structure the gantry angle was set to 270° . This is shown in Figure 3.6.

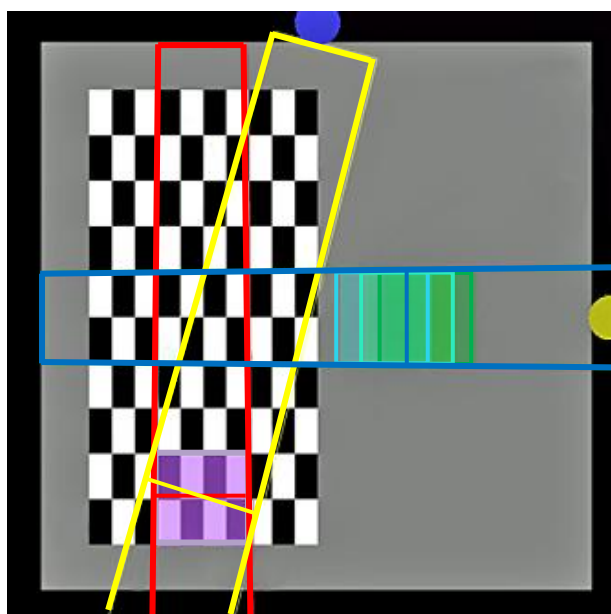


Figure 3.6: Beam setup used for the assessment of the MC parameters.

To start the evaluation of the MC parameters a treatment plan was created with the above listed user interface parameters using the PB algorithm. This plan was then calculated and optimized. Thereby, the maximum number of iteration was appointed to 300 and the optimization convergence criterion was set to 0.001%. In a next step the MC algorithm was chosen in the *pb_calc_type* file and the MC parameters (MCuncertainty, MCmaxnrparticles and MCerror dosethreshold) were changed in the *pb_calc_param* text file (chapter 3.3.2). The dose of the optimized PB plan was recalculated using the MC algorithm with the corresponding MC parameters. After saving the recalculated treatment plan, the resulting MC dose distribution was optimized as well.

3.3.4 Evaluation of the user interface parameters

For the evaluation of the user interface parameters (peak width multiplier and spot spacing) the Waterphantom described in chapter 3.1.3 was used. The assumptions of a fixed spot size, a single beam and a homogeneous geometric phantom were made for the purpose of avoiding influences from other factors on the characteristics of the dose distribution.

To start the evaluation of the user interface parameters a treatment plan was created. The grid size of the dose calculation matrix was set to $3 \times 3 \times 3 \text{ mm}^3$. To achieve the prescription of 10 Gy to the target, the maximum dose was set to 1005 cGy and the minimum dose on 995 cGy. Furthermore a dose goal of 1000 cGy was defined. For the assessment of the user interface parameters the gantry angle was set to 0° .

For the evaluation of the peak width multiplier (PWM) a fixed spot spacing of 0.5 cm was set and the PWM was varied from 0.4 to 1.8 in steps of 0.1 for all three targets. For plan calculation and optimization the maximum number of iterations was set to 300 and the optimization convergence criterion was set to 0.001%. Each plan was optimized and then compared with various evaluation tools as described in chapter 2.13. After a suitable PWM was found, the spot spacing values were varied as well to find acceptable user interface parameters. The spot spacing was varied between 0.3 cm and 0.6 cm in 0.1 cm steps, according to a spot spacing of less than two times the spot sigma (0.3 cm) [61].

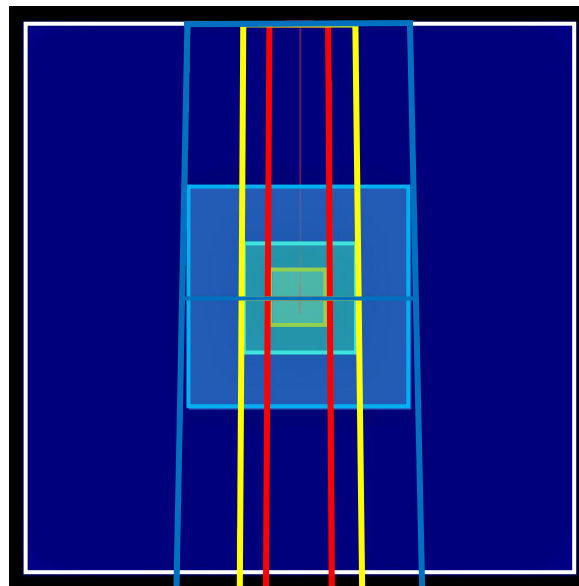


Figure 3.7: Beam setup used for the assessment of the user interface parameters.

4. Results

This chapter gives an overview of the results that were obtained within the scope of this thesis. Treatment planning was performed according to chapter 3.3.1 and the different phantoms described in chapter 3.1 were used in order to evaluate the MC (chapter 3.3.3) and user interface parameters (chapter 3.3.4), respectively.

4.1 Assessment of the MC parameters

4.1.1 Stop criterion maximum number of particles

The MCmaxnrparticles function specifies how many particles are taken into account for the dose calculation, as mentioned in chapter 2.11.4. The aim of this experimental setup was to make an estimation of the termination criterion of the number of particles. This was done in order to prevent the maximum number of particles as a limiting factor for future dose calculations. Table 4.1 shows the dose calculation times and the homogeneity index (HI) and conformity index (CI) values for various MCuncertainty, MCerrordosethreshold and maximum number of particles combinations. Due to the long calculation time, the homogenous Waterphantom (chapter 3.1.3) was used and the small target with the dimensions of 20x20x20 mm³ served as target structure for this setup (Figure 3.4). A grid size of 3x3x3 mm³ was chosen and the user interface parameters were set to a PWM of 0.8 and a spot spacing of 0.5 cm.

MCuncertainty	MCerrordose-threshold	MCmaxnrparticles	D.C.T. [s]	HI	CI
0.05	0.6	5,000	26	0.044	0.725
		50,000	30	0.041	0.727
		500,000	30	0.040	0.730
0.05	0.1	5,000	20	0.047	0.722
		50,000	34	0.039	0.724
		500,000	34	0.037	0.723
0.04	0.1	50,000	59	0.036	0.719
		200,000	59	0.035	0.725
		500,000	59	0.035	0.723
0.03	0.1	50,000	94	0.033	0.718
		200,000	95	0.032	0.717
		500,000	95	0.032	0.718
0.02	0.1	50,000	94	0.034	0.711
		200,000	199	0.032	0.717
		500,000	199	0.032	0.717
0.01	0.1	200,000	350	0.033	0.710
		500,000	764	0.032	0.719
		5,000,000	766	0.031	0.719

Table 4.1: Dose calculation times (D.C.T.), HI and CI for different MCuncertainty and MCerrordosethreshold values and maximum numbers of particles.

As shown in Table 4.1 the maximum number of particles was varied and consequently the dose calculation time was shorter in case the number of particles worked as a stop criterion and terminated the dose calculation. To determine the impact of the maximum number of particles on the target homogeneity and dose conformity, calculation of the HI and CI was carried out. As lower HI and higher CI values correspond to a more homogeneous and conformal treatment plan, deterioration for both the HI and the CI could be observed when the maximum number of particles terminated the dose calculation. For the parameter setting of a MCuncertainty (unc) of 0.02 and a MCerrordosethreshold (err) of 0.1, a maximum number of particles of 50,000 terminated the dose calculation. When using 50,000 particles, the HI was 0.034 and the CI was 0.711, whereas the HI was 0.032 and the CI was 0.717 when using 200,000 particles. Starting with a value of unc=0.02 and err=0.1, a particle number of 50,000 didn't suffice. Thus, to assure that the number of particles wasn't a limiting factor for future dose calculations, 50,000 particles were required for unc values between 0.05 and 0.03 and 500,000 below 0.03. In the end a maximum number of particles of 500,000 was chosen for all MCuncertainty values. In general, approximately 10^{10} particles are used in clinical treatment planning. This value is independent of the maximal number of particles considered in a MC dose calculation due to the fact that the MC dose calculation is a statistical process and therefore, such a high number of particles isn't necessary to achieve sufficient accuracy.

4.1.2 Evaluation of the Chess Target

After performing an estimation of the maximum number of particles, the dose distribution calculated for the first target was examined. Therefore, the cubic target "Chess Target" ($20 \times 20 \times 20 \text{ mm}^3$) located within the chess pattern structure of the Chessphantom (chapter 3.1.2) served as target structure. The maximum number of particles that the MC algorithm considers was set to 500,000, according to chapter 4.1.1.

For estimation, what MC parameters might be interesting, the gantry angle was set to 0° and the MCuncertainty was varied from 0.05 to 0.01 in steps of 0.01 and the MCerrordosethreshold was changed from 0.6 to 0.1. For a gantry angle of 15° , the modification of the MC parameters was reduced and only dose calculation using selected parameters was carried out due to the long dose computation time. The results of this investigation are shown in Table 4.2.

For the assessment of the MC parameters, treatment plans were generated using two different approaches, as mentioned in chapter 3.3.3:

1. The dose distribution was calculated using the PB algorithm and then optimized. Afterwards, the dose distribution of the optimized PB treatment plan was recalculated using the MC algorithm with the corresponding MC parameters. The term "**dose**", used in the following chapters, refers to treatment plans generated with this approach.
2. The optimized PB dose distribution was recalculated using the MC algorithm ("**dose**") and optimized afterwards. The term "**opt**", used in the following chapters, refers to this approach.

Gantry Angle [°]	Type	unc	err	D.C.T. [s]	HI	CI	$D_{2\%}$ [%]	$D_{98\%}$ [%]	$V_{95\%}$ [%]
0	PB (opt)	-	-	26	0.046	0.823	101.6	97.0	99.7
	MC (dose)	0.05	0.6	223	0.108	0.750	105.0	94.1	97.1
	MC (opt)	0.05	0.6	223	0.097	0.723	104.9	95.2	98.4
	MC (dose)	0.05	0.1	585	0.105	0.750	104.7	94.1	97.1
	MC (opt)	0.05	0.1	585	0.099	0.717	104.9	95.0	98.1
	MC (dose)	0.04	0.6	343	0.107	0.750	104.8	94.1	97.0
	MC (opt)	0.04	0.6	343	0.100	0.721	104.9	94.9	97.7
	MC (dose)	0.04	0.1	905	0.104	0.752	104.6	94.2	97.2
	MC (opt)	0.04	0.1	905	0.102	0.710	104.9	94.7	97.2
	MC (dose)	0.03	0.6	611	0.106	0.752	104.6	94.1	97.1
	MC (opt)	0.03	0.6	611	0.099	0.727	104.9	95.0	98.1
	MC (dose)	0.03	0.1	1597	0.104	0.751	104.6	94.1	97.1
	MC (opt)	0.03	0.1	1597	0.102	0.715	105.0	94.9	97.6
	MC (dose)	0.02	0.6	1352	0.105	0.751	104.6	94.0	97.0
	MC (opt)	0.02	0.6	1352	0.104	0.709	105.0	94.7	97.3
	MC (dose)	0.02	0.1	3545	0.104	0.751	104.6	94.1	97.1
MC (opt)	0.02	0.1	3545	0.103	0.709	105.1	94.8	97.4	
MC (dose)	0.01	0.6	3329	0.104	0.751	104.6	94.1	97.1	
MC (opt)	0.01	0.6	3329	0.103	0.707	105.0	94.7	97.2	
MC (dose)	0.01	0.1	7553	0.104	0.751	104.6	94.1	97.1	
MC (opt)	0.01	0.1	7553	0.103	0.706	105.1	94.9	97.6	
15	PB (opt)	-	-	29	0.049	0.692	101.4	96.6	99.5
	MC (dose)	0.05	0.6	292	0.097	0.633	103.6	93.9	97.3
	MC (opt)	0.05	0.6	292	0.061	0.634	102.7	96.6	99.6
	MC (dose)	0.05	0.1	715	0.095	0.634	103.6	94.0	97.3
	MC (opt)	0.05	0.1	715	0.048	0.640	102.0	97.2	99.8
	MC (dose)	0.04	0.6	455	0.095	0.635	103.7	94.1	97.3
	MC (opt)	0.04	0.6	455	0.059	0.640	102.6	96.8	99.7
	MC (dose)	0.04	0.1	1114	0.094	0.635	103.5	94.1	97.4
	MC (opt)	0.04	0.1	1114	0.049	0.643	102.1	97.1	99.7
	MC (dose)	0.03	0.6	783	0.095	0.634	103.5	94.0	97.3
	MC (opt)	0.03	0.6	783	0.049	0.644	101.9	97.0	99.8
	MC (dose)	0.03	0.1	1962	0.094	0.636	103.4	94.1	97.4
	MC (opt)	0.03	0.1	1962	0.050	0.645	101.9	96.9	99.7
	MC (dose)	0.02	0.6	1733	0.094	0.626	103.4	93.9	97.3
	MC (opt)	0.02	0.6	1733	0.049	0.644	101.9	97.0	99.6
	MC (dose)	0.02	0.1	4397	0.093	0.635	103.4	94.0	97.4
MC (opt)	0.02	0.1	4397	0.046	0.643	101.8	97.2	99.7	

Table 4.2: Dose calculation times (D.C.T) and dosimetric evaluation parameters for different MCuncertainty (unc) and MCerrordosethreshold (err) values of the chess target with a gantry angle of 0° and 15°.

For a gantry angle of 0°, the HI increased from 0.046 for PB to a mean HI of 0.105 for the recalculated MC treatment plans (increase by a factor of 2.3) and from 0.049 for PB to 0.095 for MC (increase by a factor of 1.9) for a gantry angle of 15°, with decreasing tendency for more accurate MC parameter settings. It can be seen, that the calculated HI and CI values differed only slightly when using different MC parameters. For a gantry angle of 0°, the HI of the recalculated treatment plan for example improved by 4.3%, when using the MC parameters of unc=0.02, err=0.1 instead of unc=0.05, err=0.6 and the CI improved by 0.2%.

Using a gantry angle of 0°, the HI of the optimized treatment plan improved between 0.7% (unc=0.02, err=0.1) and 10% (unc=0.05, err=0.6) in comparison to the recalculated treatment plan, whereas the CI of the optimized treatment plan declined by minimum 3.3% (unc=0.03, err=0.6) and maximum 6% (unc=0.01, err=0.1). Using a gantry angle of 15°, the HI of the optimized treatment plan improved between 36.6% (unc=0.05, err=0.6) and 50.5% (unc=0.02, err=0.1) in comparison to the recalculated treatment plan and the CI improved between 0.2% (unc=0.05, err=0.6) and 2.8% (unc=0.02, err=0.6). Furthermore, the optimization process achieved an improvement in the dose-volume parameters $D_{98\%}$ (1.1% for unc=0.5, err=0.6) and $V_{95\%}$ (1.3% for unc=0.5, err=0.6) when using a gantry angle of 0° and 3.2% for unc=0.2, err=0.1 and 2.5% for unc=0.5, err=0.1, respectively when using a gantry angle of 15°.

The dose calculation time differed essentially. The more accurate the calculation was, the more time was required for dose calculation. For a demonstrative comparison, the homogeneity index was plotted against the MCuncertainty, as shown in Figure 4.1.

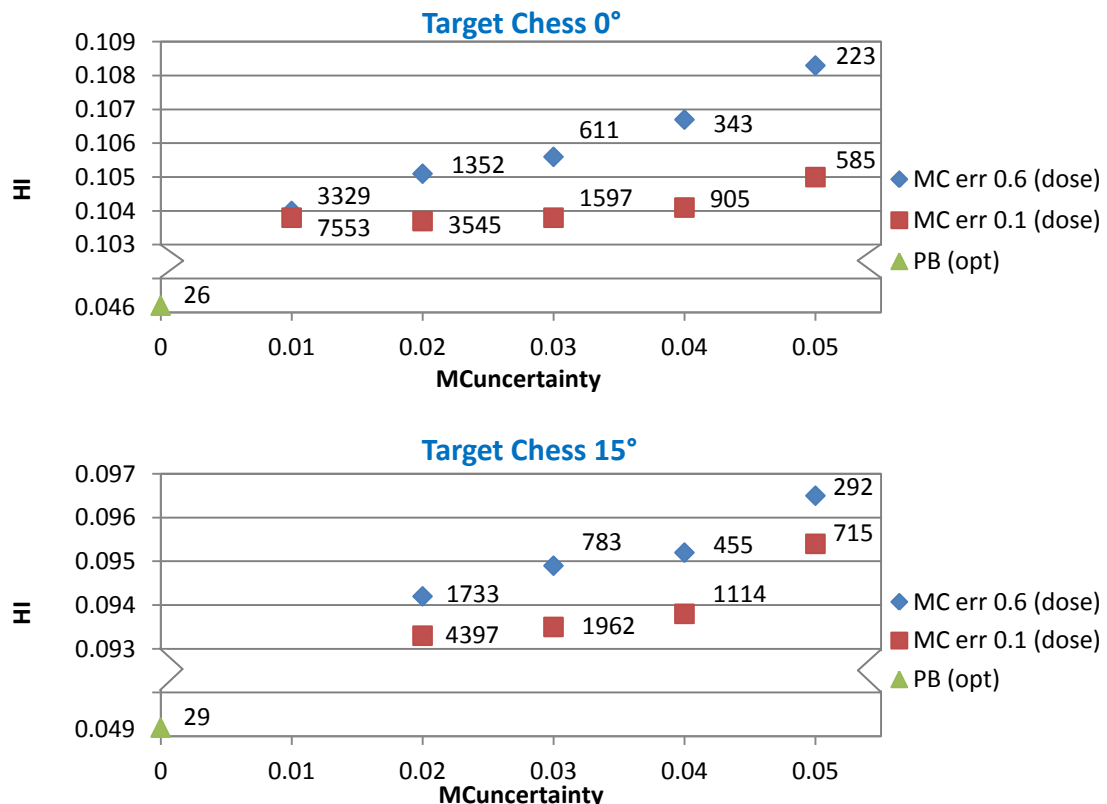


Figure 4.1: Dose homogeneity of the recalculated treatment plans using the Chess Target with a gantry angle of 0° and 15° with respect to changes of MC parameters including dose calculation times [s] presented next to the data marker.

The dose calculation required between 10% and 25% more time when using a gantry angle of 15° instead of 0°.

Better HI and CI values could be obtained when using $err=0.1$ instead of $err=0.6$. The treatment plan (gantry angle 0°) generated with $unc=0.05$ and $err=0.1$ e.g. achieved nearly the same homogeneity as the treatment plan generated with $unc=0.02$ and $err=0.6$, although the dose calculation time increased by more than a factor of two for the second plan. For both beam incidence angles the treatment plan generated with the MC parameters of $unc=0.03$ and $err=0.01$ achieved good results with regards to the HI and CI values and the dose calculation time. More accurate MC parameters like $unc=0.02$ or $unc=0.01$ with $err=0.1$ achieved almost no better HI or CI values whereas the dose calculation time increased essentially. With respect to short dose calculation time, the MC parameter setting of $unc=0.05$ and $err=0.6$ seem to be a good choice.

Comparison of MC and PB results

This chapter covers the evaluation of the differences between the treatment plans calculated with the MC and the PB algorithm. The analysis was done on the basis of isodose distributions (chapter 2.13.1), dose-difference maps (chapter 2.13.6) and γ -index evaluation (chapter 2.13.7). Figure 4.2 shows isodose distributions of the treatments plans calculated with the PB and the MC algorithm. The corresponding dose difference-maps are shown in Figure 4.3 (gantry angle of 0°) and in Figure 4.4 (gantry angle of 15°).

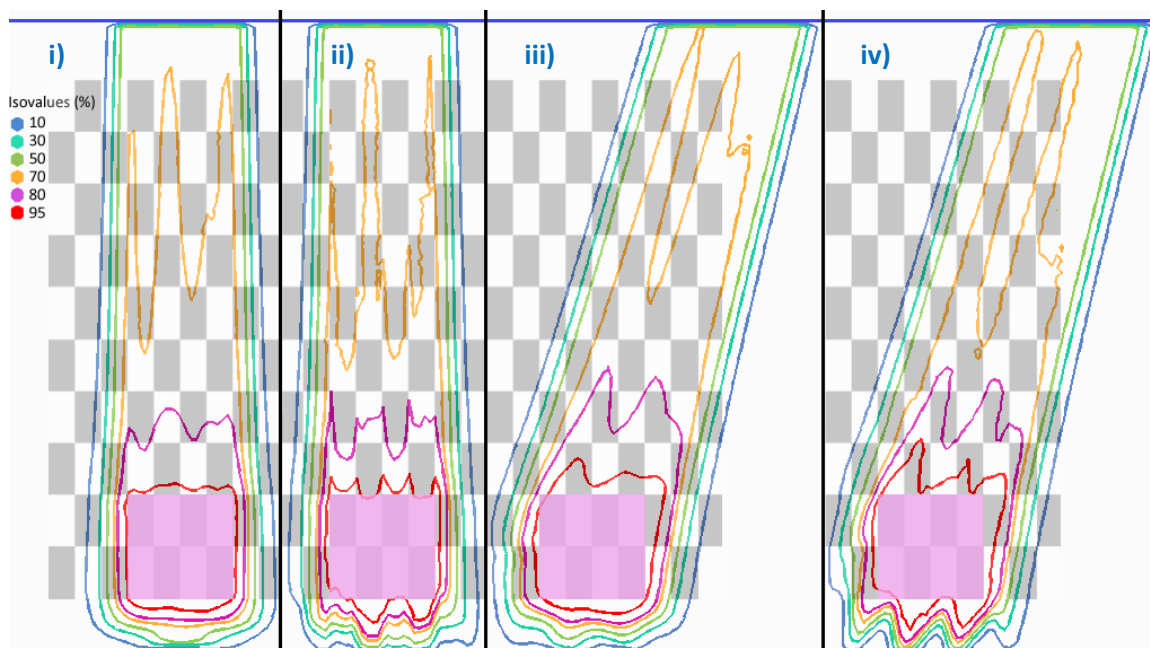


Figure 4.2: Isodose distributions of the Chess Target using a gantry angle of 0° i) PB opt, ii) MC dose ($unc=0.05$, $err=0.6$) and 15° iii) PB opt, iv) MC dose ($unc=0.05$, $err=0.6$).

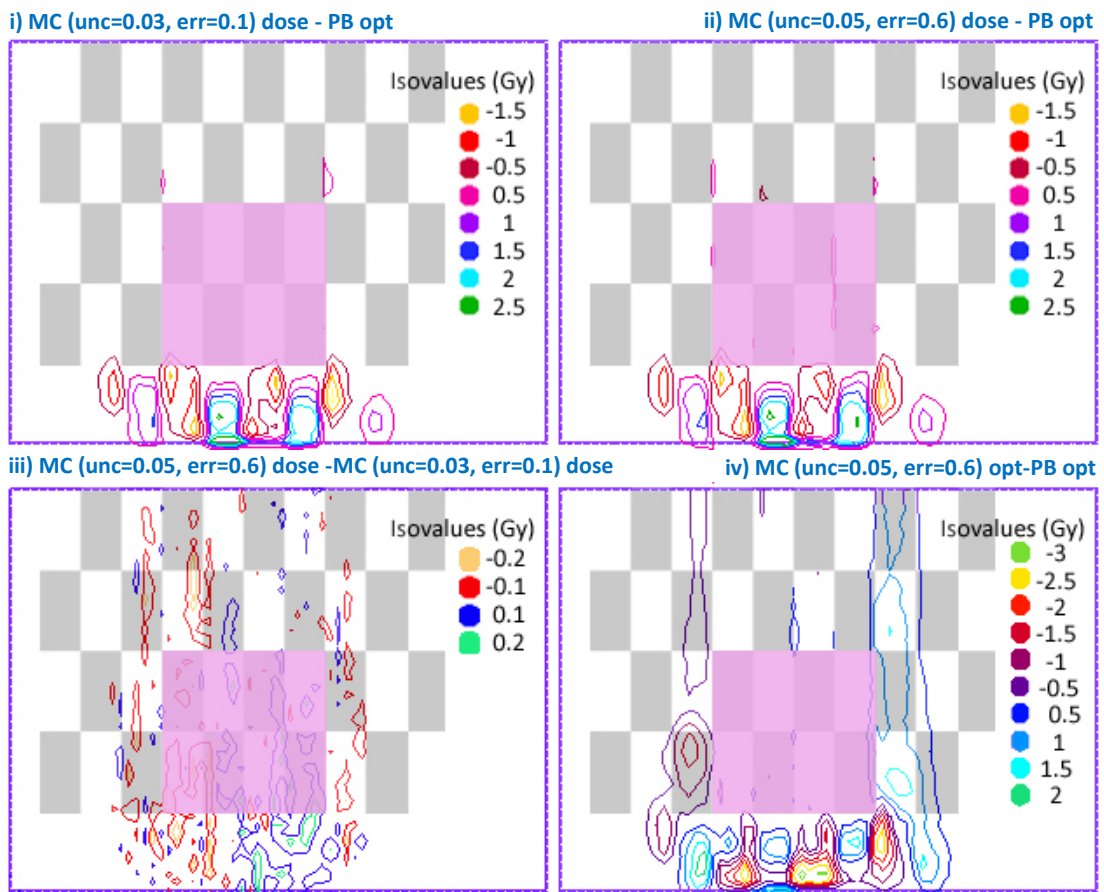


Figure 4.3: Dose-difference maps (gantry angle 0°) using different MC parameter combinations.

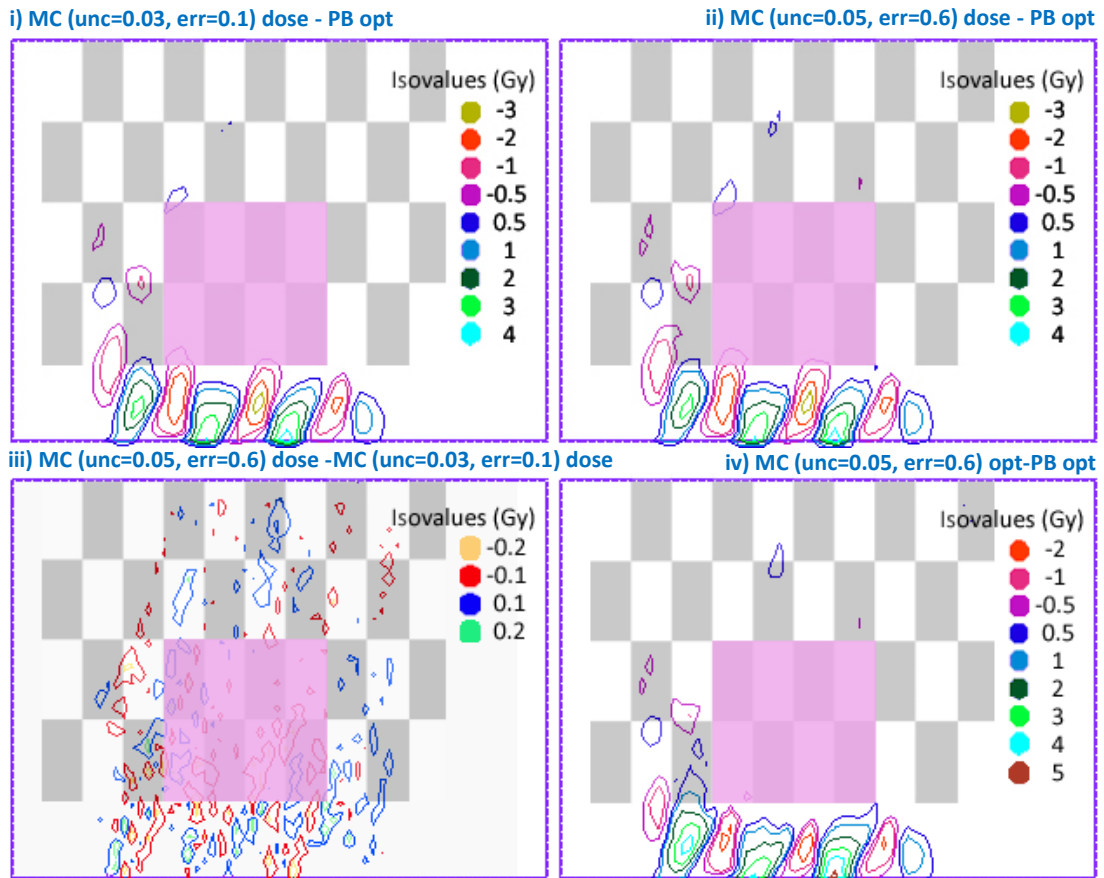


Figure 4.4: Dose-difference maps (gantry angle 15°) using different MC parameter combinations.

Figure 4.3 i) - iii) and Figure 4.4 i) - iii) show that changes in the MC parameters created only minor variations in the dose distribution. For a gantry angle of 0°, the dose calculation time was 1597 s for the MC parameter settings of $unc=0.03$, $err=0.1$ (Figure 4.3 i)) and 223 s for $unc=0.05$, $err=0.6$ (Figure 4.3 ii)), which correspond to an increase in the dose calculation time by a factor of 7.2. In contrast, the dose calculation time of the PB treatment plan was 26 s only.

With 1962 s for the MC parameter settings of $unc=0.03$, $err=0.1$ (Figure 4.4 i)) and 292 s for $unc=0.05$, $err=0.6$ (Figure 4.4 ii)) for a gantry angle of 15°, the time required to calculate the dose distribution increased by a factor of 6.7. For comparison, the dose calculation time of the PB treatment plan was 29 s.

A dose difference between the MC and the PB algorithm of up to 20% (gantry angle of 0°) and 40% (gantry angle of 15°) could be observed in some areas of the dose-difference map. The MC algorithm deposited more dose to the areas located behind the lung tissue whereas the PB algorithm deposited more dose to the areas located behind the bone tissue. This means that more radiation was absorbed by the bone tissue when using the MC algorithm instead of the PB algorithm. Moreover, low density tissue like lung tissue was more transparent to radiation when using the MC algorithm instead of the PB algorithm which resulted in a higher dose deposition behind the low density tissue. These different dose deposition characteristics of the MC and PB algorithm are visible in Figure 4.2 as well, as the MC algorithm deposited more dose behind the cuboids consisting of lung tissue, whereas nearly no dose was deposited behind the cuboids consisting of bone tissue. This resulted in a zigzag course of the isodose distribution behind the target and the inhomogeneities depicted in Figure 4.2 ii) and iv). This behavior of the MC algorithm explains the higher dose difference to the PB algorithm of up to 40% when using a gantry angle of 15°.

For the γ -index evaluation of the MC parameter settings the criteria $\Delta D = 2\%$ (dose-difference) and $\Delta d = 2\text{ mm}$ (distance-to-agreement), also written as $2\%/2\text{mm}$, was used because two algorithms were compared and only minor differences were expected. For all cases, a global dose-difference criterion of the maximum dose was used and the optimized PB treatment plan served as reference dose. The low dose threshold was set to 5%.

γ -index analysis of the whole treatment plan (gantry angle 0°) revealed a failure rate ($\gamma \geq 1$) of 1.7% for all recalculated treatment plans (“dose”) and 4% for all optimized (“opt”) treatment plans. As explained in Table 2.2 in chapter 2.13.7, a plan is accepted if the failure rate of the whole treatment plan doesn’t exceed 5%. Furthermore, γ -index analysis displayed $\gamma_{1\%}$ values of 1.3 (dose) and 2 (opt) and γ_{mean} values of 0.07 (dose) and 0.15 (opt), respectively. In the best case $\gamma_{1\%}$ should be between 0 and 1.5 and γ_{mean} values should be between 0 and 0.5. Nearly all evaluated data met the suggested constraints.

For a better evaluation of the treatment plans, the γ -index analysis was limited to a reduced area around the various targets. This area included the target volume with a 3D margin of 30 mm around it, as shown in Figure 4.5.

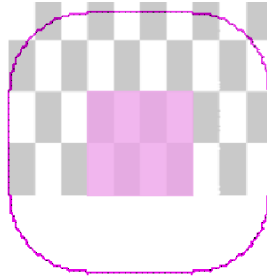


Figure 4.5: Chess Target with 30 mm margin for the γ -index analysis.

For the Chess Target with a gantry angle of 0° the following γ -values (2%/2mm) arose for the reduced area of 30 mm around the target:

Type	unc	err	$\gamma \geq 1$ (fail)	$\gamma \leq 1$ (pass)	γ_{mean}	$\gamma_{1\%}$
MC (dose)	0.05	0.6	14.6%	85.4%	0.45	2.95
MC (opt)	0.05	0.6	17.6%	82.4%	0.59	3.15
MC (dose)	0.05	0.1	14.6%	85.4%	0.44	2.98
MC (opt)	0.05	0.1	18.2%	81.8%	0.60	3.25
MC (dose)	0.04	0.6	14.5%	85.5%	0.45	2.96
MC (opt)	0.04	0.6	18.0%	82.0%	0.59	3.16
MC (dose)	0.04	0.1	14.3%	85.7%	0.44	2.97
MC (opt)	0.04	0.1	19.2%	80.8%	0.62	3.28
MC (dose)	0.03	0.6	14.5%	85.5%	0.44	2.98
MC (opt)	0.03	0.6	18.0%	82.0%	0.59	3.13
MC (dose)	0.03	0.1	14.5%	85.5%	0.43	2.97
MC (opt)	0.03	0.1	18.7%	81.3%	0.61	3.24
MC (dose)	0.02	0.6	14.4%	85.6%	0.44	2.98
MC (opt)	0.02	0.6	19.5%	80.5%	0.63	3.37
MC (dose)	0.02	0.1	14.3%	85.7%	0.43	2.97
MC (opt)	0.02	0.1	19.3%	80.7%	0.62	3.39
MC (dose)	0.01	0.6	14.4%	85.6%	0.43	2.97
MC (opt)	0.01	0.6	19.3%	80.7%	0.62	3.32
MC (dose)	0.01	0.1	14.3%	85.7%	0.43	2.97
MC (opt)	0.01	0.1	19.0%	81.0%	0.63	3.36

Table 4.3: Failure rate, γ_{mean} and $\gamma_{1\%}$ values for different MCuncertainty (unc) and MCerrordosethreshold (err) values of the Chess Target using a gantry angle of 0° .

Evaluation of the γ -analysis of the reduced area showed that no trend could be observed and that the difference between selected MC parameters was very small. For example the failure rate of the recalculated treatment plan in the reduced area improved by 2.1% only, when using the MC parameters of unc=0.02, err=0.1 instead of unc=0.05, err=0.6. The highest differences found between PB and the recalculated MC treatment plans were a failure rate of 14.6% (unc=0.05, err=0.6), a γ_{mean} of 0.45 (unc=0.05, err=0.6) and a $\gamma_{1\%}$ of 3 (unc=0.02, err=0.6). These values were still in good agreement with the PB treatment plan, regarding the fact that only an area of 30 mm around the target and not the whole treatment plan was investigated.

The failure rate of the optimized treatment plans was larger than the failure rate of the recalculated plans, with differences between $\Delta_{min}(\gamma \geq 1)=3.0\%$ (unc=0.05, err=0.6) and $\Delta_{max}(\gamma \geq 1)=5.1\%$ (unc=0.02, err=0.6). This difference was due to the optimization process which increased the difference between the treatment plans. With every optimization process the spot intensity weighting is different and therefore the difference between PB and MC can increase.

For the Chess Target with a gantry angle of 15° the following γ -values (2%/2mm) arose for the reduced area of 30 mm around the target:

Type	unc	err	$\gamma \geq 1$ (fail)	$\gamma \leq 1$ (pass)	γ_{mean}	$\gamma_{1\%}$
MC (dose)	0.05	0.6	13.7%	86.3%	0.51	3.19
MC (opt)	0.05	0.6	15.5%	84.5%	0.58	3.41
MC (dose)	0.05	0.1	13.2%	86.8%	0.50	3.18
MC (opt)	0.05	0.1	14.2%	85.8%	0.57	3.35
MC (dose)	0.04	0.6	13.5%	86.5%	0.50	3.18
MC (opt)	0.04	0.6	14.2%	85.8%	0.59	3.46
MC (dose)	0.04	0.1	13.2%	86.8%	0.50	3.19
MC (opt)	0.04	0.1	13.6%	86.4%	0.55	3.31
MC (dose)	0.03	0.6	13.3%	86.7%	0.50	3.19
MC (opt)	0.03	0.6	13.6%	86.4%	0.56	3.25
MC (dose)	0.03	0.1	13.2%	86.8%	0.49	3.19
MC (opt)	0.03	0.1	13.0%	87.0%	0.54	3.28
MC (dose)	0.02	0.6	13.3%	86.7%	0.50	3.19
MC (opt)	0.02	0.6	13.0%	87.0%	0.55	3.28
MC (dose)	0.02	0.1	13.0%	87.0%	0.49	3.18
MC (opt)	0.02	0.1	12.9%	87.1%	0.55	3.29

Table 4.4: Failure rate, γ_{mean} and $\gamma_{1\%}$ values for different MCuncertainty (unc) and MCerrordosethreshold (err) values of the Chess Target using a gantry angle of 15°.

Similar to the γ -index evaluation of the treatment plans using a gantry angle of 0°, only minor differences could be observed between the selected MC parameters.

The highest differences found between PB and the recalculated MC treatment plans were a failure rate of 13.7%, a γ_{mean} of 0.51 and a $\gamma_{1\%}$ of 3.2, all for unc=0.05, err=0.6.

Up to the MC parameters of unc=0.03, err=0.1 the failure rate for the optimized treatment plan was larger than for the recalculated plans ($\Delta_{max}(\gamma \geq 1)=1.8\%$). In contrast to the 0° gantry angle plans, a trend towards a decreasing difference between the recalculated and optimized treatment plan could be observed, when more accurate MC parameters were set.

4.1.3 Evaluation of Target 1, 2 and 3

In the next step treatment plans for the cubic targets located behind the chess pattern structure were calculated. For all three targets, the beam incidence angle was set to 270° in order to have a beam direction passing through the chess pattern before reaching the target (chapter 3.3.3). Table 4.5, Table 4.6 and Table 4.7 show the dose calculation times and dosimetric evaluation parameters for different MC parameter settings for Target 1, 2 and 3 respectively.

Type	unc	err	D.C.T [s]	HI	CI	$D_{2\%}$ [%]	$D_{98\%}$ [%]	$V_{95\%}$ [%]
PB (opt)	-	-	15	0.081	0.840	103.8	95.7	99.5
MC (dose)	0.05	0.6	327	0.094	0.777	105.5	96.0	99.3
MC (opt)	0.05	0.6	327	0.089	0.770	104.6	95.6	98.9
MC (dose)	0.05	0.1	475	0.093	0.775	105.5	96.0	99.2
MC (opt)	0.05	0.1	475	0.088	0.768	104.7	95.7	99.0
MC (dose)	0.04	0.6	503	0.093	0.776	105.5	96.0	99.3
MC (opt)	0.04	0.6	503	0.089	0.756	104.7	95.7	99.2
MC (dose)	0.04	0.1	737	0.093	0.776	105.4	96.0	99.3
MC (opt)	0.04	0.1	737	0.088	0.771	104.6	95.7	98.9
MC (dose)	0.03	0.6	892	0.093	0.776	105.4	96.0	99.3
MC (opt)	0.03	0.6	892	0.089	0.769	104.7	95.7	99.1
MC (dose)	0.03	0.1	1298	0.092	0.777	105.4	96.0	99.3
MC (opt)	0.03	0.1	1298	0.088	0.768	104.7	95.8	99.1
MC (dose)	0.02	0.6	1970	0.092	0.777	105.4	96.0	99.2
MC (opt)	0.02	0.6	1970	0.089	0.774	104.7	95.7	99.0
MC (dose)	0.02	0.1	2883	0.092	0.777	105.4	96.0	99.3
MC (opt)	0.02	0.1	2883	0.088	0.768	104.7	95.8	99.1

Table 4.5: Dose calculation times (D.C.T) and dosimetric evaluation parameters for different MCuncertainty (unc) and MCerrordosethreshold (err) values when using Target 1.

Type	unc	err	D.C.T [s]	HI	CI	$D_{2\%}$ [%]	$D_{98\%}$ [%]	$V_{95\%}$ [%]
PB (opt)	-	-	16	0.039	0.829	101.0	97.1	99.9
MC (dose)	0.05	0.6	353	0.056	0.782	103.4	97.7	99.7
MC (opt)	0.05	0.6	353	0.046	0.825	101.5	96.9	99.6
MC (dose)	0.05	0.1	530	0.054	0.784	103.1	97.7	99.8
MC (opt)	0.05	0.1	530	0.043	0.811	101.3	97.0	99.6
MC (dose)	0.04	0.6	540	0.055	0.784	103.2	97.7	99.8
MC (opt)	0.04	0.6	540	0.046	0.825	101.4	96.8	99.6
MC (dose)	0.04	0.1	820	0.053	0.784	103.1	97.7	99.8
MC (opt)	0.04	0.1	820	0.045	0.819	101.3	96.8	99.6
MC (dose)	0.03	0.6	940	0.053	0.783	103.1	97.7	99.8
MC (opt)	0.03	0.6	940	0.045	0.820	101.3	96.8	99.6
MC (dose)	0.03	0.1	1429	0.052	0.784	103.0	97.7	99.8
MC (opt)	0.03	0.1	1429	0.043	0.810	101.2	97.0	99.7
MC (dose)	0.02	0.6	2079	0.053	0.785	103.0	97.7	99.8
MC (opt)	0.02	0.6	2079	0.044	0.817	101.2	96.8	99.7
MC (dose)	0.02	0.1	3173	0.053	0.785	103.0	97.7	99.8
MC (opt)	0.02	0.1	3173	0.044	0.815	101.2	96.8	99.7

Table 4.6: Dose calculation times (D.C.T) and dosimetric evaluation parameters for different MCuncertainty (unc) and MCerrordosethreshold (err) values when using Target 2.

Type	unc	err	D.C.T [s]	HI	CI	$D_{2\%}$ [%]	$D_{98\%}$ [%]	$V_{95\%}$ [%]
PB (opt)	-	-	16	0.053	0.779	101.7	96.4	99.8
MC (dose)	0.05	0.6	333	0.072	0.781	103.9	96.6	99.6
MC (opt)	0.05	0.6	333	0.069	0.732	103.5	96.6	99.8
MC (dose)	0.05	0.1	533	0.070	0.776	103.8	96.7	99.7
MC (opt)	0.05	0.1	533	0.068	0.733	103.3	96.5	99.9
MC (dose)	0.04	0.6	510	0.071	0.772	103.8	96.7	99.7
MC (opt)	0.04	0.6	510	0.069	0.732	103.3	96.4	99.8
MC (dose)	0.04	0.1	818	0.070	0.774	103.7	96.7	99.7
MC (opt)	0.04	0.1	818	0.068	0.732	103.1	96.3	99.9
MC (dose)	0.03	0.6	875	0.070	0.774	103.7	96.7	99.7
MC (opt)	0.03	0.6	875	0.069	0.732	103.2	96.3	99.8
MC (dose)	0.03	0.1	1405	0.069	0.774	103.7	96.7	99.7
MC (opt)	0.03	0.1	1405	0.069	0.731	103.1	96.3	99.8
MC (dose)	0.02	0.6	1926	0.069	0.772	103.7	96.7	99.7
MC (opt)	0.02	0.6	1926	0.069	0.731	103.0	96.1	99.8
MC (dose)	0.02	0.1	3099	0.069	0.772	103.7	96.7	99.8
MC (opt)	0.02	0.1	3099	0.069	0.732	102.9	96.1	99.8

Table 4.7: Dose calculation times (D.C.T) and dosimetric evaluation parameters for different MCuncertainty (unc) and MCerrordosethreshold (err) values when using Target 3.

The distance to the inhomogeneities and the targets influenced the dose homogeneity. The mean HI values for the recalculated MC treatment plans were $HI_{\text{mean}}=0.09$ for a distance of 10 mm to the inhomogeneities (Target 1), $HI_{\text{mean}}=0.05$ for a distance of 20 mm (Target 2) and $HI_{\text{mean}}=0.07$ for a distance of 30 mm (Target 3). This corresponds to an increase of the HI in comparison to the PB treatment plan by a factor of 1.2 for Target 1, 1.4 for Target 2 and 1.3 for Target 3. In comparison, the HI increased by a factor of 2.3 (gantry angle 0°) and 1.9 (gantry angle 15°) when using the target located within the chess pattern structure. This difference in the increase might be explained by the position and composition of the targets, as the target located in the chess pattern structure was made of alternating cuboids consisting of bone and lung tissue whereas the targets located proximal to the chess pattern consisted of water. As the PB dose calculation is more accurate in homogenous media, the difference to the MC algorithm decreases.

An improvement in the HI of the recalculated MC plans of 1.71% (Target 1), 6.75% (Target2) and 3.76% (Target 3) could be observed when using the MC parameters of $unc=0.02$, $err=0.1$ instead of $unc=0.05$, $err=0.6$. Optimization process improved the HI of the treatment plan between 3.6% ($unc=0.02$, $err=0.6$) and 5.9% ($unc=0.05$, $err=0.1$) for Target 1, between 16.6% ($unc=0.02$, $err=0.1$) and 19.2% ($unc=0.05$, $err=0.6$) for Target 2 and between 0.4% ($unc=0.02$, $err=0.6$) and 3.5% ($unc=0.05$, $err=0.6$) for Target 3.

The CI was influenced by the distance to the inhomogeneities as well. For 10 mm distance the conformity index was 0.84 for the PB and approximately 0.78 for the MC algorithm independent of the MC parameter settings. For 20 mm distance the CI was 0.83 for the PB and approximately 0.78 for the MC algorithm. However, for 30 mm nearly no difference in the conformity index values could be observed between the PB and MC treatment plans.

For a demonstrative comparison, the homogeneity index was plotted against the MCuncertainty, as shown in Figure 4.6.

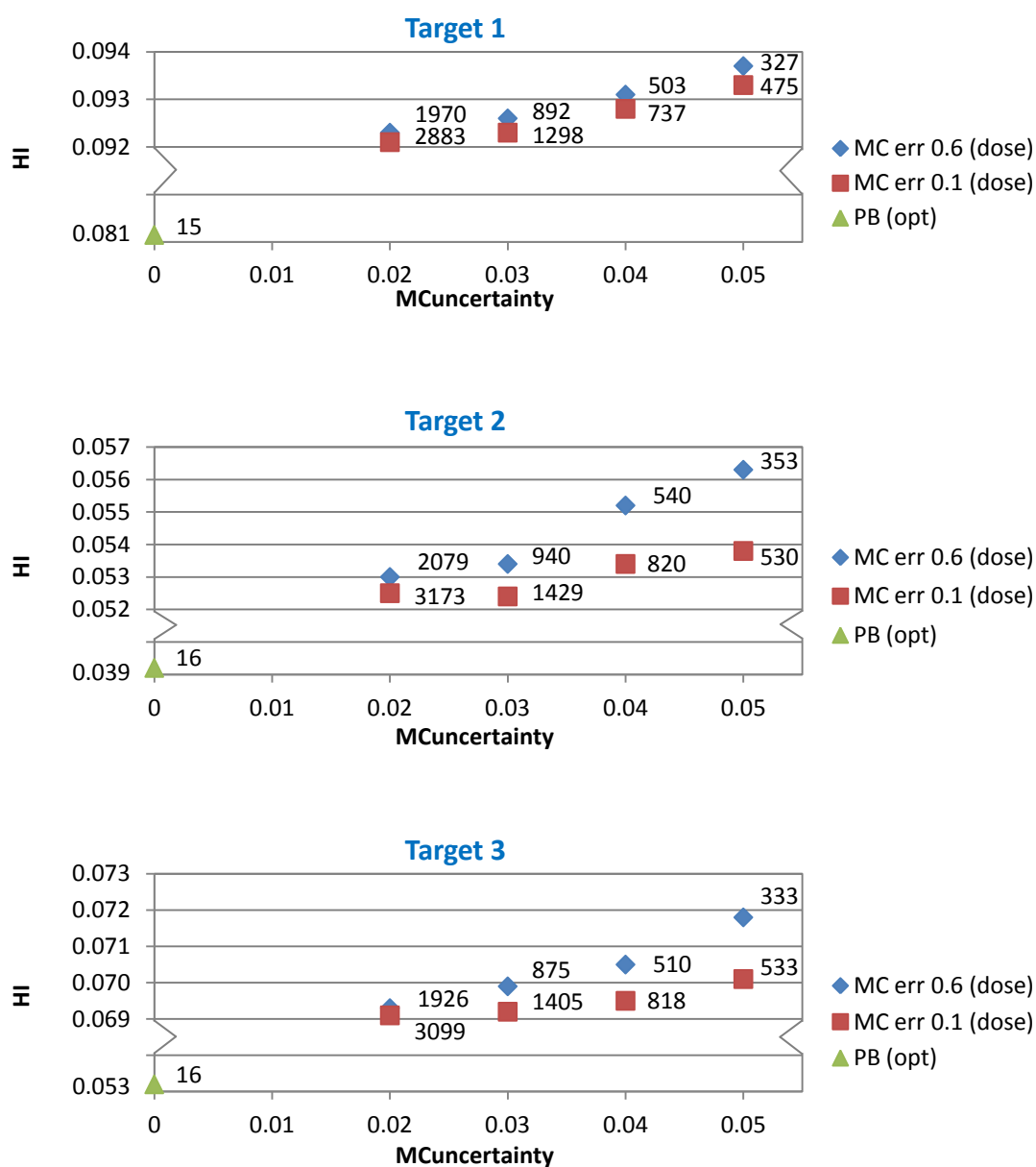


Figure 4.6: Dose homogeneity of the recalculated treatments plans when using Target 1, 2 and 3 with respect to changes of MC parameters including dose calculation times [s] presented next to the data marker.

Similar to the Chess Target, better HI and CI values could be achieved when using err=0.1 instead of err=0.6, although the difference was insignificant for Target 1. The treatment plans generated with the MC parameters of unc=0.03 and err=0.1 achieved HI and CI values comparable to those of the PB algorithm while maintaining adequate dose calculation times. This MC parameter setting, together with the MC parameter of unc=0.05 and err=0.6 - which achieves acceptable results in less time - can be considered for the review of the clinical applicability using selected patient data sets.

Comparison of MC and PB results

Figure 4.7, Figure 4.8 and Figure 4.9 show dose-difference maps of the optimized PB treatment plan subtracted voxel per voxel from the recalculated or optimized MC treatment plan using different MC parameter settings. Target 1, 2 and 3 served as target structures.

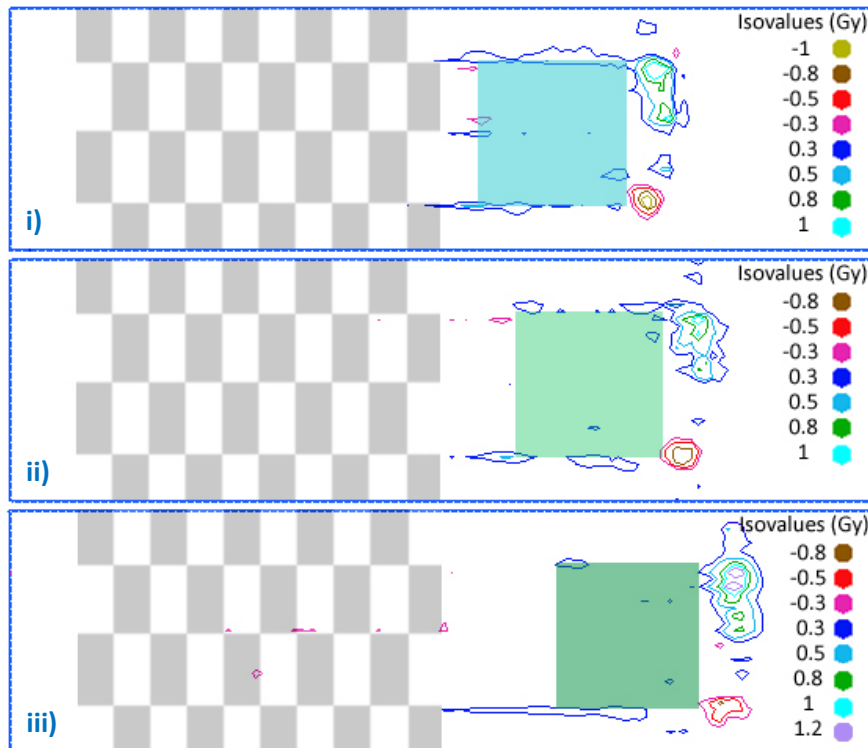


Figure 4.7: Dose-difference maps of the recalculated MC (unc=0.05, err=0.6) – optimized PB treatment plan for i) Target 1, ii) Target 2 and iii) Target 3.

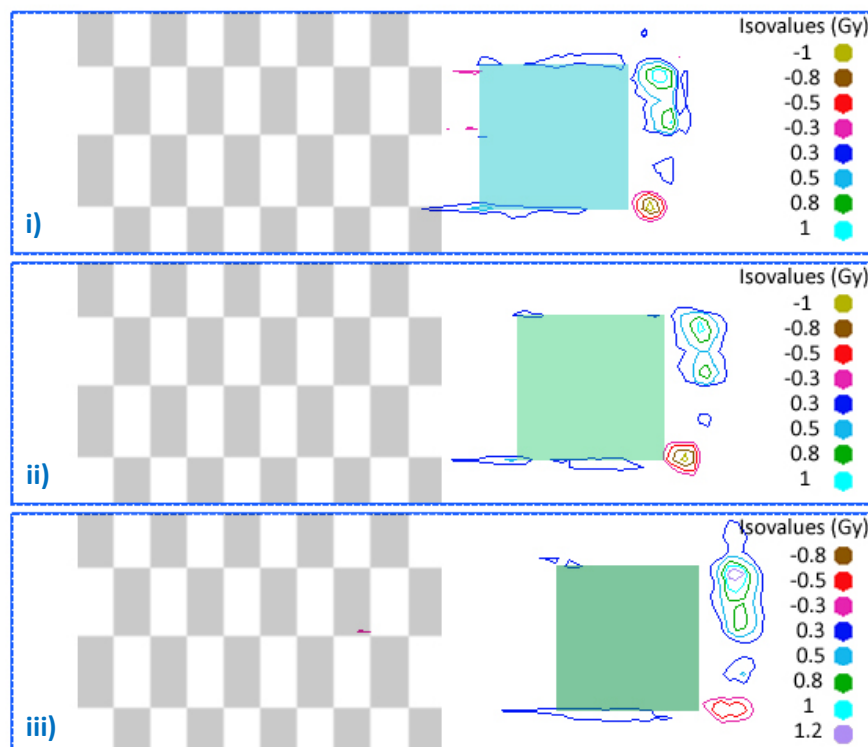


Figure 4.8: Dose-difference maps of the recalculated MC (unc=0.03, err=0.1) – optimized PB treatment plan for i) Target, 1 ii) Target 2 and iii) Target 3.

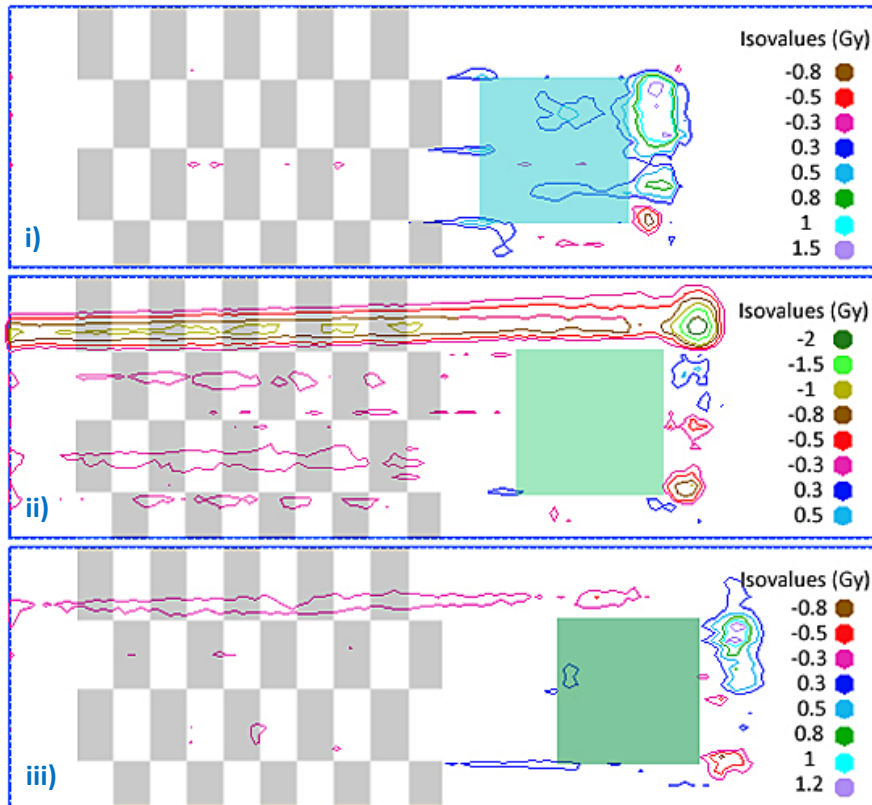


Figure 4.9: Dose-difference maps of the optimized MC (unc=0.05, err=0.6) – optimized PB treatment plan for i) Target 1, ii) Target 2 and iii) Target 3.

Figure 4.7, Figure 4.8 and Figure 4.9 show that in large parts the dose difference between the MC and PB algorithm was small. Nevertheless, there were some areas where a dose difference of up to 10% could be observed. This difference was less than for the target located in the chess pattern structure, where a difference of up to 20% (gantry angle 0°) and 40% (gantry angle 15°) could be found. This reduction in the dose difference between the MC and PB algorithm can be explained by the more accurate dose calculation of the PB algorithm in homogenous media.

Figure 4.7 and Figure 4.8 show that the PB algorithm deposited more dose to one spot located behind the bottom right corner of all three targets, whereas the MC algorithm deposited more dose to spots located behind the top right corner. This different dose deposition might be due to the different composition of air and bone tissue of the chess pattern structure in front of the targets.

Figure 4.9 illustrates dose-difference maps comparing the optimized MC dose distribution with the optimized PB dose distribution. The dose difference (up to 20%) increased in comparison to the recalculated treatment plans due to the optimization process, as the spot intensity weighting is different and therefore the difference can increase.

The results obtained with γ -index analysis (2%/2mm) for the reduced area of 30 mm around the targets are shown in Table 4.8 for Targets 1, Table 4.9 for Target 2 and Table 4.10 for Target 3 located 10 mm, 20 mm and 30 mm proximal to the chess pattern structure. The treatment plan calculated with the PB algorithm served as reference dose.

Type	unc	err	$\gamma \geq 1$ (fail)	$\gamma \leq 1$ (pass)	γ_{mean}	$\gamma_{1\%}$
MC (dose)	0.05	0.6	4.7%	95.3%	0.27	1.50
MC (opt)	0.05	0.6	7.6%	92.4%	0.33	2.00
MC (dose)	0.05	0.1	4.3%	95.7%	0.26	1.46
MC (opt)	0.05	0.1	7.4%	92.6%	0.32	1.88
MC (dose)	0.04	0.6	4.5%	95.5%	0.26	1.49
MC (opt)	0.04	0.6	8.3%	91.7%	0.36	2.65
MC (dose)	0.04	0.1	4.4%	95.6%	0.26	1.46
MC (opt)	0.04	0.1	6.6%	93.4%	0.30	1.83
MC (dose)	0.03	0.6	4.3%	95.7%	0.26	1.45
MC (opt)	0.03	0.6	7.6%	92.4%	0.32	2.00
MC (dose)	0.03	0.1	4.3%	95.7%	0.26	1.43
MC (opt)	0.03	0.1	6.9%	93.1%	0.32	1.96
MC (dose)	0.02	0.6	4.1%	95.9%	0.25	1.41
MC (opt)	0.02	0.6	6.2%	93.8%	0.30	1.82
MC (dose)	0.02	0.1	4.1%	95.9%	0.25	1.41
MC (opt)	0.02	0.1	6.5%	93.5%	0.30	1.92

Table 4.8: Failure rate, γ_{mean} and $\gamma_{1\%}$ values for different MCuncertainty (unc) and MCerror dosethreshold (err) values when using Target 1.

Type	unc	err	$\gamma \geq 1$ (fail)	$\gamma \leq 1$ (pass)	γ_{mean}	$\gamma_{1\%}$
MC (dose)	0.05	0.6	4.3%	95.7%	0.27	1.42
MC (opt)	0.05	0.6	7.4%	92.6%	0.33	2.00
MC (dose)	0.05	0.1	3.9%	96.1%	0.26	1.34
MC (opt)	0.05	0.1	7.3%	92.7%	0.33	1.89
MC (dose)	0.04	0.6	4.1%	95.9%	0.26	1.37
MC (opt)	0.04	0.6	7.2%	92.8%	0.31	1.98
MC (dose)	0.04	0.1	3.6%	96.4%	0.26	1.31
MC (opt)	0.04	0.1	6.9%	93.1%	0.31	1.98
MC (dose)	0.03	0.6	3.8%	96.2%	0.26	1.32
MC (opt)	0.03	0.6	6.9%	93.1%	0.31	1.93
MC (dose)	0.03	0.1	3.4%	96.6%	0.25	1.29
MC (opt)	0.03	0.1	6.9%	93.1%	0.32	1.99
MC (dose)	0.02	0.6	3.5%	96.5%	0.25	1.29
MC (opt)	0.02	0.6	7.0%	93.0%	0.32	2.00
MC (dose)	0.02	0.1	3.5%	96.5%	0.25	1.29
MC (opt)	0.02	0.1	6.9%	93.1%	0.31	1.99

Table 4.9: Failure rate, γ_{mean} and $\gamma_{1\%}$ values for different MCuncertainty (unc) and MCerror dosethreshold (err) values when using Target 2.

Type	unc	err	$\gamma \geq 1$ (fail)	$\gamma \leq 1$ (pass)	γ_{mean}	$\gamma_{1\%}$
MC (dose)	0.05	0.6	4.6%	95.4%	0.28	1.52
MC (opt)	0.05	0.6	4.7%	95.3%	0.28	1.45
MC (dose)	0.05	0.1	4.4%	95.6%	0.28	1.43
MC (opt)	0.05	0.1	5.1%	94.9%	0.29	1.80
MC (dose)	0.04	0.6	4.5%	95.5%	0.28	1.46
MC (opt)	0.04	0.6	5.4%	94.6%	0.30	1.74
MC (dose)	0.04	0.1	4.3%	95.7%	0.27	1.44
MC (opt)	0.04	0.1	5.6%	94.4%	0.29	1.95
MC (dose)	0.03	0.6	4.4%	95.6%	0.27	1.44
MC (opt)	0.03	0.6	5.2%	94.8%	0.29	1.78
MC (dose)	0.03	0.1	4.0%	96.0%	0.27	1.40
MC (opt)	0.03	0.1	5.0%	95.0%	0.28	1.74
MC (dose)	0.02	0.6	3.9%	96.1%	0.27	1.37
MC (opt)	0.02	0.6	4.7%	95.3%	0.27	1.66
MC (dose)	0.02	0.1	3.8%	96.2%	0.27	1.40
MC (opt)	0.02	0.1	6.1%	93.9%	0.30	1.89

Table 4.10: Failure rate, γ_{mean} and $\gamma_{1\%}$ values for different MCuncertainty (unc) and MCerror dosethreshold (err) values when using Target 3.

The MC dose calculation of the treatment plans for the Targets 1, 2 and 3 located behind the chess pattern structure had a lower γ -index failure rate than for the Chess Target located within the chess pattern structure. Considering the whole treatment plan, the mean failure rate was 1.7% (gantry angle of 0°) and 1.4% (gantry angle of 15°) when using the target located within the chess pattern structure (Chess Target), whereas the failure rate dropped to 0.4% for all three targets located behind the chess pattern structure. For the reduced area, the mean failure rate was 14.4% (gantry angle 0°) and 13.3% (gantry angle 15°) when using the Chess Target, whereas the mean failure rate dropped to 4.3% for Target 1, 3.7% for Target 2 and 4.2% for Target 3.

Furthermore, an improvement of the γ -index analysis parameters for the recalculated treatment plans could be observed when more accurate MC parameters were used.

As previously observed, the percentage of voxels with $\gamma \geq 1$ (failure rate) was larger for the optimized treatment plans than for the recalculated treatment plans. For Target 1 the difference between the optimized and the recalculated treatment plans was between $\Delta_{min}(\gamma \geq 1)=2.1\%$ (unc=0.02, err=0.6) and $\Delta_{max}(\gamma \geq 1)=3.8\%$ (unc=0.04, err=0.6), for Target 2 between $\Delta_{min}(\gamma \geq 1)=3.1\%$ (unc=0.05, err=0.6) and $\Delta_{max}(\gamma \geq 1)=3.5\%$ (unc=0.02, err=0.6) and for Target 3 between $\Delta_{min}(\gamma \geq 1)=0.1\%$ (unc=0.05, err=0.6) and $\Delta_{max}(\gamma \geq 1)=2.3\%$ (unc=0.02, err=0.1).

4.2 Assessment of the user interface parameters

For the assessment of the user interface parameters the following MC parameters were chosen: $unc=0.05$ and $err=0.6$. This was done on basis of the short dose calculation times that could be achieved when using these parameters. Furthermore, the maximum number of particles was set to 500,000. Treatment plans for all three targets namely the small target with the dimensions of $20 \times 20 \times 20 \text{ mm}^3$ (8 cm^3), the midsized target with the dimensions of $40 \times 40 \times 40 \text{ mm}^3$ (64 cm^3) and the large target with the dimensions of $80 \times 80 \times 80 \text{ mm}^3$ (512 cm^3) were calculated. The beam incidence angle was set perpendicular to the target surface, namely 0° .

4.2.1 Evaluation of the peak width multiplier

The PWM describes the spacing between range/energy-layers. The PWM value multiplied by the last peak width produces the spacing of the different range layers. For the evaluation of the peak width multiplier (PWM), a fixed spot spacing of 0.5 cm was chosen and the PWM was varied from 0.4 to 1.8 in steps of 0.1 . To compare the dose distributions of different plans calculated with varying PWM values, dose profiles and depth-dose profiles were recorded. Both dose profiles and depth-dose profiles were recorded centrally in relation to the different targets.

The change of the dose homogeneity of the target is illustrated as a function of increasing distance between spot layers, as shown in Figure 4.10. The curve progressions of the midsized and large target looked similar to that of the small target and are therefore not shown.

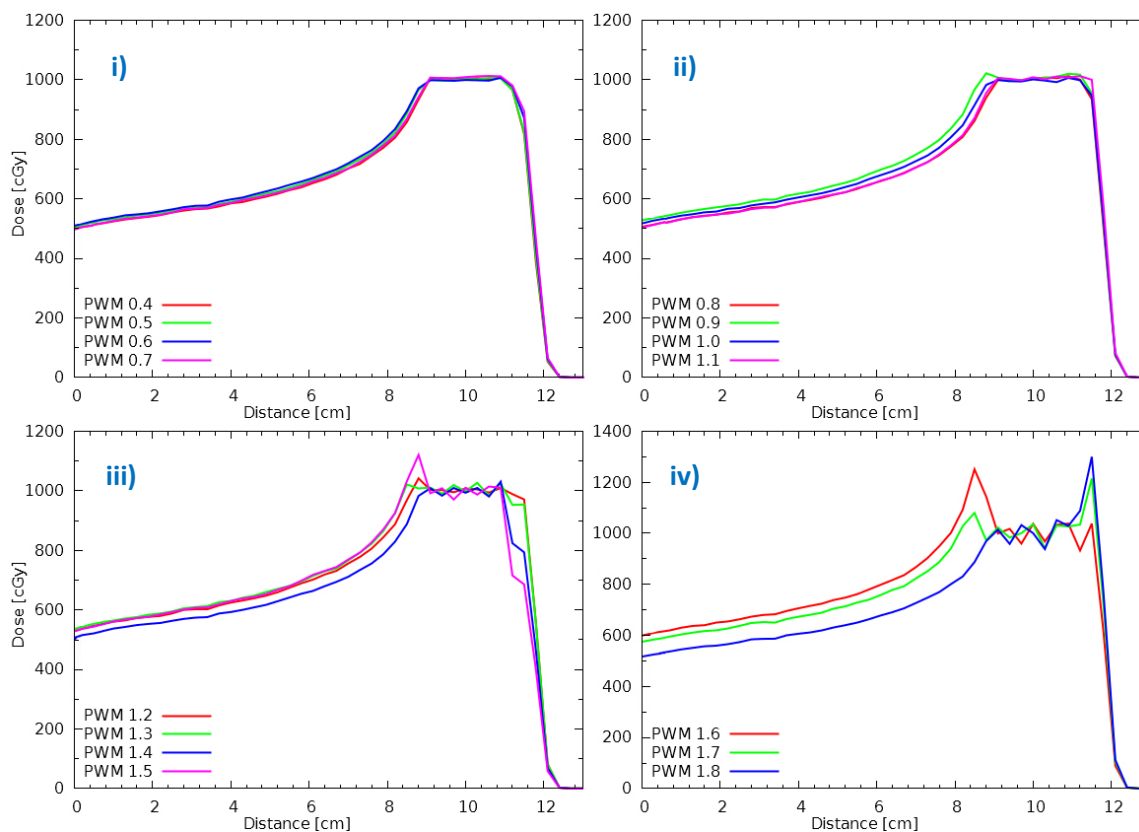


Figure 4.10: Comparison of the depth-dose profiles of the small target using different PWM values i) PWM 0.4-0.7, ii) PWM 0.8-1.1, iii) PWM 1.2-1.5 and iv) PWM 1.6-1.8.

For PWM values between 0.4-1.1 the curve progressions of the depth-dose profiles were similar. Figure 4.10 i) and Figure 4.10 ii) indicate good dose coverage based on the relatively smooth curve progression. Starting with a PWM value of 1.1, the dose coverage at the edge of the target got worse. Figure 4.10 iii) and Figure 4.10 iv) indicate that the spots, located proximal to the target, received a dose equal or higher than the target dose in order to obtain adequate dose coverage at the edge of the target. If high PWM values were used, a large dose weight was assigned to such spots that were located alongside the target. This resulted in a periodic fluctuation of the target dose conformity for all spots located proximally to the target, as shown in Figure 4.11.

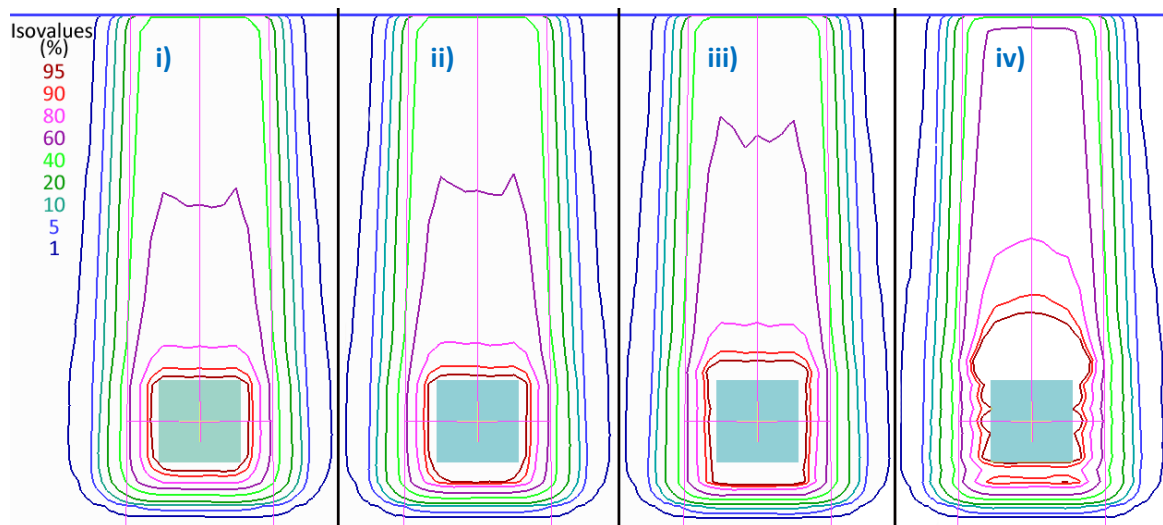


Figure 4.11: Dose distributions of the small target. i) PWM 0.4, ii) PWM 0.8, iii) PWM 1.2 and iv) PWM 1.6

Figure 4.12 shows different dose profiles generated of treatment plans with varying PWM values for the small target. The profiles for the mid-sized and large target were analogue to the small target and are therefore not shown.

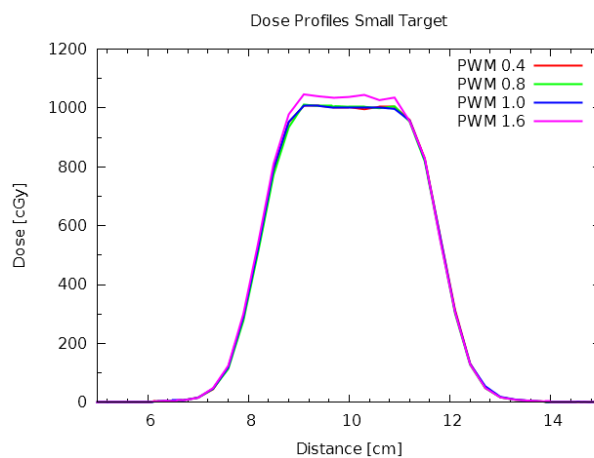


Figure 4.12: Comparison of the dose profiles of the small target calculated with different PWM values.

Table 4.11 shows dose calculation times, HI and CI for different PWM values for the small target. The dose calculation time decreased with an increase of the PWM, as consequence of the increased spacing between the layers. The number of layers varied between 16 (PWM of 0.4) and 6 (PWM of 1.8) for the small target, 27 (PWM of 0.4) and 8 (PWM of 1.8) for the midsized target and 49 (PWM of 0.4) and 11 (PWM of 1.8) for the large target.

PWM	Small target			Midsized target			Large target		
	D.C.T. [s]	HI	CI	D.C.T. [s]	HI	CI	D.C.T. [s]	HI	CI
0.4	84	0.033	0.782	303	0.038	0.861	1583	0.017	0.884
0.5	73	0.029	0.730	247	0.036	0.862	1321	0.017	0.881
0.6	63	0.030	0.726	209	0.042	0.850	1076	0.017	0.882
0.7	53	0.034	0.762	189	0.039	0.820	924	0.015	0.885
0.8	48	0.034	0.726	161	0.040	0.799	819	0.016	0.878
0.85	47	0.033	0.686	158	0.039	0.801	748	0.019	0.890
0.9	47	0.031	0.609	143	0.040	0.827	715	0.018	0.887
1.0	42	0.029	0.643	132	0.040	0.801	653	0.020	0.891
1.1	37	0.032	0.662	120	0.041	0.788	596	0.022	0.902
1.2	38	0.038	0.592	116	0.044	0.712	560	0.024	0.895
1.3	37	0.052	0.602	107	0.050	0.724	500	0.035	0.912
1.4	32	0.065	0.773	106	0.058	0.786	463	0.038	0.863
1.5	32	0.073	0.572	98	0.073	0.759	425	0.047	0.855
1.6	31	0.081	0.491	97	0.084	0.797	393	0.059	0.861
1.7	31	0.094	0.491	90	0.108	0.653	385	0.068	0.833
1.8	31	0.113	0.526	88	0.105	0.600	370	0.076	0.832

Table 4.11: Dose calculation times (D.C.T.) and dosimetric evaluation parameters for different PWM values of the small, midsized and large target.

The best results for HI and CI values could be achieved with low PWM values, as the accuracy of the dose calculation increased. Because the dose calculation time increased by a factor of two when changing the PWM from 0.4 to 0.8, small PWM values are not suitable for an adequate clinical use. Furthermore, a smaller PWM results in a higher number of energy layers and consequently in a longer treatment time. For an illustrative comparison of all three targets, the homogeneity index was plotted against the PWM and is shown in Figure 4.13.

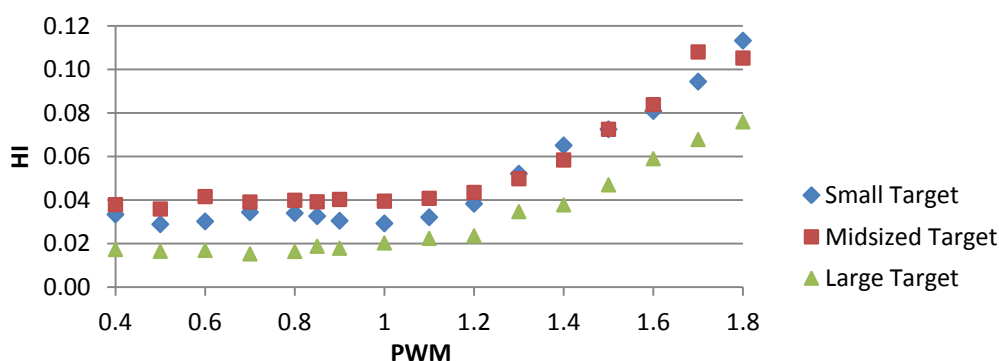


Figure 4.13: Dose homogeneity of all three targets with respect to changes of the PWM.

The better HI values of the large target can be explained by the size and spacing of the spots in relation to the target size. The impact of not perfectly covered corner edges of the target is comparatively larger for the small target than for the large target. This influences the HI values directly. Anyhow this effect will not be observed in a clinical situation as tumor structures are irregularly shaped and do not include any sharp edges as in this theoretical challenging setup.

Figure 4.14 shows the conformity index plotted against the PWM.

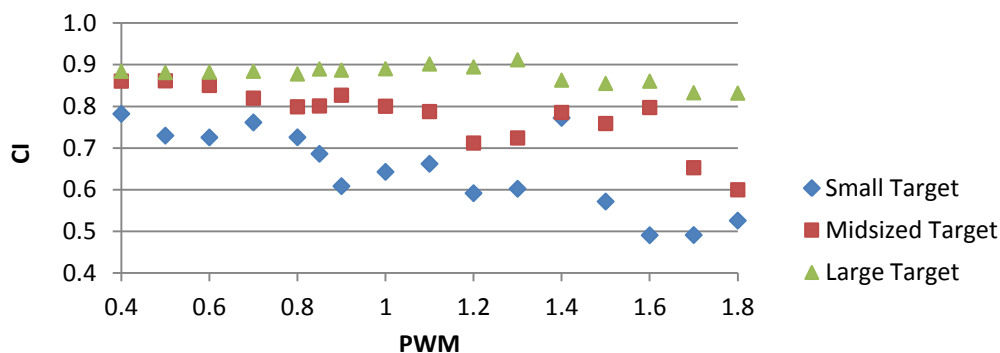


Figure 4.14: Dose conformity of all three targets with respect to changes of the PWM.

On the basis of depth-dose profiles and homogeneity- and conformity measurements the number of suitable PWM values could be reduced. Peak width multiplier values larger than 1.0 caused fluctuations of the target dose conformity and the accuracy of the dose calculation decreased with an increase of the distance between the spot layers.

Since no major changes of the homogeneity- and conformity index for different parameter settings was observed for the values of interest (PWM 0.6 - PWM 1.0), the dose calculation time was selected as decision criterion. In the end PWM values of 0.7 or 0.8 were chosen on the basis of adequate dose conformity and homogeneity and the shorter dose calculation time. Therefore, these parameter values were selected for the evaluation of the spot spacing.

4.2.2 Evaluation of the spot spacing

The spot spacing describes the distance between the centers of the spots defined at the isocenter. For the assessment of the spot spacing, PWM values of 0.7 and 0.8 were chosen. The spot spacing was varied between 0.3 cm and 0.6 cm in 0.1 cm steps. This range was selected according to Hillbrand et al. [61]. The conclusion of this paper was that a spot spacing of less or equal than two times the fixed spot sigma size (0.3 cm) appears to be adequate for IMPT treatment planning. When the spot spacing exceeded this limit, target dose conformity of the investigated treatment plans became worse.

For the comparison of dose distributions of different treatment plans calculated with varying spot spacing values, dose profiles and depth-dose profiles were evaluated. Both dose profiles and depth-dose profiles were recorded centrally in relation to the different targets. They are not shown here, as the curve progression of the curves with different spot spacing was nearly identical.

PWM	Small target				Midsized target			Large target		
	S.S. [cm]	D.C.T. [s]	HI	CI	D.C.T. [s]	HI	CI	D.C.T. [s]	HI	CI
0.7	0.3	95	0.063	0.833	434	0.051	0.847	2287	0.012	0.915
	0.4	62	0.056	0.815	258	0.050	0.845	1462	0.013	0.876
	0.5	54	0.034	0.767	189	0.039	0.820	924	0.015	0.883
	0.6	42	0.051	0.753	132	0.049	0.834	661	0.021	0.878
0.8	0.3	86	0.064	0.810	389	0.052	0.818	2014	0.013	0.911
	0.4	55	0.055	0.789	224	0.050	0.817	1296	0.015	0.871
	0.5	49	0.034	0.727	161	0.037	0.790	819	0.017	0.879
	0.6	37	0.053	0.715	119	0.050	0.807	584	0.022	0.875

Table 4.12: Dose calculation times (D.C.T.) and dosimetric evaluation parameters for different spot spacing (S.S.) values of the small, midsized and large target.

With decreasing spot spacing, the total number of spots increased and thus the dose calculation time increased as well. For illustrative purposes for all three targets the spot spacing was plotted against the HI, as shown in Figure 4.15 for fixed PWM values of 0.7 and 0.8.

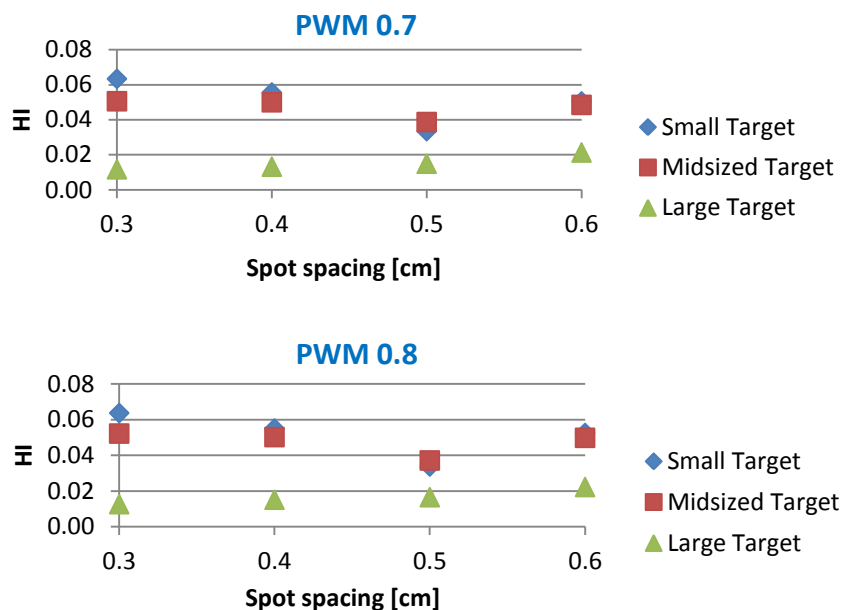


Figure 4.15: Dose homogeneity of all three targets with a fixed PWM of 0.7 and 0.8 with respect to changes of the spot spacing.

Figure 4.15 shows that the best homogeneity index values could be obtained with a spot spacing of 0.5 for the small and midsized target. Furthermore, Figure 4.15 and Table 4.12 indicate that the quality of a treatment plan created with a PWM value of 0.7 and 0.8 is equal. Only a dose calculation time increase of nearly 10% could be observed when using a PWM value of 0.7 instead of 0.8. In the end a spot spacing value of 0.5 cm and a peak width multiplier value of 0.8 were chosen, as these values were already recommended to be the optimal choice for PB dose calculation [61].

4.3 Patient examples

To assess the potential advantage and applicability of MC dose calculation for clinical routine, treatment plans were created for selected indications using MC and PB based dose calculation. A patient with prostate cancer and a patient with paranasal sinus cancer were chosen in order to evaluate the previously assessed MC and user interface parameters in clinical routine. A dose calculation grid size of $3 \times 3 \times 3 \text{ mm}^3$ was used for both clinical cases. A grid size of $2 \times 2 \times 2 \text{ mm}^3$ was not possible due to limited memory capacity of the hardware.

4.3.1 Prostate patient

For a first evaluation of the influence of MC settings on the dose distribution, a simple beam arrangement using one beam with an angle of 90° was chosen, as shown in Figure 4.16. The user interface parameters were set to a peak width multiplier of 0.8 and a spot spacing of 0.5 cm according to chapter 4.2.2. To achieve the prescription of 78 Gy to the target, the maximum dose was set to 7820 cGy and the minimum dose on 7780 cGy.

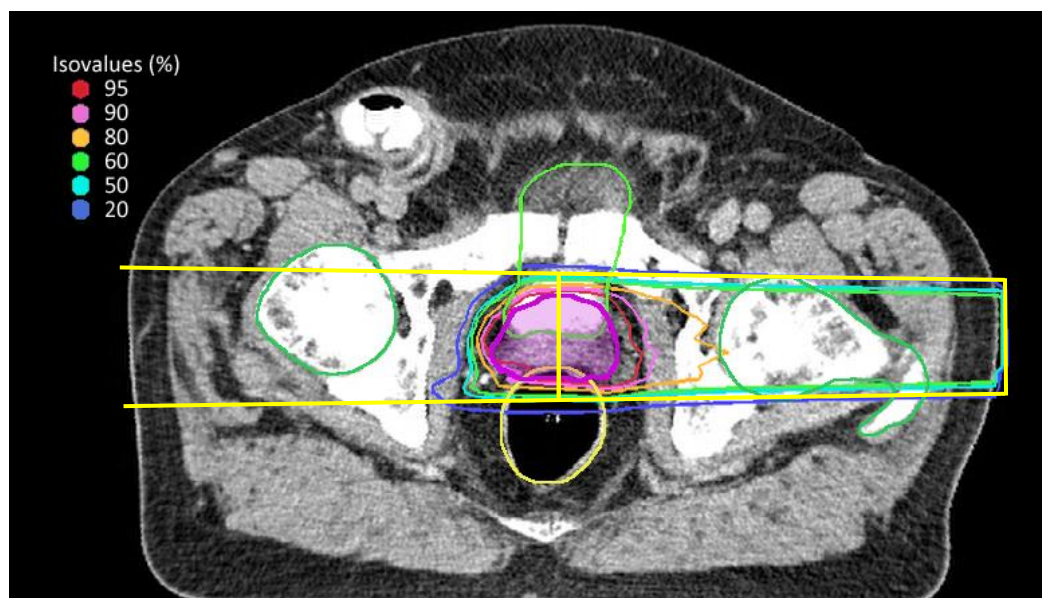


Figure 4.16: Isodose distribution of the prostate patient (one beam) calculated with the MC algorithm (unc=0.05, err=0.6) with the PTV and OARs.

First, the dose distribution was calculated using the PB algorithm and then optimized two times - because the first optimization was finished after only a few iterations - with the above mentioned constraints for the PTV. For this investigation, no constraints were set for the OARs in order to reduce influences of the optimization process on the dose distribution. For plan calculation and optimization the maximum number of iterations was set to 300 and the optimization convergence criterion was set to 0.001%. In a second step the optimized PB treatment plan was recalculated (“dose”) using the MC algorithm. As mentioned earlier in chapter 4.1.3, the MC parameter settings of a MCuncertainty of unc=0.03 and a MCerror dosethreshold of err=0.1 and unc=0.05, err=0.6 were considered for the prostate patient. The results of the dose evaluation are shown in Table 4.13.

Type	unc	err	D.C.T. [s]	HI	CI	$D_{2\%}$	$D_{98\%}$	$V_{95\%}$
PB (opt)	-	-	16	0.023	0.680	100.8	98.5	100.0
MC (dose)	0.05	0.6	142	0.107	0.619	103.1	92.3	96.0
MC (dose)	0.03	0.1	659	0.105	0.619	102.8	92.3	96.0

Table 4.13: Dose calculation times (D.C.T.) and dosimetric evaluation parameters of the prostate patient treatment plans (one beam) calculated with the MC and PB algorithm.

The HI increased from 0.02 for the optimized PB algorithm to 0.1 for the recalculated MC algorithm. The main factor for this increase is the lower dose calculated with the MC algorithm to 98% of the volume ($D_{98\%}$) in comparison to that of the PB algorithm, which influences the HI directly (chapter 2.13.4). The CI dropped from 0.68 for the PB plan to 0.62 for the MC plans (i.e. by 8.8%). Figure 4.17 shows a dose-difference map of the prostate patient.

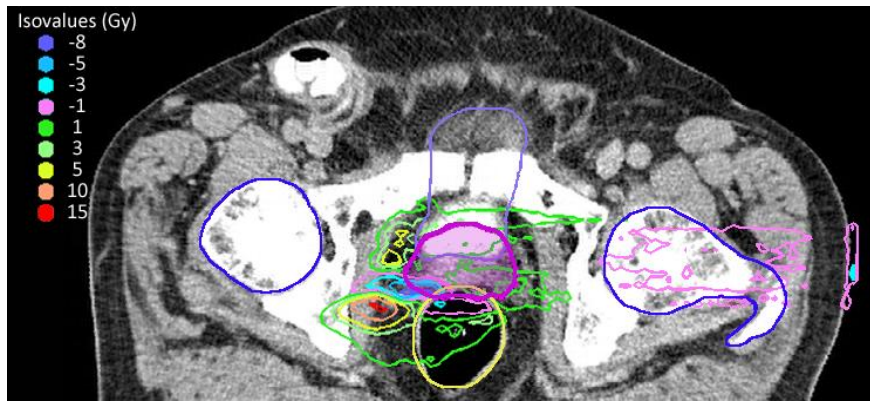


Figure 4.17: Dose-difference map of the prostate patient (one beam). The optimized PB plan was subtracted from the recalculated MC (unc=0.05, err=0.6) plan.

In Figure 4.17 the dose distribution of the optimized PB treatment plan was subtracted from the recalculated MC treatment plan, revealing a hotspot located proximal to the left bottom of the PTV, where a dose difference of more than 15 Gy (19% of the prescribed dose) could be observed. This high dose delivered by the MC algorithm can be explained on the basis of the different dose deposition characteristics of the MC and the PB algorithm in presence of tissue heterogeneities surrounding the PTV. As previously observed (chapter 4.1), the MC algorithm deposited more dose to areas located behind low density tissue (air filled rectal balloon).

Table 4.14 shows the results of the γ -index analysis (2%/2mm) of the whole treatment plan and for an area consisting of a 3D margin of 50 mm around the target, as shown in Figure 4.18. This area encompassed the nearby surroundings of the PTV, where large dose differences could be found, as shown in Figure 4.17.

	Type	unc	err	$\gamma \geq 1$ (fail)	$\gamma \leq 1$ (pass)	γ_{mean}	$\gamma_{1\%}$
Treatment plan	MC (dose)	0.05	0.6	0.4%	99.6%	0.02	0.62
	MC (dose)	0.03	0.1	0.3%	99.7%	0.02	0.60
Reduced area	MC (dose)	0.05	0.6	5.5%	94.5%	0.19	2.31
	MC (dose)	0.03	0.1	5.1%	94.9%	0.18	2.27

Table 4.14: Failure rate, γ_{mean} and $\gamma_{1\%}$ values of the prostate patient treatment plans using one beam. The dose calculated with the PB algorithm served as reference dose.

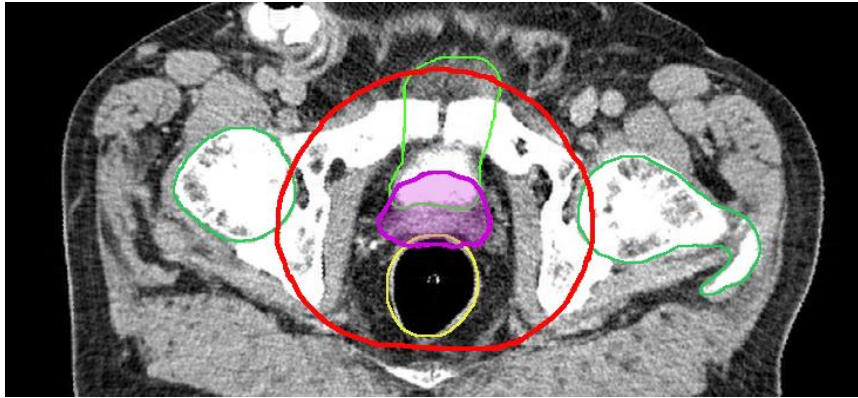


Figure 4.18: 3D margin (red circle) of 50 mm around the PTV.

A γ -index analysis revealed a failure rate of 0.38% (unc=0.05, err=0.6) when the whole treatment plan was reviewed. For the reduced area of 50 mm around the PTV, the failure rate increased to 5.54% (unc=0.05, err=0.6). Using the MC parameter settings of unc=0.05, err=0.6, γ_{mean} was 0.02 for the whole treatment plan and increased to 0.19 for the reduced area and $\gamma_{1\%}$ was 0.6 and increased to 2.3, respectively. Almost no difference could be observed when using different MC parameter settings.

In a second investigation, the dose was delivered by two opposing beams with a gantry angle of 90° and 270° (Figure 4.19), a commonly used setup for prostate treatment plans using protons. The treatment plan was calculated using the PB algorithm, then recalculated using the MC algorithm (“dose”) and then optimized (“opt”). To produce the PB treatment plan, the PTV was optimized two times with a dose prescription of 78 Gy. After this optimization, the constraints for the OARs were set and the plan was optimized accordingly.

After calculating the dose distribution using the selected MC parameters (unc=0.05, err=0.6 and unc=0.03, err=0.1), it was apparent that the dose calculation time with 404 s (unc=0.03, err=0.1) was short and therefore further measurements were carried out. Thus, the MCuncertainty was varied from 0.1 to 0.01 in different step sizes and the MCerrordosethreshold was changed from 0.6 to 0.1.

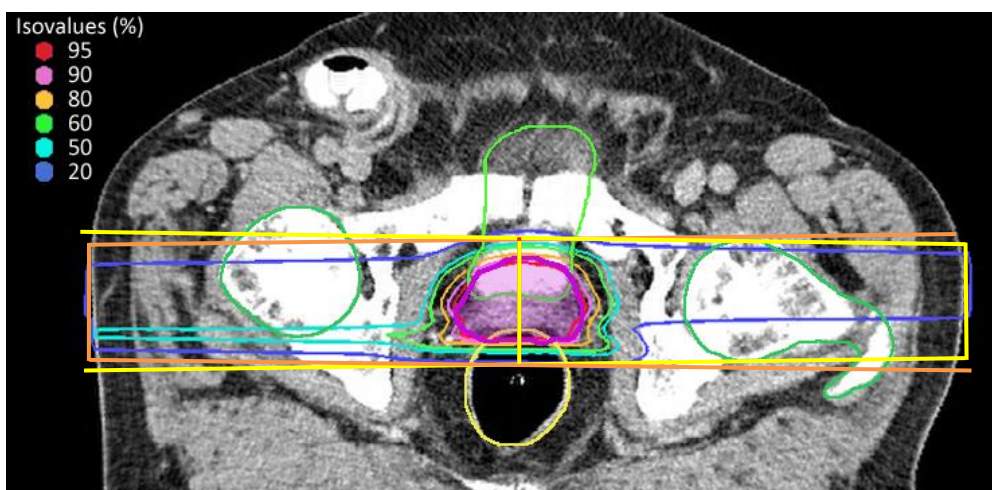


Figure 4.19: Isodose distribution of the prostate patient (two beams) calculated with the MC algorithm (unc=0.05, err=0.6) with the PTV and OARs.

Table 4.15 summarizes the dose calculation time, homogeneity- and conformity index values and dose-volume specifications of the prostate patient using two opposing beams.

Type	unc	err	D.C.T. [s]	HI	CI	$D_{2\%}$	$D_{98\%}$	$V_{95\%}$
PB (opt)	-	-	21	0.092	0.890	102.1	92.9	102.1
MC (dose)	0.1	0.6	38	0.127	0.838	104.3	91.8	104.3
MC (opt)	0.1	0.6	38	0.088	0.879	102.2	93.4	102.2
MC (dose)	0.08	0.6	42	0.126	0.837	104.6	91.9	104.6
MC (opt)	0.08	0.6	42	0.091	0.891	102.3	93.2	102.3
MC (dose)	0.05	0.6	80	0.124	0.834	104.2	91.7	104.2
MC (opt)	0.05	0.6	80	0.083	0.888	102.0	93.7	102.0
MC (dose)	0.05	0.1	156	0.122	0.835	104.2	91.9	104.2
MC (opt)	0.05	0.1	156	0.087	0.897	102.1	93.4	102.1
MC (dose)	0.03	0.6	207	0.121	0.834	104.0	91.8	104.0
MC (opt)	0.03	0.6	207	0.085	0.896	102.1	93.6	102.1
MC (dose)	0.03	0.1	404	0.120	0.836	103.9	91.9	103.9
MC (opt)	0.03	0.1	404	0.086	0.894	102.1	93.5	102.1
MC (dose)	0.02	0.6	455	0.120	0.836	104.0	91.9	104.0
MC (opt)	0.02	0.6	455	0.084	0.895	102.0	93.6	102.0
MC (dose)	0.02	0.1	896	0.120	0.838	104.0	91.9	104.0
MC (opt)	0.02	0.1	896	0.084	0.895	101.9	93.6	101.9
MC (dose)	0.01	0.6	1650	0.120	0.836	104.0	91.9	104.0
MC (opt)	0.01	0.6	1650	0.085	0.894	102.0	93.5	102.0

Table 4.15: Dose calculation times (D.C.T.) and dosimetric evaluation parameters of the prostate patient treatment plans (two beams) calculated with the MC and PB algorithm.

MC parameters with less accuracy, e.g. unc=0.1 and err=0.6, were tested to determine whether this accuracy was sufficient to obtain comparable results to the PB algorithm in a reasonable time. For an illustrative comparison the HI was plotted against the MCuncertainty (Figure 4.20).

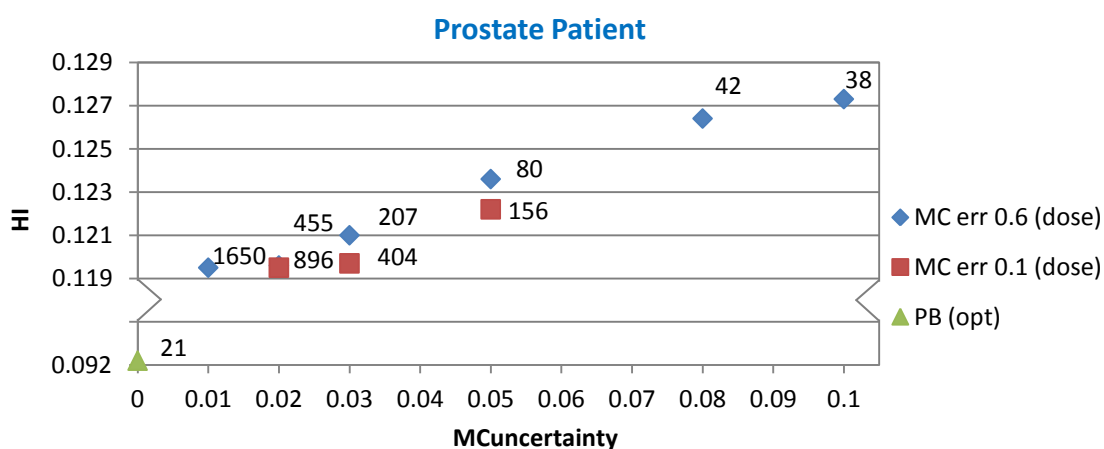


Figure 4.20: Dose homogeneity of the recalculated treatment plans of the prostate patient with respect to changes of MC parameters including dose calculation times [s] presented next to the data marker.

On the basis that lower HI values correspond to a more homogenous dose distribution within the target, the HI of the recalculated MC plans (0.12) decreased (by 33%) in comparison to the optimized PB treatment plan (0.09). Only minor variations in the HI values could be observed when using different MC parameter settings. When using the MC parameters of $unc=0.01$, $err=0.6$ instead of $unc=0.1$, $err=0.6$, an improvement in the HI of the recalculated MC plans of 6.1% could be observed and the dose calculation time increased by a factor of 43.

The previously assessed MC parameter settings (chapter 4.1) of $unc=0.05$, $err=0.6$ and $unc=0.03$, $err=0.1$ achieved adequate results, especially with respect to dose calculation time. Nevertheless, the MC dose calculations were about 4 ($unc=0.05$, $err=0.6$) and 20 ($unc=0.03$, $err=0.1$) times longer than the PB dose calculation.

The optimization process achieved an improvement, as the mean HI of the optimized MC treatment plans (0.086) dropped below the HI of the optimized PB treatment plan (0.09).

Considering the CI of the optimized PB plan (0.89), the mean CI of the recalculated MC treatment plans (0.84) decreased as well (by 5.6%), as an ideal treatment plan corresponds to a CI of 1. Optimization process achieved an improvement by 6.7%, as the mean CI of the recalculated treatment plans (0.84) increased to 0.89, which is comparable to the result of the PB treatment plan.

Figure 4.21 shows a cumulative DVH that compares the treatment plan calculated with the PB algorithm with the treatment plan calculated with the MC algorithm. A visible but not significant difference between the PB and MC treatment plans could be observed. Due to the small deviation between the various MC parameters and the similar curve progression, a DVH which compares different MC parameters is not shown here.

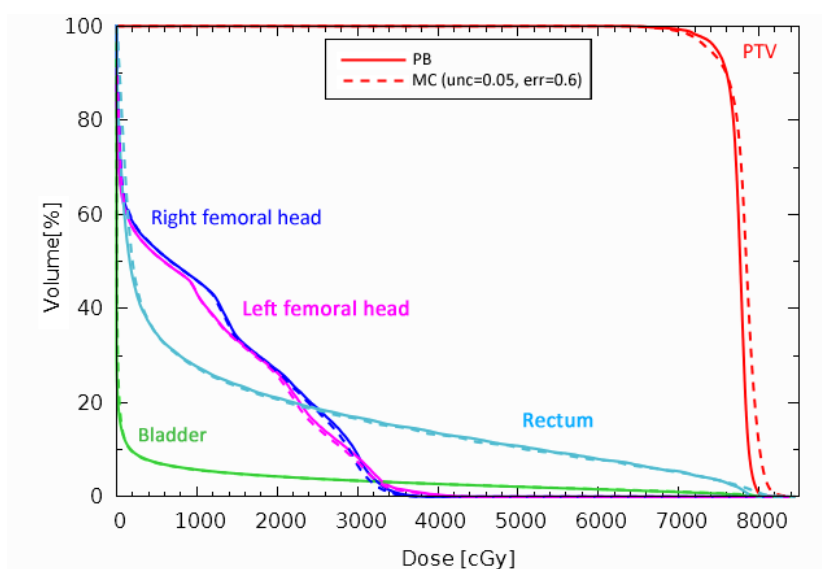


Figure 4.21: Cumulative DVH of the prostate patient (two beams) calculated with the MC ($unc=0.05$, $err=0.6$) and PB algorithm.

Figure 4.22 shows dose-difference maps of the prostate patient using two opposing beams. The optimized PB dose distribution was subtracted from the recalculated MC dose distribution (Figure 4.22 i)) and from the optimized MC dose distribution (Figure 4.22 ii)). The dose-difference maps reveal hotspots located proximal to the right and the left bottom of the PTV, where a dose difference of more than 15 Gy (19% of the prescribed dose) could be found. As previously observed, the MC algorithm deposited more dose in the area located behind the rectum due to the air filled rectal balloon. The PB algorithm, on the other hand, deposited more dose in the beam direction and the entrance region of the beam.

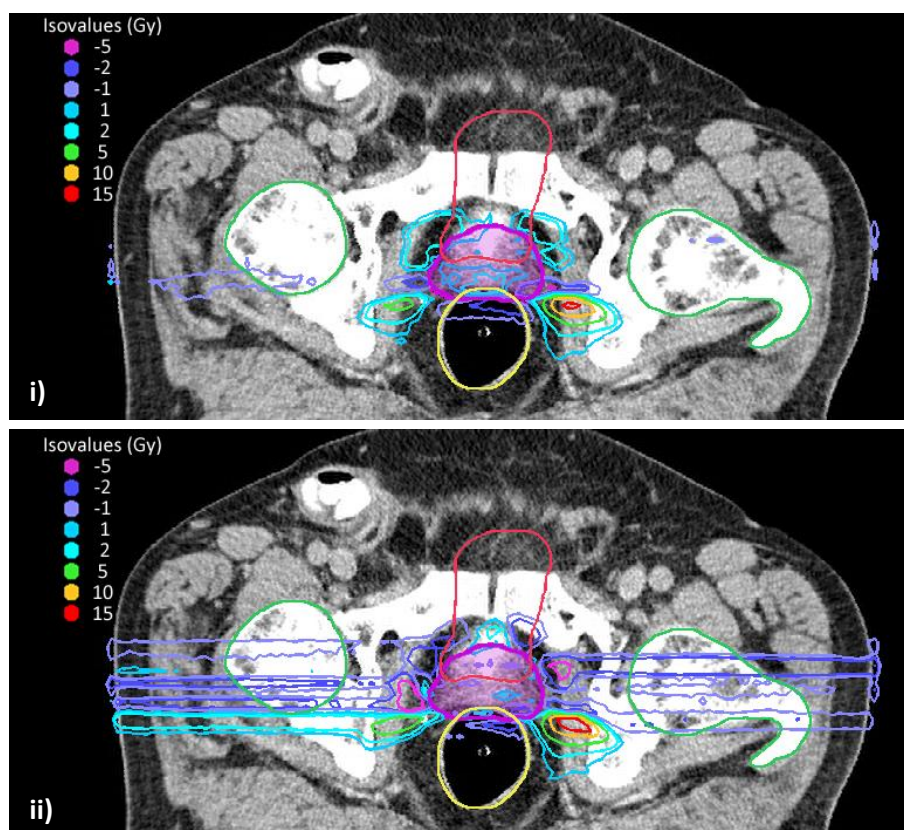


Figure 4.22: Dose-difference maps of the prostate patient (two beams) comparing MC plans with PB plans. The optimized PB plan was subtracted from the i) recalculated MC (unc=0.05, err=0.6) plan and the ii) optimized MC (unc=0.05, err=0.6) plan.

Figure 4.23 i) and Figure 4.23 ii) show dose-difference maps that compare recalculated MC treatment plans of the prostate patient calculated with different MC parameter settings. The dose-difference map depicted in Figure 4.23 i) shows dose differences of up to 2 Gy. The MC parameter settings used in this display represent the most accurate and least accurate MC parameter settings investigated.

In contrast, the dose-difference map in Figure 4.23 ii) shows only a dose difference up to 1 Gy.

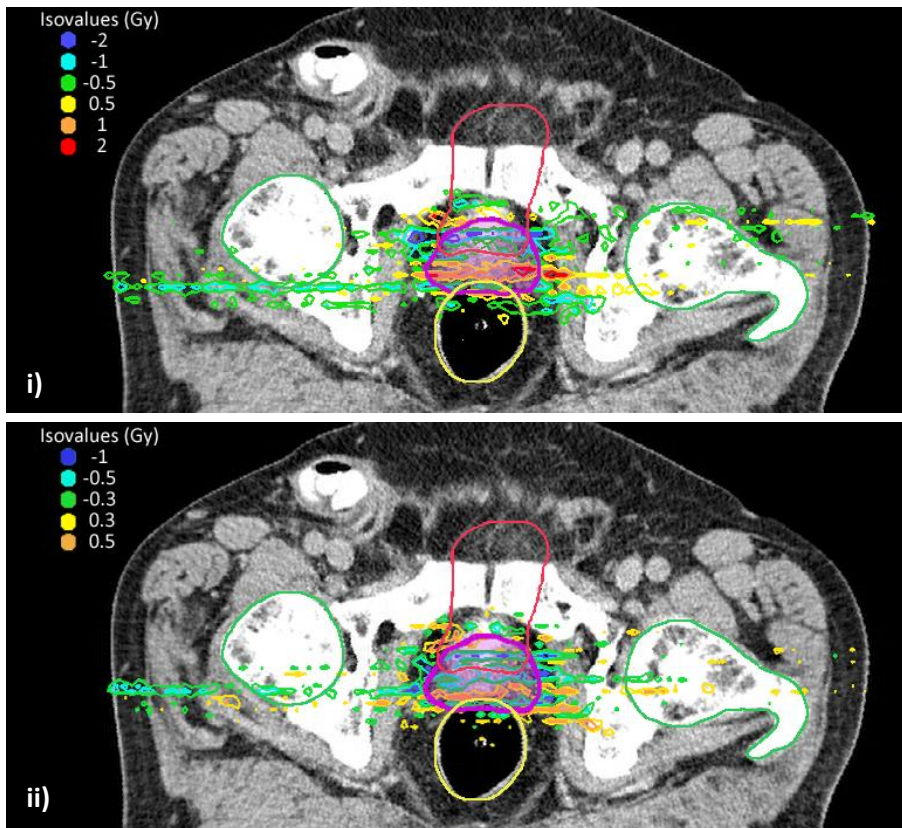


Figure 4.23: Dose-difference maps of the prostate patient (two beams) comparing MC plans with MC plans. Recalculated MC plans were compared using the MC parameters of i) (unc=0.1, err=0.6) - (unc=0.01, err=0.6) ii) (unc=0.5 err=0.6) - (unc=0.03, err=0.1).

The results of the γ -index analysis of the whole treatment plan are shown in Table 4.16.

Type	unc	err	$\gamma \geq 1$ (fail)	$\gamma \leq 1$ (pass)	γ_{mean}	$\gamma_{1\%}$
MC (dose)	0.1	0.6	0.4%	99.6%	0.02	0.55
MC (opt)	0.1	0.6	1.4%	98.6%	0.04	1.17
MC (dose)	0.08	0.6	0.4%	99.6%	0.02	0.52
MC (opt)	0.08	0.6	1.2%	98.8%	0.04	1.13
MC (dose)	0.05	0.6	0.3%	99.7%	0.02	0.48
MC (opt)	0.05	0.6	1.2%	98.8%	0.04	1.10
MC (dose)	0.05	0.1	0.3%	99.7%	0.02	0.47
MC (dose)	0.05	0.1	1.0%	99.0%	0.03	1.00
MC (dose)	0.03	0.6	0.3%	99.7%	0.02	0.46
MC (opt)	0.03	0.6	1.1%	98.9%	0.03	1.07
MC (dose)	0.03	0.1	0.3%	99.7%	0.02	0.47
MC (opt)	0.03	0.1	1.1%	98.9%	0.03	1.05
MC (dose)	0.02	0.6	0.3%	99.7%	0.02	0.47
MC (opt)	0.02	0.6	1.1%	98.9%	0.03	1.08
MC (dose)	0.02	0.1	0.3%	99.7%	0.02	0.46
MC (opt)	0.02	0.1	1.1%	98.9%	0.03	1.07
MC (dose)	0.01	0.6	0.3%	99.7%	0.02	0.46
MC (dose)	0.01	0.6	1.0%	99.0%	0.03	1.02

Table 4.16: Failure rate, γ_{mean} and $\gamma_{1\%}$ values of the prostate patient treatment plans (two beams). The dose calculated with the PB algorithm served as reference dose.

The highest failure rate ($\gamma \geq 1$) for the recalculated treatment plan was 0.4% the lowest 0.3%. γ_{mean} was 0.02 for all recalculated treatment plans and the highest $\gamma_{1\%}$ was 0.55 (unc=0.01, err=0.6). These results meet the suggested constraints (Table 2.2), described in chapter 2.13.7. Although the deviation between the different MC parameters was small, γ -index parameters improved for both the recalculated and the optimized treatment plan when more accurate MC parameter settings were used. Altogether, γ -index analysis of the whole treatment plan revealed that the MC algorithm was in good agreement with the PB algorithm and achieved comparable results.

Furthermore, γ -index analysis was done for the reduced area consisting of a 3D margin of 50 mm around the PTV (Figure 4.19), respective results are shown in Table 4.17. For the reduced area, the highest failure rate was 5.7% (unc=0.1, err=0.6); the lowest 5% (unc=0.01, err=0.6). The highest value obtained for γ_{mean} was 0.19 (unc=0.1, err=0.6) and 1.77 (unc=0.01, err=0.6) for $\gamma_{1\%}$. Although only the reduced area where the largest dose differences occurred was examined, only minor deviations between the different MC parameters could be observed.

The deviation of the failure rate between the most accurate MC parameters investigated (unc=0.01, err=0.6) and the least accurate MC parameters investigated (unc=0.1, err=0.6) was only 0.65% for the reduced area and only 0.05% for the whole treatment plan.

Type	unc	err	$\gamma \geq 1$ (fail)	$\gamma \leq 1$ (pass)	γ_{mean}	$\gamma_{1\%}$
MC (dose)	0.1	0.6	5.7%	94.3%	0.19	1.77
MC (opt)	0.1	0.6	10.8%	89.2%	0.29	2.71
MC (dose)	0.08	0.6	5.4%	94.6%	0.18	1.75
MC (opt)	0.08	0.6	9.8%	90.2%	0.28	2.70
MC (dose)	0.05	0.6	5.2%	94.8%	0.17	1.73
MC (opt)	0.05	0.6	9.5%	90.5%	0.27	2.86
MC (dose)	0.05	0.1	5.2%	94.8%	0.17	1.74
MC (dose)	0.05	0.1	8.1%	91.9%	0.24	2.63
MC (dose)	0.03	0.6	5.1%	94.9%	0.17	1.73
MC (opt)	0.03	0.6	8.8%	91.2%	0.25	2.63
MC (dose)	0.03	0.1	5.0%	95.0%	0.16	1.71
MC (opt)	0.03	0.1	8.6%	91.4%	0.25	2.73
MC (dose)	0.02	0.6	5.1%	94.9%	0.17	1.72
MC (opt)	0.02	0.6	9.0%	91.0%	0.25	2.79
MC (dose)	0.02	0.1	5.0%	95.0%	0.16	1.71
MC (opt)	0.02	0.1	8.7%	91.3%	0.25	2.77
MC (dose)	0.01	0.6	5.0%	95.0%	0.16	1.71
MC (dose)	0.01	0.6	8.5%	91.5%	0.24	2.69

Table 4.17: Failure rate, γ_{mean} and $\gamma_{1\%}$ values for the reduced area (two beams). The dose calculated with the PB algorithm served as reference dose.

Another type of investigation was carried out with the prostate patient. The aim was the assessment of some limitations of the MC algorithm concerning the target size. Therefore, the margin of the PTV was enhanced and the dose calculation time was recorded. For this setup the MC parameters were set to $unc=0.05$, $err=0.6$ due to the much shorter calculation time. Table 4.18 shows the dose calculation times for different target sizes.

Volume [cm ³]	D.C.T. [s]	Volume [cm ³]	D.C.T. [s]
68.85	80	1260.72	2297
200.85	364	1570.28	2912
426.02	740	1920.73	3582
770.73	1380	2776.42	5375
998.04	1819	3288.61	Dose calculation failed

Table 4.18: Dose calculation times (D.C.T.) of the prostate patient for different PTV sizes.

The treatment software XiO wasn't able to calculate the dose distribution within the prostate patient using the MC algorithm when the target volume was extended to a volume of 3288.61 cm³ and a grid size of 3x3x3 mm³ was used. The dose calculation might fail at an earlier point using a smaller volume, but due to the long dose calculation time no further investigation was done.

4.3.2 Paranasal sinus patient

The second patient investigated was a paranasal sinus (PS) patient, illustrated in Figure 4.24. The dose was delivered by three beams with gantry angles of 80°, 90° and 270° and couch angles of 300°, 355° and 345°, respectively. Similar to the prostate patient, the treatment plan was first calculated and optimized using the PB algorithm, then recalculated using the MC algorithm and then optimized in order to compare the results with those obtained using the PB algorithm. As before, the MC parameters of $unc=0.03$, $err=0.1$ and $unc=0.05$, $err=0.6$ were considered for the evaluation. The user interface parameters were set to a peak width multiplier (PWM) of 0.8 and a spot spacing of 0.5 cm. Due to the long dose calculation time only the treatment plans with these selected MC parameters were calculated. For plan calculation and optimization the maximum number of iteration was set to 300 and the optimization convergence criterion was set to 0.001%. To achieve the prescription of 70 Gy to the target, the maximum dose was set to 7010 cGy and the minimum dose on 6990 cGy. Similar to the prostate case, the PTV was optimized two times using the PB algorithm, explained in more detail in chapter 4.3.1. After the optimization process, the constraints for the OARs were set and the plan was optimized again to assure a reproducible treatment plan that is not influenced by the order of the optimization steps. The dose distribution was measured by means of homogeneity- and conformity measures and dose-volume specifications and the final decision was also based on the dose calculation time (Table 4.19).

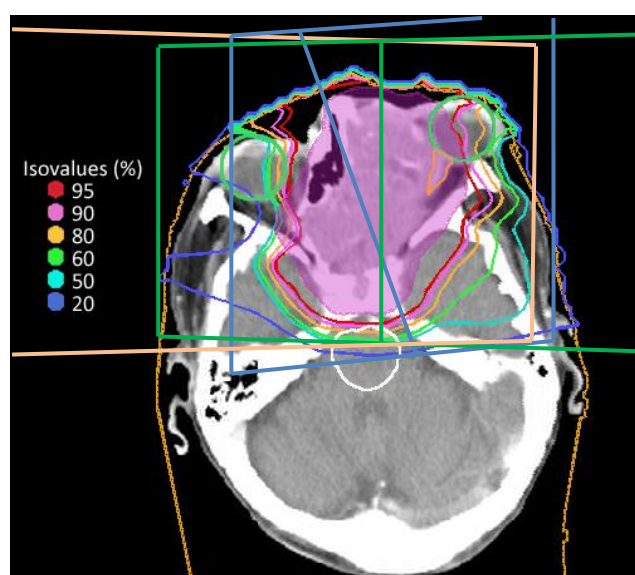


Figure 4.24: Isodose distribution of the paranasal sinus patient with the PTV and OARs.

Type	unc	err	D.C.T. [s]	HI	CI	$D_{2\%}$	$D_{98\%}$	$V_{95\%}$
PB	-	-	21	0.039	0.799	101.4	97.5	99.1
MC (dose)	0.05	0.6	789	0.083	0.764	103.2	94.9	97.9
MC (opt)	0.05	0.6	789	0.067	0.784	102.5	95.8	98.7
MC (dose)	0.03	0.1	3210	0.081	0.763	103.2	95.0	98.0
MC (opt)	0.03	0.1	3210	0.062	0.777	102.3	96.1	98.9

Table 4.19: Dose calculation times (D.C.T.) and dosimetric evaluation parameters of the PS patient calculated with PB and MC algorithm.

The homogeneity index increased from 0.04 (optimized PB plan) to 0.08 (recalculated MC plans) which corresponds to an increase by a factor of 2. In contrast, the HI of the prostate patient treatment plans increased only from 0.09 to 0.12, respectively, which corresponds to an increase by a factor of 1.3. The HI values obtained when using different MC parameter settings differed by 1.8% only. Optimization achieved an improvement of the target homogeneity, as the HI dropped from 0.08 to 0.06 for the MC treatment plans.

The conformity index of the optimized PB treatment plan (0.80) declined by 5% in comparison to the recalculated MC treatment plans (0.76). Optimization achieved an improvement in the plan conformity as well, as the CI of the recalculated MC plans increased from 0.76 to 0.78 for the optimized MC plans.

Dose calculation time took about 38 (unc=0.05, err=0.6) and 153 (unc=0.03, err=0.1) times longer when using the MC algorithm instead of the PB algorithm. The much longer dose calculation time as well as the negligible improvements of the dosimetric evaluation parameters (Table 4.19) resulting from the application of the more accurate MC parameters, show that the clinical setting for more complex clinical cases where many heterogeneities are involved, isn't practical. Therefore, the usage of a MCuncertainty of 0.05 seems acceptable, especially with respect to the much shorter dose calculation time.

Figure 4.25 shows cumulative DVHs of the paranasal sinus patient calculated with different dose calculation algorithms. Due to the small deviation between the various MC parameters and the similar curve progression, a DVH which compares different MC parameters is not shown here.

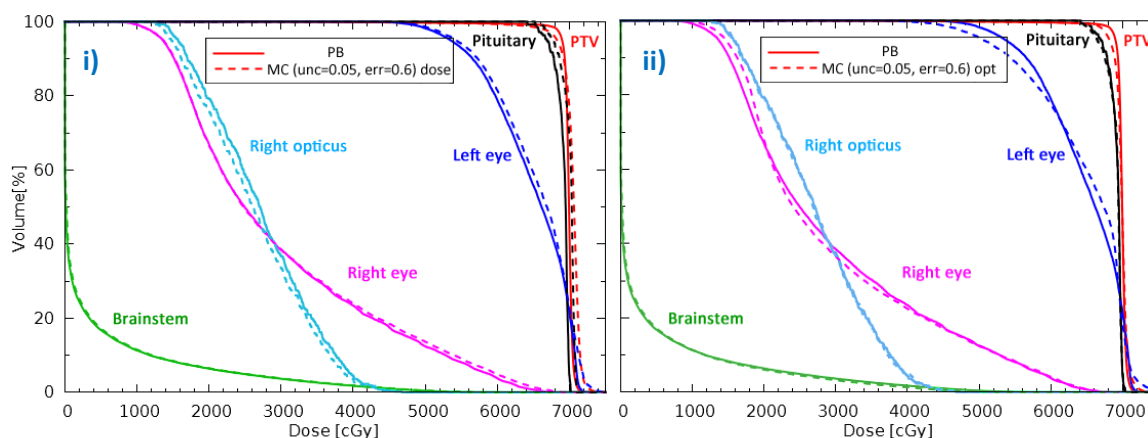


Figure 4.25: Cumulative DVHs of the PS patient calculated with the PB algorithm and i) the recalculated MC and ii) the optimized MC treatment plan (unc=0.05, err=0.6).

Figure 4.25 shows a visible, but not significant difference between the treatment plans calculated with the PB and the MC algorithm. The corresponding dose-difference maps are shown in Figure 4.26.

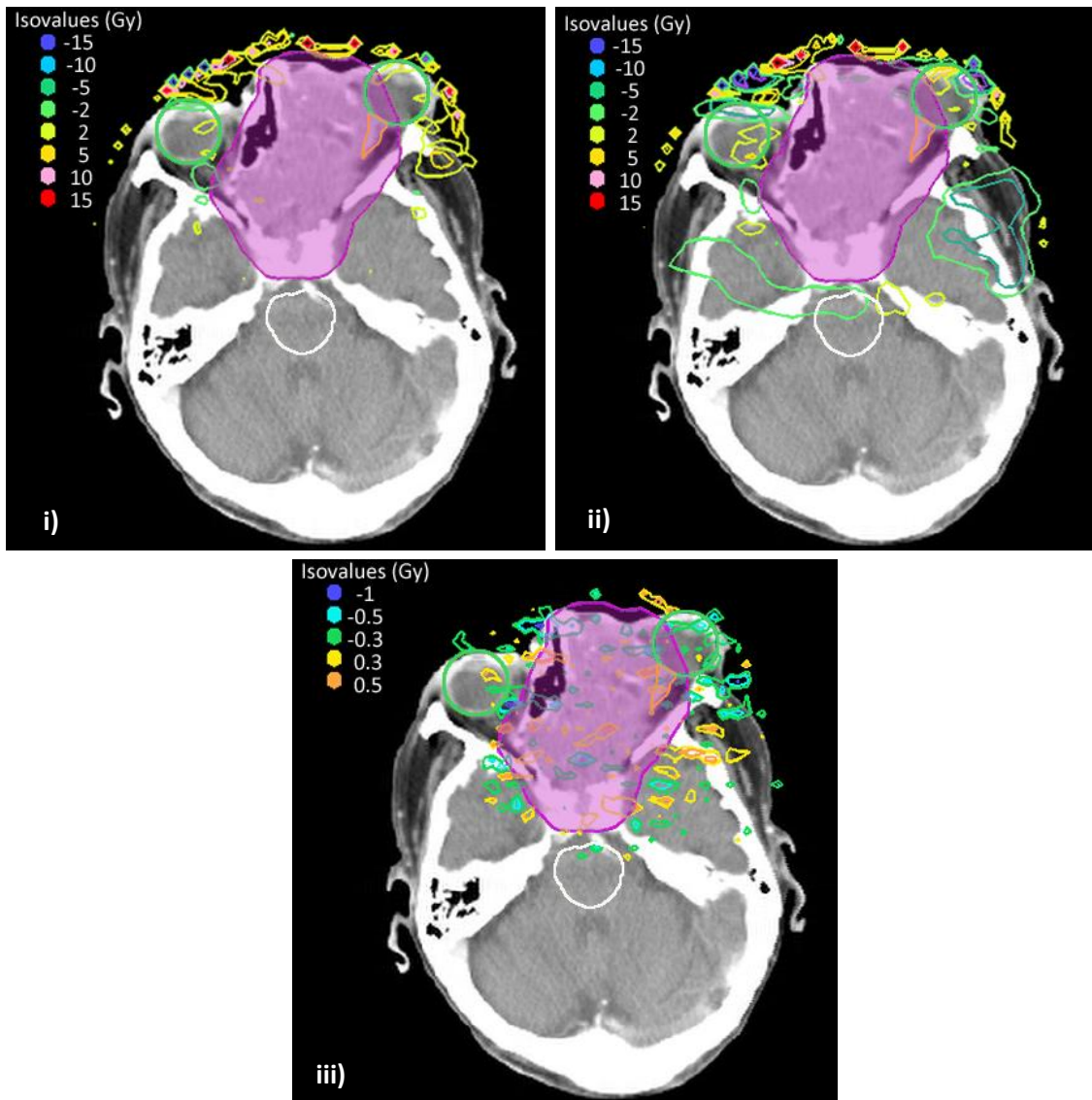


Figure 4.26: Dose difference maps of the PS patient. The optimized PB plan was subtracted from the i) recalculated MC (unc=0.05, err=0.6) plan and ii) the optimized MC (unc=0.05, err=0.6) plan. In image iii) a recalculated MC (unc=0.03, err=0.1) plan was subtracted from a recalculated MC (unc=0.05, err=0.6) plan.

Figure 4.26 i) and ii) show dose-difference maps that compare recalculated MC treatment plans of the paranasal sinus patient calculated with different MC parameter combinations. Small hotspots on the surface of the patient created by both the PB and the MC algorithm are visible. Materials like the plastic treatment mask, air cavities, soft tissue and bone tissue are the source of these hotspots. Hotspots having a dose difference of up to 15 Gy (21% of the prescribed dose) could be found. This dose difference is comparable to the dose difference of approximately 19% that could be observed in the dose-difference maps of the prostate patient (chapter 4.3.1). The small dose difference of approximately 1 Gy (Figure 4.26 iii)), which results from the usage of different MC parameter settings, is comparable to that of the prostate patient as well.

Table 4.20 shows the results of γ -index analysis (2%/2mm) of the paranasal sinus patient.

Type	unc	err	$\gamma \geq 1$ (fail)	$\gamma \leq 1$ (pass)	γ_{mean}	$\gamma_{1\%}$
MC (dose)	0.05	0.6	1.3%	98.7%	0.06	1.17
MC (opt)	0.05	0.6	4.3%	95.7%	0.12	2.43
MC (dose)	0.03	0.3	1.3%	98.7%	0.06	1.17
MC (opt)	0.01	0.1	4.3%	95.7%	0.12	2.46

Table 4.20: Failure rate, γ_{mean} and $\gamma_{1\%}$ values of the PS patient. The dose calculated with the PB algorithm served as reference dose.

γ -index analysis revealed a failure rate of 1.3% (unc=0.05, err=0.6), a γ_{mean} of 0.06 and a $\gamma_{1\%}$ of 1.17 for the recalculated and not optimized treatment plan. Although the results of the paranasal sinus patient are higher than the results of the prostate patient (failure rate of 0.4%, a γ_{mean} of 0.02 and $\gamma_{1\%}$ of 0.55), the result fulfill the suggested constraints (Table 2.2), described in chapter 2.13.7.

Furthermore Table 4.20 illustrates, that the deviation between different MC parameters is almost negligible and therefore a MCuncertainty of 0.05 is considered to be sufficient.

5. Summary and Discussion

The aim of this project was to benchmark the Monte Carlo (MC) algorithm (2.11.4) against the pencil beam (PB) algorithm (chapter 2.11.3) and the identification of clinical useful MC calculation settings (chapter 4.1) for dose calculation in proton therapy. The following parameters were considered: the mean relative statistical uncertainty per spot (1-5%, $unc=0.1-0.5$), the mean relative statistical uncertainty threshold (10%-60% of the maximum dose per spot, $err=0.1-0.6$) for voxels included in the uncertainty calculation and the maximum numbers of particles ($maxNr=5 \times 10^3-5 \times 10^5$). Furthermore, treatment planning parameters as e.g. peak width multiplier and spot spacing were examined (chapter 4.2).

Treatment planning systems for proton beam therapy are currently based on fast analytic dose calculation engines using PB algorithms. Nevertheless, there are limitations of PB algorithms concerning heterogeneous media, mainly because of the one-dimensional density scaling of particle beams in a medium. MC calculations, on the other hand, are recognized for their superior accuracy due to their more detailed consideration of physics processes, especially in difficult treatment situations involving media with large density and composition variations. This is particularly important when using protons for treatment due to the fact that inhomogeneities produce much larger dose perturbations in a proton treatment plan than in a photon treatment plan (chapter 2.4). While heterogeneities alter the dose distributions of a photon treatment plan only by a few per cent, their influence on charged particle beams can be enormous. Therefore, the evaluation of the value of MC based dose calculation in modern proton treatment planning systems is essential for further improvement in particle beam therapy.

For parameter assessment different phantom geometries were considered. Thereby, assessing the optimal phantom shape and composition is essential. Two phantoms with different geometry and HU compositions were created using MATLAB. For the evaluation of the MC parameters (chapter 3.3.3), a complex multi-layer chess pattern phantom (chapter 3.1.2) with different densities (HU of +1000 (bone) and -800 (lung)) embedded in a water tank was created with target structures placed within or at different distances behind the chess pattern. This phantom composition was chosen because differences between PB and MC algorithms should be particularly observable at boundary layers. For the assessment of an optimal user interface parameter set (chapter 3.3.4) a homogenous cubic phantom (chapter 3.1.3) was created with three cubes of different size that served as target structures [61].

For parameter assessment, treatment plans based on the PB algorithm were optimized and recalculated via the MC algorithm using a XiO research version v4.62 (Elekta AB, Stockholm, Sweden) (chapter 3.2.2). The outcome of the PB and the MC algorithm based treatment plans were compared using dose profiles, dose-difference maps, γ -index analysis and dosimetric parameters such as conformity index (CI) and homogeneity index (HI) (chapter 2.13). Furthermore, the dose calculation time that the XiO software required for calculating a 3D dose distribution within the phantom was evaluated for selecting a set of parameters. It should be

considered that the dose calculation time is strongly dependent on the available hardware and therefore the results can't be readily transferred to other investigations.

For the evaluation of the MC parameters a coarse estimation of the maximum number of particles that are considered in the MC calculation was done (chapter 4.1.1). To ensure that the numbers of particles didn't terminate dose calculation, 5×10^4 particles were required for uncertainty values of 0.05-0.03 and 5×10^5 below $\text{unc}=0.03$. For the target located in the chess pattern structure, different gantry angles between the beam entrance direction and target surface, namely 0° and 15° , were investigated (chapter 4.1.2). For both gantry angles the HI was 0.05 for the PB treatment plan and increased to 0.1 for the MC treatment plans with the tendency of a decreased HI for more accurate MC parameter settings. Considering the fact that the PB algorithm is based on several approximations and thus the accuracy of this method is limited under certain circumstances (e.g. density heterogeneities), it is debatable whether the obtained results reflect the reality. Every dose calculation algorithm has uncertainties that have their origin in e.g. approximations and simplifications of the physical model or in the computer implementation of the algorithm. When using the MC algorithm, uncertainties like the CT to material conversion uncertainty or the statistical uncertainty in the calculated dose (proportional to $1/\sqrt{n}$, where n is the number of particles simulated) have to be considered. Nevertheless, the results obtained with the MC algorithm are probably more realistic than the results obtained with the PB algorithm due to the more detailed consideration of physical processes. However, measurements would be necessary in order to evaluate which algorithm reflects the reality more accurately.

Furthermore, different dose deposition properties of the MC and PB algorithm in the presence of heterogeneities could be examined on the basis of dose-difference maps which showed that the MC algorithm deposited more dose to areas located proximal to low density tissue (in this case lung tissue).

For the targets located at 10 mm (Target 1), 20 mm (Target 2) and 30 mm (Target 3) behind the chess pattern structure, it could be observed, that the distance to the inhomogeneities influenced the difference between the MC and PB algorithm to a large extent. For 10 mm distance to the chess pattern structure, the CI was 0.84 for PB and 0.78 for MC, independent of the MC parameter settings; 0.83 for the PB and 0.78 for MC for 20 mm distance, whereas for 30 mm almost no difference between PB and MC could be observed. For both targets located within the chess pattern structure as well as for the targets located behind the chess pattern structure, γ -index analysis revealed that the PB and MC results were in good agreement.

For an appropriate use of the MC algorithm implemented in the XiO treatment planning system all parameters, including the user interface parameters (peak width multiplier (PWM) and spot spacing), had to be assessed. Thus, in a second step the user interface parameters were varied according to Hillbrand et al. [61] using the homogenous cubic water phantom. The peak width multiplier (chapter 4.2.1) and the spot spacing (chapter 4.2.2) were analyzed on basis of dose calculation time, dose profiles and HI and CI measures were used for evaluating the results. Since no major changes of the HI and CI values for different parameter settings could be

observed, the dose calculation time was selected as decision criterion. The results of the evaluation of the PWM and the spot spacing showed that there are limits for the interspaces between dose spots and layers in order to achieve clinically acceptable treatment plans. On the basis of adequate HI and CI values and dose calculation times, a PWM value of 0.7 or 0.8 was selected for the evaluation of the spot spacing.

During the evaluation of the spot spacing values, it could be observed that the best homogeneity and conformity of the treatment plan could be obtained with a spot spacing of 0.5 cm for all three target sizes. However, as nearly no difference was found between the PWM values of 0.7 and 0.8, a PWM of 0.8 and a spot spacing of 0.5 cm were recommended for further investigations. This was done on basis of shorter dose calculation time (10%) when using a PWM value of 0.8 instead of 0.7 and furthermore these values were already proven to be the optimal choice for PB dose calculation. It should be considered, that the evaluation of the user interface parameters were based on a perfectly homogeneous cubic phantom. Therefore, the limits for the spot spacing and the distance between spot layers (PWM) can't be readily transferred to clinical situations. Due to tissue heterogeneities, a higher number of spots can be necessary to compensate for air/tissue/muscle gaps, which can be achieved by a reduction of the spacing between spots.

To assess the usefulness and applicability of MC dose calculation for clinical routine, treatment plans were created for selected patients using MC and PB based dose calculation. The patient data sets included a patient with prostate cancer (chapter 4.3.1) and a patient with paranasal sinus cancer (chapter 4.3.2). In a first investigation of the prostate patient, the dose was applied by one beam. The HI increased from 0.02 for the optimized PB algorithm to 0.1 for the recalculated MC algorithm. Furthermore, dose-difference maps (Figure 4.17) revealed a hotspot located proximal to the left bottom of the PTV, where a dose difference of more than 15 Gy (19% of the prescribed dose) between the PB and MC treatment plans could be observed. This high dose delivered by the MC algorithm can be explained on the basis of the different dose deposition properties of the MC and the PB algorithm in presence of tissue heterogeneities surrounding the PTV. As previously observed the MC algorithm deposited more dose to areas located behind low density tissue (air filled rectal balloon). At this point it should be considered that CT images of patients that received photon radiation therapy were used in the framework of this thesis. Due to the higher dose perturbation at the air-tissue interface when using protons instead of photons, air filled rectal balloons are not used in proton radiation therapy and thus the results can't be transferred to clinical situations.

In a second investigation, the dose was delivered by two opposing beams. Dose-difference maps pointed out that the PB algorithm deposited more dose in the beam direction and the entrance region of the beam, whereas the MC algorithm deposited more dose in the area located around the PTV, creating hotspots of up to 19% of the prescribed dose (Figure 4.22). The HI increased from 0.09 for PB dose calculation to 0.12 for MC dose calculation, with decreasing tendency for more accurate MC parameter settings.

The investigation of the prostate patient showed, that even MC parameters of $unc=0.1$ and $err=0.6$ achieved similar results to the PB algorithm within a dose calculation time comparable to the PB dose calculation time.

The second patient examined was a paranasal sinus (PS) patient. Dose-difference maps of the PS patient that compared treatment plans calculated with the MC and the PB algorithm, showed small hotspots located on the surface of the patient (Figure 4.26). These hotspots were caused by different dose deposition characteristics of the MC and the PB algorithm in the presence of density and composition variations (plastic treatment mask, air cavities, soft tissue and bone tissue). A dose difference of up to 15 Gy (21% of the prescribed dose) could be observed.

The HI of the PS treatment plans increased from 0.04 for the PB dose calculation to 0.08 for the MC dose calculation, which corresponds to an increase by a factor of 2. In comparison, the HI of the prostate patient treatment plans increased by a factor of 5 (from 0.02 to 0.1) when using one beam and by a factor of 1.3 (from 0.09 to 0.12) when using two opposing beams. Considering the targets located within the Chessphantom, the HI of the recalculated MC plans increased by a factor of 2.3 (Chess Target, gantry angle of 0°), 1.9 (Chess Target, gantry angle of 15°), 1.2 (Target 1), 1.4 (Target 2) and 1.3 (Target 3) in comparison to the PB plans.

Both the results of the patient examples and the phantoms showed only minor variations in the HI and CI values when using different MC parameter settings. An improvement in the HI of the of 1.8% (PS patient), 2% (prostate patient, one beam), 3.2% (prostate patient, two beams), 4.2% (Chess Target, gantry angle 0°), 3.1 % (Chess Target, gantry angle 15°), 1.5% (Target 1), 6.9% (Target 2) and 3.6% (Target 3) could be observed when the MC parameter settings of $unc=0.03$, $err=0.1$ were used instead of $unc=0.05$, $err=0.6$. It is visible, that these differences resulting from the usage of different MC parameter settings vary with different setups. However, the difference was maximal 7%, whereas the dose calculation time increased significantly.

The dose calculation time for the MC treatment plans of the PS patient increased by a factor of 38 ($unc=0.05$, $err=0.6$) and a factor of 153 ($unc=0.03$, $err=0.1$) in comparison to the PB dose calculation. In contrast, the dose calculation time of the prostate patient increased by a factor of 9 and 41 (one beam) and a factor of 4 and 19 (two opposing beams) respectively. Furthermore, the dose calculation time of the Chessphantom using different targets increased by a factor of 9 and 61 (Chess Target, gantry angle of 0°), 10 and 68 (Chess Target, gantry angle of 15°), 22 and 87 (Target 1), 22 and 89 (Target 2) and 21 and 88 (Target 3) respectively. This longer dose calculation time resulting from using more accurate MC parameters showed that the clinical application for more complex clinical cases that involve heterogeneities is not practical.

The results of the PS and the prostate patient indicate, that an MCuncertainty of 0.05 seems acceptable for a clinical MC dose calculation, especially with regard to the dose calculation time. Furthermore, γ -index analysis and the comparison of the homogeneity and conformity measures showed that the deviation between different MC parameter was very small and therefore, the longer dose calculation time resulting from the usage of more accurate MC parameter might not be justified and practical in clinical use.

All results pointed out that the tested MC algorithm was well implemented in the XiO treatment planning software. However, it should be considered that the already for proton therapy clinically used PB algorithm worked accurate and achieved comparable results to the MC algorithm. This conclusion was also based on more complex treatment planning situations where heterogeneities were involved.

6. Outlook

Due to the high accuracy of MC dose calculation algorithms and the possibility to simulate all physical processes occurring during irradiation, it seems natural that MC methods may eventually become the gold standard for future radiation therapy treatment planning. On the basis of the dose deposition properties of protons, which are characterized by a steep rise and fall-off of the depth-dose distribution towards the end of the particle's range (Bragg peak), the high accuracy of MC dose calculation may be even more important in particle therapy than in conventional photon radiation therapy. The MC method decreases uncertainties in dose calculations, which is particularly important for particle therapy due to the finite range of the particles. The potential advantages of using MC dose calculation algorithms for particle therapy are particularly evident when the radiation field passes through tissue heterogeneities, such as bone tissue, lung tissue or air cavities. Especially air cavities pose a great challenge, as the dose perturbation created by air-tissue interface effects are difficult to estimate. In comparison to other analytical dose models, MC simulations are more suitable for complex clinical cases involving heterogeneities in the radiation field, as they provide a better evaluation of interface doses and in addition they are able to handle electron multiple scattering in the presence of heterogeneities with remarkable accuracy. One disadvantage when using MC algorithms for calculating the dose distribution is the long dose calculation time. Based on the fast developments in computer technology (cluster computing, massive parallel processing, grid computing), it is reasonable to expect that the Monte Carlo method will play a central role in the radiation therapy treatment planning of the future.

To guarantee a successful dose delivery, dosimetric verification of the MC algorithm implemented in the treatment planning system has to be considered for future projects. For the first investigation, a uniform and homogeneous water phantom could be irradiated. The delivered dose could be measured and compared to the dose calculated with the treatment planning system using the same homogeneous water phantom. In a second step, a heterogeneous phantom consisting of different materials equivalent to different body tissues should be investigated. CT scans of the phantom could be taken and treatment planning could be performed using the MC algorithm. Comparing the delivered dose distribution to the calculated dose distribution would ensure the successful dose delivery and enable accurate verification of the MC algorithm implemented in the treatment planning system.

Bibliography

- [1] J. M. Slater, "From X-Rays to Ion Beams: A Short History of Radiation Therapy," in *Ion Beam Therapy*, U. Linz, Ed. Springer Berlin Heidelberg, pp. 3–16, 2012.
- [2] P. P. Connell and S. Hellman, "Advances in radiotherapy and implications for the next century: a historical perspective," *Cancer Res.*, vol. 69, no. 2, pp. 383–392, 2009.
- [3] R. Wilhelm, "Über eine neue Art von Strahlen," in *Sitzungsberichte der physikalisch-medizinischen Gesellschaft zu Würzburg*, vol. 137, pp. 132–141, 1895.
- [4] L. Freund, "Ein mit Röntgenstrahlen behandelter Fall von Naevus pigmentosus piliferus," *Wien. Med. Wochenschr.*, vol. 47, pp. 856–860, 1897.
- [5] H. Becquerel, "Sur les radiations émises par phosphorescence," *Comptes Rendus L'Académie Sci.*, vol. 122, pp. 420–421, 1896.
- [6] P. Curie and M. Curie, "Sur une substance nouvelle radioactive, contenue dans la pechblende," *Comptes Rendus Académie Sci.*, vol. 127, p. 175, 1898.
- [7] H. Becquerel and C. Pierre, "Action physiologique des rayons du radium," *Comptes Rendus L'Académie Sci.*, vol. 132, pp. 1289–1291, 1901.
- [8] Nobelprize.org, http://www.nobelprize.org/nobel_prizes/physics/laureates/1903/, retrieved on 27-January-2015.
- [9] L. Freund, *Elements of general radio-therapy for practitioners*. Rebman, 1904.
- [10] C. Regaud and R. Ferroux, "Discordance des effets des rayons X, d'une part dans la peau, d'autre part dans le testicule, par fractionnement de la dose: diminution de l'efficacité dans la peau, maintien de l'efficacité dans le testicule," *C. R. Biol.*, 1927.
- [11] H. Coutard, "Principles of x-ray therapy of malignant disease," *The Lancet*, vol. 2, pp. 1–12, 1934.
- [12] W. D. Coolidge, "A Powerful Röntgen Ray Tube with a Pure Electron Discharge," *Phys. Rev.*, vol. 2, no. 6, pp. 409–430, 1913.
- [13] W. D. Coolidge, "Cathode-ray and Roentgen-ray work in progress," *Am. J. Roentgenol.*, vol. 19, pp. 313–321, 1928.
- [14] R. Wideröe, "Über ein neues Prinzip zur Herstellung hoher Spannungen," *Arch. Für Elektrotechnik*, vol. 21, no. 4, pp. 387–406, 1928.
- [15] E. O. Lawrence and M. S. Livingston, "The Production of High Speed Light Ions Without the Use of High Voltages," *Phys. Rev.*, vol. 40, no. 1, pp. 19–35, 1932.
- [16] D. W. Kerst, "The Acceleration of Electrons by Magnetic Induction," *Phys. Rev.*, vol. 60, no. 1, pp. 47–53, 1941.
- [17] C. J. Karzmark and N. C. Pering, "Electron linear accelerators for radiation therapy: history, principles and contemporary developments," *Phys. Med. Biol.*, vol. 18, pp. 321–354, 1973.
- [18] R. R. Wilson, "Radiological use of fast protons," *Radiology*, vol. 47, no. 5, pp. 487–491, 1946.

- [19] M. L. Boone, J. H. Lawrence, W. G. Connor, R. Morgado, J. A. Hicks, and R. C. Brown, "Introduction to the use of protons and heavy ions in radiation therapy: historical perspective," *Int. J. Radiat. Oncol. Biol. Phys.*, vol. 3, pp. 65–69, 1977.
- [20] J. H. Lawrence, C. A. Tobias, J. L. Born, R. K. McCOMBS, J. E. Roberts, H. O. Anger, B. V. Low-Beer, and C. B. Huggins, "Pituitary irradiation with high-energy proton beams: a preliminary report," *Cancer Res.*, vol. 18, no. 2, pp. 121–134, 1958.
- [21] B. Larsson, L. Leksell, B. Rexed, P. Sourander, W. Mair, and B. Andersson, "The high-energy proton beam as a neurosurgical tool," *Nature*, vol. 182, no. 4644, pp. 1222–1223, 1958.
- [22] J. M. Slater, D. W. Miller, and J. O. Archambeau, "Development of a hospital-based proton beam treatment center," *Int. J. Radiat. Oncol. Biol. Phys.*, vol. 14, no. 4, pp. 761–775, 1988.
- [23] J. R. Castro, D. E. Linstadt, J. P. Bahary, P. L. Petti, I. Daftari, J. M. Collier, P. H. Gutin, G. Gauger, and T. L. Phillips, "Experience in charged particle irradiation of tumors of the skull base: 1977-1992," *Int. J. Radiat. Oncol. Biol. Phys.*, vol. 29, no. 4, pp. 647–655, 1994.
- [24] H. Tsujii, J. Mizoe, T. Kamada, M. Baba, S. Kato, H. Kato, H. Tsuji, S. Yamada, S. Yasuda, T. Ohno, T. Yanagi, A. Hasegawa, T. Sugawara, H. Ezawa, S. Kandatsu, K. Yoshikawa, R. Kishimoto, and T. Miyamoto, "Overview of clinical experiences on carbon ion radiotherapy at NIRS," *Radiother. Oncol.*, vol. 73, Supplement 2, pp. S41–S49, 2004.
- [25] Particle Therapy Co-Operative Group, <http://www.ptcoq.ch/index.php/facilities-in-operation>. retrieved on 27-January-2015.
- [26] K. C. Tsien, "The application of automatic computing machines to radiation treatment planning. 1954," *Br. J. Radiol.*, vol. 68, no. 814, pp. H157–164, 1995.
- [27] P. N. T. Wells, "Sir Godfrey Newbold Hounsfield KT CBE. 28 August 1919 – 12 August 2004 Elected F.R.S. 1975," *Biogr. Mem. Fellows R. Soc.*, vol. 51, pp. 221–235, 2005.
- [28] I. Young, "Hounsfield, Sir Godfrey Newbold," *Oxf. Dict. Natl. Biogr. Online Ed*, 2009.
- [29] M. B. Levene, P. K. Kijewski, L. M. Chin, B. E. Bjärngard, and S. Hellman, "Computer-controlled radiation therapy," *Radiology*, vol. 129, no. 3, pp. 769–775, Dec. 1978.
- [30] J. V. Dyk, "The Modern Technology of Radiation Oncology: A Compendium for Medical Physicists and Radiation Oncologists," Medical Physics Pub., 1999.
- [31] E. Pedroni, "Latest Developments in Proton Therapy," in *Proceedings of EPAC*, pp. 240–244, 2000.
- [32] F. M. Khan, "The Physics of Radiation Therapy," Lippincott Williams & Wilkins, pp. 467–506, 2010.
- [33] P. Mayles, A. Nahum, and J. Rosenwald, "Handbook of Radiotherapy Physics: Theory and Practice," 2007.
- [34] H. Krieger, *Grundlagen der Strahlungsphysik und des Strahlenschutzes*. Springer Spektrum, 2012.
- [35] The International Commission on Radiation Units and Measurements, "Fundamental Quantities and Units for Ionizing Radiation," 1998.

- [36] A. Einstein, "Über einen die Erzeugung und Verwandlung des Lichtes betreffenden heuristischen Gesichtspunkt," in *Annalen der Physik*, vol. 17, pp. 132–148, 1905.
- [37] H. Krieger and W. Petzold, "Strahlenphysik, Dosimetrie und Strahlenschutz I: Grundlagen," Teubner Verlag, 1992.
- [38] J. T. Bushberg, "The AAPM/RSNA physics tutorial for residents. X-ray interactions," *Radiogr. Rev. Publ. Radiol. Soc. N. Am. Inc.*, vol. 18, no. 2, pp. 457–468, 1998.
- [39] The International Commission on Radiation Units and Measurements, "Linear Energy Transfer," *ICRU Report 16*, 1970.
- [40] R. E. Zirkle, D. F. Marchbank, and K. D. Kuck, "Exponential and sigmoid survival curves resulting from alpha and x irradiation of *Aspergillus* spores," *J. Cell. Physiol. Suppl.*, vol. 39, no. Suppl. 1, pp. 78–85, 1952.
- [41] G. Failla and P. S. Henshaw, "The Relative Biological Effectiveness of X-rays and Gamma Rays," *Radiology*, vol. 17, no. 1, pp. 1–43, 1931.
- [42] H. Paganetti, A. Niemierko, M. Ancukiewicz, L. E. Gerweck, M. Goitein, J. S. Loeffler, and H. D. Suit, "Relative biological effectiveness (RBE) values for proton beam therapy," *Int. J. Radiat. Oncol.*, vol. 53, no. 2, pp. 407–421, 2002.
- [43] H. Paganetti, "Interpretation of proton relative biological effectiveness using lesion induction, lesion repair, and cellular dose distribution," *Med. Phys.*, vol. 32, no. 8, pp. 2548–2556, 2005.
- [44] The International Atomic Energy Agency Vienna, "Relative Biological Effectiveness in Ion Beam Therapy," *Technical Report Series No. 461*, 2008.
- [45] D. T. Goodhead, "Radiation effects in living cells," *Can. J. Phys.*, vol. 68, no. 9, pp. 872–886, 1990.
- [46] U. Linz, *Ion Beam Therapy: Fundamentals, Technology, Clinical Applications*. Springer, 2012.
- [47] D. Schulz-Ertner, O. Jäkel, and W. Schlegel, "Radiation therapy with charged particles," *Semin. Radiat. Oncol.*, vol. 16, no. 4, pp. 249–259, 2006.
- [48] T. DeLaney and H. Kooy, "Proton and Charged Particle Radiotherapy," Lippincott Williams & Wilkins, 2008.
- [49] H. Paganetti, "Proton Therapy," in *New Technologies in Radiation Oncology*, Springer Berlin Heidelberg, pp. 345–363, 2006.
- [50] E. J. Hall, "Intensity-modulated radiation therapy, protons, and the risk of second cancers," *Int. J. Radiat. Oncol.*, vol. 65, no. 1, pp. 1–7, 2006.
- [51] A.-L. Grosu and M. Molls, "Definition of Target Volume and Organs at Risk. Biological Target Volume," in *New Technologies in Radiation Oncology*, Springer Berlin Heidelberg, pp. 167–177, 2006.
- [52] The International Commission on Radiation Units and Measurements, "Prescribing, Recording, and Reporting Photon Beam Therapy," *Journal of the ICRU Volume 4 No 1*, 1993.

- [53] The International Commission on Radiation Units and Measurements, "Prescribing, Recording and Reporting Intensity-Modulated Photon-Beam Therapy (IMRT)," *Journal of the ICRU Volume 10 No 1*, 2010.
- [54] T. Bortfeld, "Optimization of Treatment Plans, Inverse Planning," in *New Technologies in Radiation Oncology*, Springer Berlin Heidelberg, pp. 207–220, 2006.
- [55] S. Webb, "Conformal and Intensity-Modulated Radiotherapy," *Handb. Radiother. Phys.*, pp. 943–974, 2007.
- [56] C. Ma, H. Mayles, and P. Mayles, "Intensity-Modulated Radiotherapy: Practical Aspects," *Handb. Radiother. Phys.*, pp. 975–986, 2007.
- [57] U. Oelfke, "Dose Calculation Algorithms," in *New Technologies in Radiation Oncology*, Springer Berlin Heidelberg, pp. 187–196, 2006.
- [58] M. Soukup, M. Fippel, and M. Alber, "A pencil beam algorithm for intensity modulated proton therapy derived from Monte Carlo simulations," *Phys. Med. Biol.*, vol. 50, no. 21, pp. 5089–5104, 2005.
- [59] L. Hong, M. Goitein, M. Bucciolini, R. Comiskey, B. Gottschalk, S. Rosenthal, C. Serago, and M. Urie, "A pencil beam algorithm for proton dose calculations," *Phys. Med. Biol.*, vol. 41, no. 8, p. 1305, 1996.
- [60] E. Pedroni, S. Scheib, T. Böhringer, A. Coray, M. Grossmann, S. Lin, and A. Lomax, "Experimental characterization and physical modelling of the dose distribution of scanned proton pencil beams," *Phys. Med. Biol.*, vol. 50, no. 3, p. 541, 2005.
- [61] M. Hillbrand and D. Georg, "Assessing a set of optimal user interface parameters for intensity-modulated proton therapy planning," *J. Appl. Clin. Med. Phys. Am. Coll. Med. Phys.*, vol. 11, no. 4, p. 3219, 2010.
- [62] T. Knöös, A. Ahnesjö, P. Nilsson, and L. Weber, "Limitations of a pencil beam approach to photon dose calculations in lung tissue," *Phys. Med. Biol.*, vol. 40, no. 9, pp. 1411–1420, 1995.
- [63] B. Schaffner, E. Pedroni, and A. Lomax, "Dose calculation models for proton treatment planning using a dynamic beam delivery system: an attempt to include density heterogeneity effects in the analytical dose calculation," *Phys. Med. Biol.*, vol. 44, no. 1, pp. 27–41, 1999.
- [64] M. Fippel, "Monte Carlo Dose Calculation for Treatment Planning," in *New Technologies in Radiation Oncology*, Springer Berlin Heidelberg, pp. 197–206, 2006.
- [65] M. Fippel and M. Soukup, "A Monte Carlo dose calculation algorithm for proton therapy," *Med. Phys.*, vol. 31, no. 8, pp. 2263–2273, 2004.
- [66] A. Tourovsky, A. J. Lomax, U. Schneider, and E. Pedroni, "Monte Carlo dose calculations for spot scanned proton therapy," *Phys. Med. Biol.*, vol. 50, no. 5, pp. 971–981, 2005.
- [67] J. S. Li, T. Pawlicki, J. Deng, S. B. Jiang, E. Mok, and C. M. Ma, "Validation of a Monte Carlo dose calculation tool for radiotherapy treatment planning," *Phys. Med. Biol.*, vol. 45, no. 10, pp. 2969–2985, 2000.
- [68] J. E. Gentle, "Random Number Generation and Monte Carlo Methods," Springer Berlin Heidelberg, 2003.

- [69] I. Kawrakow, "The effect of Monte Carlo statistical uncertainties on the evaluation of dose distributions in radiation treatment planning," *Phys. Med. Biol.*, vol. 49, no. 8, p. 1549, 2004.
- [70] P. M. Pardalos and H. E. Romeijn, *Handbook of Optimization in Medicine*. Springer Science & Business Media, 2009.
- [71] A. Brahme, "Optimized radiation therapy based on radiobiological objectives," *Semin. Radiat. Oncol.*, vol. 9, no. 1, pp. 35–47, 1999.
- [72] T. Bortfeld, "Optimized planning using physical objectives and constraints," *Semin. Radiat. Oncol.*, vol. 9, no. 1, pp. 20–34, 1999.
- [73] U. Oelfke, S. Nill, and J. J. Wilkens, "Physical Optimization," in *Image Guided IMRT*, Springer Berlin Heidelberg, pp. 31–45, 2006.
- [74] T. Kataria, K. Sharma, V. Subramani, K. P. Karrthick, and S. S. Bisht, "Homogeneity index: An objective tool for assessment of conformal radiation treatments," *J. Med. Phys. Assoc. Med. Phys. India*, vol. 37, no. 4, pp. 207–213, 2012.
- [75] L. Feuvret, G. Noël, J.-J. Mazon, and P. Bey, "Conformity index: a review," *Int. J. Radiat. Oncol. Biol. Phys.*, vol. 64, no. 2, pp. 333–342, 2006.
- [76] I. Paddick, "A simple scoring ratio to index the conformity of radiosurgical treatment plans," *J. Neurosurg.*, vol. 93 Suppl 3, pp. 219–222, 2000.
- [77] D. A. Low, W. B. Harms, S. Mutic, and J. A. Purdy, "A technique for the quantitative evaluation of dose distributions," *Med. Phys.*, vol. 25, no. 5, pp. 656–661, 1998.
- [78] M. Stock, B. Kroupa, and D. Georg, "Interpretation and evaluation of the gamma index and the gamma index angle for the verification of IMRT hybrid plans," *Phys. Med. Biol.*, vol. 50, no. 3, pp. 399–411, 2005.
- [79] A. Bakai, M. Alber, and F. Nüsslin, "A revision of the gamma-evaluation concept for the comparison of dose distributions," *Phys. Med. Biol.*, vol. 48, no. 21, pp. 3543–3553, 2003.
- [80] D. A. Low, "Gamma Dose Distribution Evaluation Tool," *J. Phys. Conf. Ser.*, vol. 250, no. 1, p. 012071, 2010.
- [81] Computational Environment for Radiotherapy Research, "CERR WIKI," 2012.
- [82] M. Wendling, L. J. Zipp, L. N. McDermott, E. J. Smit, J.-J. Sonke, B. J. Mijnheer, and M. van Herk, "A fast algorithm for gamma evaluation in 3D," *Med. Phys.*, vol. 34, no. 5, pp. 1647–1654, 2007.
- [83] G. O. Sawakuchi, U. Titt, D. Mirkovic, and R. Mohan, "Density heterogeneities and the influence of multiple Coulomb and nuclear scatterings on the Bragg peak distal edge of proton therapy beams," *Phys. Med. Biol.*, vol. 53, no. 17, pp. 4605–4619, 2008.
- [84] CMS. Inc., *XiO Online Help Version 4.62*. 2010.

List of Figures

2.1	Principle of coherent scattering of a photon	6
2.2	Principle of the Compton effect	7
2.3	Angular distributions of scattered Compton photons	8
2.4	Principle of the photoelectric effect	9
2.5	Energy dependence of the mass photon absorption coefficient for lead	10
2.6	Principle of pair production.	10
2.7	Different photon interactions as a function of atomic number and energy.	12
2.8	Coherent scattering, photoelectric, Compton, pair production and total mass attenuation coefficients for soft tissue ($Z=7$) as a function of energy.	12
2.9	Amount of particles and energy losses as a function of the penetration depth	14
2.10	Determining the RBE on the basis of cell survival and dose-response curves	15
2.11	i) Relative dose as a function of the penetration depth of photons, protons and carbon ions. ii) Spread out Bragg peak.	16
2.12	Dose-response curves	18
2.13	Principle of passive scattering proton beam delivery	20
2.14	Principle of active scanning proton beam delivery.	21
2.15	Various treatment volumes.	23
2.16	Difference between conformal radiotherapy IMRT	27
2.17	Influence of the number of sub-spots on the dose distribution at the surface of a water phantom if a blocking device is present	31
2.18	Optimization loop for iterative IMRT optimization.	34
2.19	Example of a i) cumulative DVH and a ii) differential DVH.	36
3.1	Phantom used by Soukup et al.	39
3.2	Phantom setup for the evaluation of the MC parameters.	40
3.3	Phantom setup for the evaluation of the MC parameters	41
3.4	Phantom setup for the evaluation of the user interface parameters	42
3.5	Text file <i>pb_calc_param</i> to change the MC parameters	45
3.6	Beam setup used for the assessment of the MC parameters	46
3.7	Beam setup used for the assessment of the user interface parameters	47
4.1	Dose homogeneity of treatment plans using the Chess Target	51

4.2	Isodose distributions of the Chess Target using a gantry angle of 0°	52
4.3	Dose-difference maps (gantry angle 0°)	53
4.4	Dose-difference maps (gantry angle 15°)	53
4.5	Chess Target with 30 mm margin for the γ -index analysis.	55
4.6	Dose homogeneity of treatment plans using Target 1, 2 and 3	59
4.7	Dose-difference maps of the recalculated MC (unc=0.05, err=0.6) - optimized PB treatment plan for i) Target 1, ii) Target 2 and iii) Target 3.	60
4.8	Dose-difference maps of the recalculated MC (unc=0.03, err=0.1) - optimized PB treatment plan for i) Target, 1 ii) Target 2 and iii) Target 3.	60
4.9	Dose-difference maps of the optimized MC (unc=0.05, err=0.6) - optimized PB treatment plan for i) Target 1, ii) Target 2 and iii) Target 3.	61
4.10	Depth-dose profiles of the small target using different PWM values	64
4.11	Dose distributions of the small target	65
4.12	Dose profiles of the small target calculated with different PWM values	65
4.13	Dose homogeneity of all three targets with respect to changes of the PWM	66
4.14	Dose conformity of all three targets with respect to changes of the PWM.	67
4.15	Dose homogeneity of all three targets with respect to changes of the spot spacing	68
4.16	Isodose distribution of the prostate patient (one beam) calculated with the MC algorithm (unc=0.05, err=0.6) with the PTV and OARs.	69
4.17	Dose-difference map of the prostate patient (one beam)	70
4.18	3D margin of 50 mm around the PTV.	71
4.19	Isodose distribution of the prostate patient (two beams)	71
4.20	Dose homogeneity of treatment plans of the prostate patient with respect to changes of MC parameters.	72
4.21	Cumulative DVH of the prostate patient (two beams) calculated with the MC (unc=0.05, err=0.6) and PB algorithm.	73
4.22	Dose-difference maps of the prostate patient (two beams)	74
4.23	Dose-difference maps of the prostate patient (two beams)	75
4.24	Isodose distribution of the paranasal sinus patient with the PTV and OARs.	78
4.25	Cumulative DVHs of the PS patient	79
4.26	Dose difference maps of the PS patient	80

List of Tables

2.1	Dependencies of the attenuation coefficient from the Photon energy, atomic number and mass number of the absorber.	11
2.2	Constraints for γ -index-volume specifications.	38
3.1	Dimensions and radiodensities of the structures of the Testphantom	39
3.2	Dimensions and radiodensities of the structures of the Chessphantom	41
3.3	Dimensions and radiodensities of the structures of the Waterphantom.	42
4.1	Dose calculation times, HI and CI for different unc and err values and maximum numbers of particles.	48
4.2	Dose calculation times and dosimetric evaluation parameters when using chess target with a gantry angle of 0° and 15°	50
4.3	Failure rate, γ_{mean} and $\gamma_{1\%}$ values of the Chess Target using a gantry angle of 0° . . .	55
4.4	Failure rate, γ_{mean} and $\gamma_{1\%}$ values of the Chess Target using a gantry angle of 15° . . .	56
4.5	Dose calculation times and dosimetric evaluation parameters when using Target 1. . .	57
4.6	Dose calculation times and dosimetric evaluation parameters when using Target 2. . .	57
4.7	Dose calculation times and dosimetric evaluation parameters when using Target 3. . .	58
4.8	Failure rate, γ_{mean} and $\gamma_{1\%}$ values when using Target 1	62
4.9	Failure rate, γ_{mean} and $\gamma_{1\%}$ values when using Target 2	62
4.10	Failure rate, γ_{mean} and $\gamma_{1\%}$ values when using Target 3	63
4.11	Dose calculation times and dosimetric evaluation parameters for different PWM values of the small, mid-sized and large target.	66
4.12	Dose calculation times and dosimetric evaluation parameters for different spot spacing values of the small, mid-sized and large target.	68
4.13	Dose calculation times and dosimetric evaluation parameters of the prostate patient treatment plans (one beam)	70
4.14	Failure rate, γ_{mean} and $\gamma_{1\%}$ values of the prostate patient (one beam).	70
4.15	Dose calculation times and dosimetric evaluation parameters of the prostate patient treatment plans (two beams)	72
4.16	Failure rate, γ_{mean} and $\gamma_{1\%}$ values of the prostate patient (two beams)	75
4.17	Failure rate, γ_{mean} and $\gamma_{1\%}$ values for the reduced area (two beams)	76
4.18	Dose calculation times of the prostate patient for different PTV sizes	77
4.19	Dose calculation times and dosimetric evaluation parameters of the PS patient	78
4.20	Failure rate, γ_{mean} and $\gamma_{1\%}$ values of the PS patient	81

List of Abbreviations

<i>PB</i>	Pencil Beam
<i>MC</i>	Monte Carlo
<i>LET</i>	Linear Energy Transfer
<i>RBE</i>	Relative Biological Effectiveness
<i>GTV</i>	Gross Tumor Volume
<i>CTV</i>	Clinical Target Volume
<i>PTV</i>	Planning Target Volume
<i>TV</i>	Treated Volume
<i>OAR</i>	Organ At Risk
<i>CRT</i>	Conformal Radiotherapy
<i>MLC</i>	Multileaf Collimator
<i>IMRT</i>	Intensity-Modulated Radiation Therapy
<i>IMPT</i>	Intensity-Modulated Particle Therapy
<i>SFUD</i>	Single-Field Uniform Dose
<i>DVH</i>	Dose-Volume Histogram
$D_{2\%}$	Dose which 2% of the volume receives
$D_{50\%}$	Dose which 50% of the volume receives
$D_{98\%}$	Dose which 98% of the volume receives
$V_{95\%}$	Volume which receives 95% of the prescribed dose
<i>HI</i>	Homogeneity index
<i>CI</i>	Conformity index
<i>DTA</i>	Distance-To-Agreement
γ_{mean}	Average γ -value
$\gamma_{1\%}$	1% of points have an equal or higher γ -value
<i>unc</i>	MCuncertainty, Mean Relative Statistical Uncertainty
<i>err</i>	MCerrordosethreshold, Mean Relative Statistical Uncertainty Threshold
<i>prec</i>	Precision
<i>PWM</i>	Peak Width Multiplier
<i>D.C.T</i>	Dose Calculation Time
<i>dose</i>	The term refers to the PB treatment plan recalculated using the MC algorithm
<i>opt</i>	The term refers to the PB treatment plan recalculated and then optimized using the MC algorithm
<i>S.S</i>	Spot Spacing
<i>PS</i>	Paranasal Sinus